Enhancing the performance of Si photonics: structure-property relations and engineered dispersion relations

Hamdam Nikkhah

Thesis submitted in partial fulfillment of the requirements for the

Doctorate in Philosophy degree in Electrical and Computer Engineering

Ottawa-Carleton Institute for Electrical and Computer Engineering

School of Electrical Engineering and Computer Science

University of Ottawa

Abstract

The widespread adoption of photonic circuits requires the economics of volume manufacturing offered by integration technology. A Complementary Metal-Oxide Semiconductor compatible silicon material platform is particularly attractive because it leverages the huge investment that has been made in silicon electronics and its high index contrast enables tight confinement of light which decreases component footprint and energy consumption. Nevertheless, there remain challenges to the development of photonic integrated circuits. Although the density of integration is advancing steady and the integration of the principal components – waveguides, optical sources and amplifiers, modulators, and photodetectors – have all been demonstrated, the integration density is low and the device library far from complete. The integration density is low primarily because of the difficulty of confining light in structures small compared to the wavelength which measured in micrometers. The device library is incomplete because of the immaturity of hybridisation on silicon of other materials required by active devices such as III-V semiconductor alloys and ferroelectric oxides and the difficulty of controlling the coupling of light between disparate material platforms. Metamaterials are nanocomposite materials which have optical properties not readily found in Nature that are defined as much by their geometry as their constituent materials. This offers the prospect of the engineering of materials to achieve integrated components with enhanced functionality. Metamaterials are a class of photonic crystals includes subwavelength grating waveguides, which have already provided breakthroughs in component performance yet require a simpler fabrication process compatible with current minimum feature size limitations.

The research reported in this PhD thesis advances our understanding of the structure-property relations of key planar light circuit components and the metamaterial engineering of these properties. The analysis and simulation of components featuring structures that are only just subwavelength is complicated and consumes large computer resources especially when a three dimensional analysis of components structured over a scale larger than the wavelength is desired. This obstructs the iterative design-simulate cycle. An abstraction is required that summarises the properties of the metamaterial pertinent to the larger scale while neglecting the microscopic detail. That abstraction is known as homogenisation. It is possible to extend homogenisation from the long-wavelength limit up to the Bragg resonance (band edge). It is found that a metamaterial waveguide is accurately modeled as a continuous medium waveguide provided proper account is taken of the emergent properties of the homogenised metamaterial. A homogenised subwavelength grating waveguide structure behaves as a strongly anisotropic and spatially dispersive material with a c-axis normal to the layers of a one dimensional multi-layer structure (Kronig-Penney) or along the axis of uniformity for a two dimensional photonic crystal in three dimensional structure. Issues with boundary effects in the near Bragg resonance subwavelength are avoided either by ensuring the averaging is over an extensive path parallel to boundary or the sharp boundary is removed by graded structures. A procedure is described that enables the local homogenised index of a graded structure to be determined. These finding are confirmed by simulations and experiments on test circuits composed of Mach-Zehnder interferometers and individual components composed of regular nanostructured waveguide segments with different lengths and widths; and graded adiabatic waveguide tapers. The test chip included Lüneburg micro-lenses, which have application to Fourier optics on a chip. The measured loss of each lens is 0.72 dB.

Photonic integrated circuits featuring a network of waveguides, modulators and couplers are important to applications in RF photonics, optical communications and quantum optics. Modal phase error is one of the significant limitations to the scaling of multimode interference coupler port dimension. Multimode interference couplers rely on the Talbot effect and offer the best in-class performance. Anisotropy helps reduce the Talbot length but temporal and spatial dispersion is necessary to control the modal phase error and wavelength dependence of the Talbot length. The Talbot effect in a Kronig-Penny metamaterial is analysed. It is shown that the metamaterial may be engineered to provide a close approximation to the parabolic dispersion relation required by the Talbot effect for perfect imaging. These findings are then applied to the multimode region and access waveguide tapers of a multi-slotted waveguide multimode interference coupler with slots either in the transverse direction or longitudinal direction. A novel polarisation beam splitter exploiting the anisotropy provided by a longitudinally slotted structure is demonstrated by simulation.

The thesis describes the design, verification by simulation and layout of a photonic integrated circuit containing metamaterial waveguide test structures. The test and measurement of the fabricated chip and the analysis of the data is described in detail. The experimental results show good agreement with the theory, with the expected errors due to fabrication process limitations. From the Scanning Electron Microscope images and the measurements, it is clear that at the boundary of the minimum feature size limit, the error increases but still the devices can function.

Acknowledgments

I would like to express my sincere appreciation to my supervisor, Dr. Trevor Hall, who provided me the opportunity to work in a field to which I aspired and for his continuous support and guidance; without which this thesis would not have been possible. His encouragement and enthusiasm have been a great motivation to continue this interesting work. I am grateful to Dr. Sawsan Abdul-Majid, Dr. Ramon Maldonado-Basilio, Peng Liu in Photonic Technology Laboratory (PTLab), Dr. Pierre Berini, Anthony Olivieri Centre for Research in Photonics at the University of Ottawa (CRPuO), and Tom Davis (Photon Design) for their kind and immediate assistance with simulation, experimental advice and SEM facilities over the past four years. I also would like to express my gratitude to Dr. Jessica Zhang and CMC Microsystems for sharing their experience of silicon photonics design and providing the funds for the fabrication during the project. A special thank you to Dr. Karin Hinzer for her always kind and friendly advice during my study at the University of Ottawa. I would like to thank my friends and colleagues in PTLab and CRPuO for their contribution to a friendly working environment. I am grateful to the members of my thesis advisory committee, Dr. Serge Bidnyk, Dr. Tet Yeap for their interest in my work, and Dr. Pavel Cheben for his sound and practical advice on subwavelength gratings.

Finally I give a special and deeply felt thank you to my family, my mother and my brother that provided the greatest and warmest encouragement and throughout my life to pursue my goals. I am indebted to them for their continuous support, closely or remotely, during my study. Deepest thanks to my father who helped me find my path confidently into science, greatly encouraged my academic aims, and his memory made me confident to follow what I adore.

Table of Contents

List of Tables

List of Figures

List of Acronyms

CGH	Computer Generated Hologram
CMOS	Complementary Metal-Oxide Semiconductor
MMI	Multimode Interference Coupler
MZI	Mach Zehnder Interferometer
OPL	Optical Path Length
OPD	Optical Path Length Difference
PIC	Photonic Integrated Circuit
PLC	Planar Light Circuit
Si	Silicon
SOI	Silicon On Insulator
SWG	Sub-Wavelength Grating
TE	Transverse Electric
TM	Transverse Magnetic
1D	One Dimensional
2D	Two Dimensional
3D	Three Dimensional

Chapter 1. Introduction

Optics and photonics, the science and technology of the control of light, have been developed rapidly by advances in micro- and nano- scale structures and devices during the last decade. This development includes applications to energy, communications, life-sciences, displays, imaging and advanced manufacturing. The optical communication sector have embraced silicon as the material platform of choice to decrease component footprint, energy consumption, and, most important, to reduce cost by leveraging the vast investment of the electronics industry in silicon microfabrication and the consequent maturity of the fabrication processes. The major challenge confronting a designer of a photonic integrated circuit is the low density of integration currently possible and a device library that is far from complete. Fundamentally, these challenges stem from the difficulty of confining light below the scale of its wavelength, which is measured in micrometres. In contrast, electrons may be relatively easily confined in devices measured in nanometers. Two recent developments in the field offer hope that the precise control of light lies with our grasp: transformation optics, which enables the material parameters needed to support a target desired optical field to be found, and effective media theory (also known as homogenisation), which enables the constituent elements of a composite material to be specified such that its continuous medium equivalent possesses any desired optical property.

This thesis presents the findings of research concerning the structure-property relations of key planar light circuit (PLC) components and the metamaterial engineering of these properties. This has important application to the next generation of coherent photonic systems in which the control of the complex amplitude of the field rather than the intensity (magnitude squared) is critical. Outcomes include new design procedures of practical utility founded on the fundamental physics of metamaterials, sub-wavelength grating waveguides and the identification of opportunities for break-through integrated photonic devices that metamaterial engineering has to offer. This chapter provides the motivation and background to set this research in context, outlines the challenges to be addressed and explains how the thesis is structured to meet its objectives.

1.1 Background & Motivation

1.1.1. Silicon-based Integrated Photonics

The continuous demand for small form factor requires compact components and circuits which has raised the importance of improved photonic integration. The silicon-based photonic integration platform has become prominent in the field because it provides the benefits of high-density photonic integration and complementary metal-oxide-semiconductor (CMOS) compatibility. Silicon-on-insulator (SOI) has become the most popular silicon photonic integration material platform by offering compact device footprints due to the tight confinement of light provided by high refractive index contrast waveguides. Enhancing the

performance of optical structures and, consequently, the optical devices and circuits that make use of these structures, has been achieved either by improving the structure itself, or by using more capable materials. Composite materials have shown great utility in the improvement of photonics components and devices.

Large components may result in circuit footprints that exceed the dimensions of a chip resulting in the reduced robustness and increased expense, loss, and power consumption, of multi-chip solutions. For example, regardless of the implementation technology, switch elements are limited to low port dimensions. To achieve large port dimension, it is necessary to use an optical interconnection network to combine a large number of small switch elements into a switch-fabric. The multiple stages and large number of waveguide crossovers of the optical interconnection network complicate fabrication and contribute to excessive insertion loss and crosstalk. A capability to pattern the silicon structures at a micro- or nano-scale would offer the freedom to engineer the properties of integrated optical components to avoid the aforementioned issues. Moreover, composite materials structured on a subwavelength scale can create materials with effective continuous media properties that cannot be readily found in nature. The nanocomposite material is then known as a 'subwavelength grating' (SWG)' structure [1]. A 'metamaterial' is another alternative term used to describe nanostructured composite materials that have effective electro-magnetic material properties that arise as much from the geometry of the structure as the constituent materials. This creates an opportunity for new optical devices founded on these materials.

Fortunately, progress in nanofabrication has given more freedom to use the SWG structures to engineer and tailor the refractive index and dispersion properties of integrated components [2]. For instance the interconnections in switch structures using planar Lüneburg lenses based on graded SWGs, which offer, in addition to insertion loss and cross talk reduction, the simplicity of a binary etch process compared to the complex fabrication processing otherwise required to create continuously profiled or graded index lenses that needs a complicated multi-step etching process [3]. Also waveguide crossings based on SWG in silicon waveguides offer insertion loss as low as -0.023 dB/crossing [4], while crossovers of photonics wires on SOI showed an insertion loss of between -0.4 dB and -0.1 dB per crossing [5, 6]. The cross-talk in both cases was almost the same, <-40dB, but the SWG structure has the advantage of a less complex fabrication process [7].

SWG structures also can improve the performance of the key components and reduce their footprints. For example, conventional multimode interference couplers (MMIs) are compact, operate over a broad bandwidth of 100 nm and are robust to fabrication errors; hence they are widely used in PICs. However, as the number of ports is increased the performance of a MMI significantly reduces as the modal phase error scales with the number of ports. This can be ameliorated by the use of a low index contrast platform [8] but this conflicts with the requirement for high quality fractional self-imaging that the modal expansion is close to a Fourier series.

An alternative approach is to apply a perturbation to the lateral refractive index profile in the multimode section to reduce the modal phase errors [9]. Shallow etching of the multimode region can also reduce the effective index contrast [10], but these solutions have the demerit of requiring a multiple etch steps in the fabrication process. MMIs formed using a SWG structure offer a solution requiring only a single etch step. In this way, the lateral refractive index contrast may be reduced by using SWG in the lateral cladding regions of the multimode section while the high index contrast on the access waveguides remains to be able to place them closely to reduce the size of MMIs when the number of ports increases [11]. Moreover, the modal birefringence of the waveguide can be controlled by depositing low and high index layers with the subwavelength pitch on the top of the waveguide [12]. MMIs that make use of the anisotropy of SWG structure to achieve ultra-compact footprints have been reported recently [13] and the SWG MMI reported by Maese-Novo, Halir et al [14] operates over an ultra-broad bandwidth of 450 nm with the insertion loss of 1 dB and with a port phase deviation of less than 3 degrees and occupying a footprint half that of a conventional MMI. In addition, using the SWG approach described, highly compact Mach-Zehnder interferometer (MZI) structures can be designed. MZIs are one of the most commonly used components in PICs which regularly occupy a large area on the chip, especially when a large optical path-length (OPL) imbalance is needed. Applying the SWG structure on MZI may offer freedom over a wide range in the choice of relative refractive index difference of the imbalanced arms of the MZI. The functionality of SWG structures may create components that manipulate the polarisation of light such as a polarization rotator or to compensate the polarisation dependence of a component to provide a polarization insensitive function [15, 16].

The physics community is interested in the exotic properties offered by metamaterials and most often experimental demonstrations are restricted to ‘metasurfaces’ – the modern term for ‘diffractive optical element’ – which are easier to fabricate using modern nanotechnology and can be probed optically using laboratory free-space optics. In contrast, the engineering community is interested in refractive index and dispersion engineered components for photonic integration. The focus is on SWGs, which are a sub-variety of metamaterials that have the attraction that the fabrication processes is amenable to the economics of mass manufacture by patterning in a single etch step of a binary nanocomposite material with a feature size that is not limited to expensive high resolution techniques such as electron-beam lithography. The ‘grating’ is typically one dimensional but the waveguide format adds considerable technical difficulty in terms of accurate modelling.

Whereas a device designer has access to a variety of software simulation tools to verify designs, these tools cannot substitute for the intuition of the designer informed by design rules founded on the underlying physics. An abstraction is required that summarises the properties of the material pertinent to good device design. The detail may then be accounted for in a further optimization step that refines the design; starting from a good simplified design. This abstraction is known as ‘homogenisation’ that may be done in different scales

and may simplify the analysis and designs of the periodic structures that will be discussed in more details in this thesis.

1.1.2. First Homogenisation

One hardly ever questions the treatment of materials as continuous media because it is an excellent approximation whenever a region small enough can be found that it can be considered infinitesimal on the scale of the problem but nevertheless may be large enough that it contains a huge number of particles. In the case of electromagnetic waves, the requirement is that the wavelength is long compared to the average distance between atoms. This requirement explains why materials may be treated as continuous media for visible light but the behaviour of hard X-rays and more so γ- rays is ballistic and can exhibit the atomistic nature of the matter.

Macroscopic theories regularly apply an average over elements of volume and ignore the microscopic fluctuations of the averaged quantities. Maxwell's equations strictly describe electromagnetic fields in the vacuum interacting with matter described by the charges ρ and currents j that include all contributions of both bound and free charges. The macroscopic equations of electromagnetics describe the average interaction and properties of the charged particles and the fields [17]. Hence, through a proper averaging process, the macroscopic field equations may be derived from the microscopic field equations. For example, a microscopic electric field, $\boldsymbol{e}$, and microscopic magnetic field, $\boldsymbol{h}$, may be rapidly fluctuating functions on the atomic scale but the macroscopic electric field, $\boldsymbol{E}$, and magnetic field, $\boldsymbol{H}$, defined as the average of the microscopic field:

$$\begin{aligned} \boldsymbol{E} &= \langle \boldsymbol{e} \rangle \\ \boldsymbol{H} &= \langle \boldsymbol{h} \rangle \end{aligned} \tag{1.1}$$

are smooth on the same scale, where $\langle \cdot \rangle$ denotes a volumetric average, often a unit cell of a crystalline material, or an ensemble average in the case of a random material.

This method was developed by H. A. Lorentz in 1906 and has been extended as a homogenisation method [17, 18]. Averaging the microscopic form of Maxwell's equations introduces the fundamental equations of the electrodynamics of continuous media [19]. If the permittivity and permeability of the vacuum are defined as ε_0 and μ_0 respectively, the microscopic constitutive equations can be written as:

$$\begin{aligned} \boldsymbol{d} &= \varepsilon_0 \boldsymbol{e} \\ \boldsymbol{b} &= \mu_0 \boldsymbol{h} \end{aligned} \tag{1.2}$$

where $\boldsymbol{d}$ is the microscopic electric induction, $\boldsymbol{e}$ is microscopic electric field, $\boldsymbol{b}$ is microscopic magnetic induction and $\boldsymbol{h}$ is the microscopic magnetic field. With respect to the microscopic fields, the constitutive equations of electric and magnetic induction $\boldsymbol{D}$ and $\boldsymbol{B}$ defined by macroscopic fields can be written as:

$$\boldsymbol{D} = \boldsymbol{\varepsilon E}$$
$$\boldsymbol{B} = \boldsymbol{\mu H} \tag{1.3}$$

where $\boldsymbol{\varepsilon}$ and $\boldsymbol{\mu}$ are the permittivity and permeability tensors of the continuous medium. In practice, this average can be considered when the wavelength of the electromagnetic field λ is much larger than the dimension l of the unit cells of the atoms.

Hence, if the field over real space unit cell is described by the exponential envelope $\exp(i\boldsymbol{k}.\boldsymbol{x})$ that varies little over one unit cell and an amplitude u with the lattice periodicity:

$$\varphi(\boldsymbol{x}) = \exp(i\boldsymbol{k}.\boldsymbol{x})\, u(\boldsymbol{x}) \tag{1.4}$$

The field averaging over the unit cell gives the macroscopic field as:

$$\langle\varphi\rangle(\boldsymbol{x}) = \exp(i\boldsymbol{k}.\boldsymbol{x})\, \langle u\rangle \tag{1.5}$$

This means that the media looks a homogeneous medium for a wavelength large enough in comparison with the unit cell. This method is called homogenisation which in this thesis is named as first homogenisation. In the next chapter second homogenisation with averaging over a larger scale of artificial materials in the long wavelength limit will be explained.

1.2 Aim & Objectives

The aim of this work is to explore the potential of metamaterials to improve the performance of photonic integrated components such as: increased definition precision of the amplitude and phase of light at the ports of a coupler, increased extinction ratio of interferometric devices based on such couplers, and reduced foot-print of PIC switch fabrics. The focus of this work is on the SOI platform as it offers the potential for extremely small device footprints and, due to its compatibility with CMOS, low cost manufacture. Specific objectives are:

1) To survey the theory of metamaterials and their homogenisation methods and assess their utility to address the challenges of the design and verification of 1D and 2D metamaterial structures.
2) To verify the role and importance of MMI in PIC and the methods to improve its functionality by making use the emergent anisotropic and spatially dispersive properties of SWG metamaterials to engineer the dispersion relation of the structures such as MMI.
3) To establish an effective means of adiabatic interfacing of SWG components to the other components within the circuit.
4) To design metamaterial test structures to test the predictions of the theory.
5) To fabricate and experimentally characterise a PIC containing test structures and circuits in order to validate the theory and design methodology

The expected outcomes include:

- a new design methodology for 1D and 2D SWG structures based on homogenisation;

- the establishment of effective strategies for the connection of metamaterial components to other components within a circuit;
- experimental design and implementation for test of the validity of the study.

1.3 Structure of the Thesis

To achieve these objectives the thesis has been structured into five chapters:

Chapter 1 describes the motivation and the background of the research. It addresses the development of PICs in the enhancement of the photonic systems, the importance of replacing bulky 3D optical components by components in planar format to be placed on the chips, the difficulties encountered and introduces the most relevant solutions offered in the literature today.

In Chapter 2, nanostructuring of photonic integrated circuit components and metamaterials are discussed to refine the optical properties of a device. Homogenisation concepts and methods for 1D and 2D lattice metamaterial structures are discussed and the dispersion confinement correction is introduced to account for the effect of the waveguide on the wave vector which removes an artifact when the metamaterial exhibits a bandgap at the operating wavelength for on-axis propagation.

In Chapter 3 the 1D metamaterial structures are discussed and their local anisotropic behaviour described. The modification of the dispersion relation is addressed using subwavelength engineering methods to reduce the modal phase error in structures such as MMI for perfect imaging. A polarisation beam splitter based on the Talbot effect in longitudinal metamaterial structure is proposed. The use of adiabatic structures to not only adapt waveguide dimensions but also adapt the homogenised index to avoid abrupt junctions is explained.

In Chapter 4 the grading of 2D metamaterials to implement gradient index components such as a Lüneburg lens is discussed and MZI test structures based on a 2D metamaterial lattice are proposed. The design of the adiabatic structures for SWG structures interface to conventional waveguides is explained. The MZI test structures on the base of 2D metamaterial is introduced and simulations are performed. The mask layout procedure using Pyxis Mentor Graphic tools is described.

In Chapter 5 the fabricated structures are verified using the SEM images and the experimental set up are given. The analysis of the experimental results is discussed and compared with the prediction of simulations.

Chapter 6 summarises the most important points arising in the thesis, draws some conclusions and makes recommendations for further work.

The Photon Design suite and Mentor Graphics provided the principal tools that were used, including:

1. FimmWave & FimmProp (Eigenmode Expansion Method [20]), for the simulation of planar waveguide elements;
2. OmniSim (Finite Difference Time Domain [21]) for the simulation of the Lüneburg lens; and,
3. CrystalWave (Photonic Band Structure Solver extension of OmniSim) for the simulation of the metamaterial structures.
4. Pyxis Mask layout tools.

These tools were supplemented by custom MatLab scripts and Ample. A Python script was written to automate the quantisation of continuous refractive index profiles to metamaterial atom size. An Ample script was written to fully automate the mask layout drawing in Pyxis.

1.4 Original Contributions and Achievements

The thesis contributes to the advancement of the field of photonic integrated circuits through both original contributions and the critical analysis of current knowledge. The contributions of the author include:

1. A critical analysis of current knowledge of metamaterial and SWG structures.
2. The clarification of the homogenisation methods for metamaterial analysis and component design.
3. Test structure designs and implementation.
4. Mask layout of the designed structures.
5. Introducing a MMI polarisation splitter based on the Talbot effect in a SWG structures.
6. Test, measurement and analysis of the fabricated devices.

The results presented in this thesis were obtained during a period of study at the University of Ottawa for a PhD. degree from Fall 2013 to Fall 2017 under the supervision of Dr. Trevor J. Hall. This work is to the best knowledge of the author original. The following publications related to this thesis research were published during this period.

Appearing in this thesis

1. H. Nikkhah, T. J. Hall, 'The Talbot Effect in a Metamaterial', The 8th International Conference on Metamaterials, Photonic Crystals and Plasmonics META 2017, Incheon, South Korea, August 2017 (*invited*). Published as:
   H. Nikkhah, M. Hasan, T. J. Hall, 'The Talbot effect in a metamaterial', Applied Physics A, **124**:106, January (2018), (9 pages). https://doi.org/10.1007/s00339-017-1521-1
2. H. Nikkhah, T. J. Hall, 'Subwavelength grating waveguides for integrated photonics', Applied Physics A, 2016, **122**:368 , pp. 1-6.
3. H. Nikkhah, T. J. Hall, 'Subwavelength Grating Waveguide Design Rules for Integrated Photonics', IEEE Proceedings of the 9th International Congress Advanced

Electromagnetic Materials in Microwaves and Optics (Metamaterials 2015), Oxford, United Kingdom, 7-12 September 2015 , pp. 460-462.

Publications preceding the results in this thesis

4. H. Nikkhah, T. J. Hall, 'Metamaterial Waveguide Analysis and Test-Structures for Si Photonics', IEEE Proceedings of the 12th International Conference on Group IV Photonics (GFP), 2015, Vancouver, Canada, pp. 53-54.
5. H. Nikkhah, T. J. Hall, 'Metamaterial Lüneburg lens for Fourier optics on-a-chip', Proceedings SPIE OPTO, Integrated Optics: Devices, Materials, and Technologies, 2014, Photonics West, San Francisco, United States, pp. 89880J-89880J.

Contributions not directly related to this thesis

6. M. Hasan, J. Hu, H. Nikkhah, T. J. Hall, 'A photonic circuit for complementary frequency shifting, in-phase quadrature/single sideband modulation and frequency multiplication: analysis and integration feasibility', Journal of Modern Optics 2017, **65**(14), pp. 1386-1397.
7. R. Maldonado-Basilio, M. Hasan, H. Nikkhah, S. Abdul-Majid, R. Guemri, F. Lucarz, J. L. de Bougrenet de la Tocnaye, T.J. Hall, 'Electro-optic up-conversion mixer amenable to photonic integration', Journal of Modern Optics, **62**(17), 2015, pp. 1405-1411.

Chapter 2. Second Homogenisation

2.1 Introduction

In chapter 1 the development of PICs for the enhancement of photonic systems was discussed and the importance of footprint size minimisation by the replacement of bulky 3D optical components by planar components amenable to integration was stressed. First homogenisation over the atomic scale was described as an established means of summarising the electromagnetic properties of a crystalline material pertinent to a macroscopic scale while eliminating microscopic detail by field averaging over the unit cell. First homogenisation introduces a continuous medium that has equivalent electromagnetic properties as the original discrete medium in respect of the averaged fields and an emergent electromagnetic identity defined by the auxiliary polarisation and magnetisation vectors. First homogenisation effects an enormous simplification of the description of the propagation of electromagnetic waves in natural materials at frequencies lower than the x-ray region of the spectrum. This simplification is critical to a practical component design process.

A metamaterial consists of an arrangement of 'atoms' large enough to possess an electromagnetic identity on a lattice with subwavelength lattice constants. The implication of the word 'metamaterial' is that its macroscopic properties can also be summarised by a second field averaging step to introduce a continuous medium with electromagnetic properties not readily found in nature. The ability to engineer these properties offers an opportunity for breakthroughs in photonic integrated components. Photonic components often have dimensions large compared to the operating wavelength while the metamaterial's lattice has dimensions small compared to the wavelength. These disparate scales ensure that electromagnetic simulation tools are challenging in terms of the provision of necessary computer resources. A systematic component design and optimisation process is rendered intractable.

This chapter addresses this problem by introducing second homogenisation in the close to Bragg resonance long wavelength regime for metamaterials with 1D and 2D lattice structure.

2.2 Contribution

The results provided in the first part of this chapter are published in an IEEE conference publication. In the paper the homogenisation of sub-wavelength grating structures is discussed and simple design rules are introduced to model their properties. In the second part of the chapter adds new original results on the homogenisation of 1D SWG structures and their anisotropic and spatially dispersive properties. I drafted the paper, performed the simulations, observed the artefact of the effective mode index vs. fill factor that appears at the short wavelength end of the operating wavelength range but is absent at the longer wavelength end; performed the analysis and contributed the original idea for the polarisation

beam splitter. Dr. Hall contributed to the theory; provided advice, assisted with the interpretation of the results, and helped with the Matlab codes and manuscript revision.

2.3 Article

The following section is a reproduction of an article published in the IEEE Proceedings of the 9th International Congress on Advanced Electromagnetic Materials in Microwaves and Optics (Metamaterials 2015), Oxford, UK [21].

H. Nikkhah, T. J. Hall, 'Subwavelength Grating Waveguide Design Rules for Integrated Photonics', Proceedings of the 9th International Congress Advanced Electromagnetic Materials in Microwaves and Optics (Metamaterials 2015), Oxford, United Kingdom, 7-12 September 2015 , pp. 460-462.

Subwavelength Grating Waveguide Design Rules for Integrated Photonics

H. Nikkhah, T. J. Hall

Photonics Technology Laboratory, Centre for Research in Photonics, University of Ottawa, School of Electronic Engineering & Computer Science, Advanced Research Complex, 25 Templeton Street, Ottawa, ON K1N 6N5 CANADA

Abstract – A recent break-through in the domain of photonic integration is the use of sub-wavelength waveguide grating structures to engineer the refractive index of integrated components. These structures are an example of a case where a nanoscale simulation over the full device is not reliable and reliance must be placed on a simple design procedure. This paper reports a study of the homogenisation of sub-wavelength waveguide grating structures. It is shown how the properties of these waveguides may be accurately modelled using simple design rules. A justification for these rules is found from the exact theory by a judicious choice of approximations. The temporal and spatial dispersive properties of the subwavelength grating waveguide are also evidenced.

I. INTRODUCTION

The designer of a photonic integrated circuit is fortunate to have access to a wide variety of software tools. It is important to emphasise that the tools assist the design process by verifying through simulating the behaviour of a preliminary design. Some tools support automatic refinement of a design using an optimisation algorithm. However, the design problem is typically so complex that any automated optimisation can at best be accomplished starting from a good preliminary design. There is therefore no substitution for the intuition of the designer in an iterative –design-verification cycle and the application of design rules to the formulation of the initial design. Simplifications of the theory backed up by experimental results are critical to the acquisition of intuition and the formulation of design rules.

Sub-wavelength waveguide grating structures (SWGs) have met with great success in reducing coupling loss, insertion loss and crosstalk; and increasing the operational bandwidth of on-chip components [1]. In photonic crystals (PhC), a waveguide is typically created by introducing a line defect. SWGs are a different sub-category of PhC, also known as metamaterials, which operate at frequencies below the band-gap and require no surrounding lattice to guide. The fundamental principle is the propagation of the Floquet-Bloch modes of the SWG. Components exploiting SWGs have two disparate scales to their structure; one small compared to the wavelength and one much larger than the wavelength. This provides an additional challenge to the designer because no single software tool spans the two scales. Current tools for simulation of wavelength scale structure (e.g. PhC or metamaterials) require sub-wavelength computational meshes that can only be applied to regions a few wavelengths in extent; whereas tools that can simulate devices many wavelengths in extent cannot be applied to sub-wavelength structures. The simulation of sub-wavelength nanostructure over scales of many wavelengths requires an abstraction of the properties of the nanostructure, which summarises its properties pertinent to the larger scale and smooths over the detail at the smaller scale. This abstraction is known as homogenisation.

There is a vast literature on homogenisation. Its classic roots are the Clausius-Mossotti equation [3] that links the electrodynamics of continuous media to their atomic structure and the mixing formulae of Maxwell-Garnet [4] for the constitutive parameters of composite materials. Early studies applied long-wavelength asymptotic approximations because all but simple problems, such as the 1D lamellar structure analysed by Rytov [5], are intractable theoretically. A resurgence of interest in homogenisation can be traced to Prof. Sir John Pendry's corpus of work on negative refractive index materials, first postulated by Veselago [6]; and to an influential paper by Smith & Pendry [7] in which they pointed out that the electromagnetic fields in a unit cell of a photonic crystal may be calculated advantageously by commercial tools; albeit there remains additional coding to complete the homogenisation. The method of Smith & Pendry has been shown to be flawed in certain

circumstances [8]; but that of Pérez-Huerta et al. [9], which draws on early work by Mochán & Barrera [10], and Mochán et al. [11] is compelling.

This paper reports a study of the homogenisation of sub-wavelength waveguide grating structures. It is shown how the properties of these waveguides may be accurately modelled using simple design rules. A justification for the design rule is found from the exact theory by a judicious choice of approximations. The temporal and spatial dispersive properties of the subwavelength grating waveguide are also evidenced. Care is required in coherent applications, such as microwave frequency multiplication, advanced I-Q modulation, and optical hybrids for coherent receivers, to control the phase of light propagation. This leads to a desire to engineer the dispersion and anisotropy of an SWG MMI so that a practical device provides close to ideal behaviour.

II. PHENOMENOLOGICAL MODELLING AND SIMULATION

A slab waveguide with a core patterned as a photonic crystal in one-dimension (i.e. a 1D grating) is under study. The effective index of a mode propagating in the plane of the grating in a direction substantially normal to the grooves has been modelled by three different techniques. In the first technique ("Kronig-Penney") the 1D Kronig-Penney model is used to predict the homogenised index of a two dimensional photonic crystal of infinite extent. This is compared with the predictions of the Photon Design CrystalWave 2D band-solver applied to a 2D unit cell with an artificial periodicity in the direction parallel to the grooves. Good agreement between the band structures predicted by both methods is obtained even for propagation at an angle to the normal as found in a standard slab waveguide.

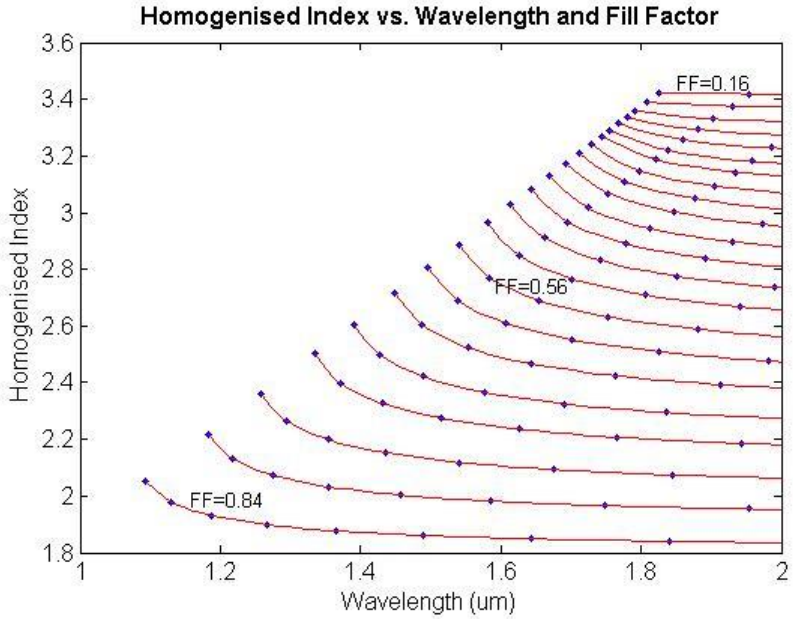

Figure 1. Homogenised index against wavelength and fill factor (FF) for the1D Kronig-Penney photonic crystal structure.

The homogenised index found thereby (see Figure 1) is then used as the core index in a standard asymmetric slab waveguide model to predict a value of the effective index of the guided mode as a function of frequency and wave-vector. In the second technique ("Lamellar"), the effective index of the mode is found directly using a 2D band solver from a specially constructed 2D unit cell. This unit cell introduces an artificial periodicity in the direction normal to the plane of the slab. Care is taken to ensure that the modal fields have decayed to negligible proportions between repeats of the structure in this direction. The third technique ("3D unit cell") is similar but uses a 3D band solver and a 3D unit cell in which an artificial periodicity is introduced in the direction parallel to the grating grooves. Figure 2 shows the comparison of the results of the three models at wavelength 1.5 μm for E_x mode propagation. The 3D unit cell and Lamellar models are in good agreement

however the Kronig-Penney model does not agree over the range of fill factor (fraction of period that is air) from 0.4 to 0.8 where the waveguide operates close to the band edge (near Bragg resonance). This is caused by the neglect of the transverse component of the wave vector of the plane wave pair that forms a mode of a slab waveguide. The region with fill factor less than 0.4 then corresponds to operation within the band-gap of the Kronig-Penney model rendering the method invalid despite the appearance of good agreement in that region.

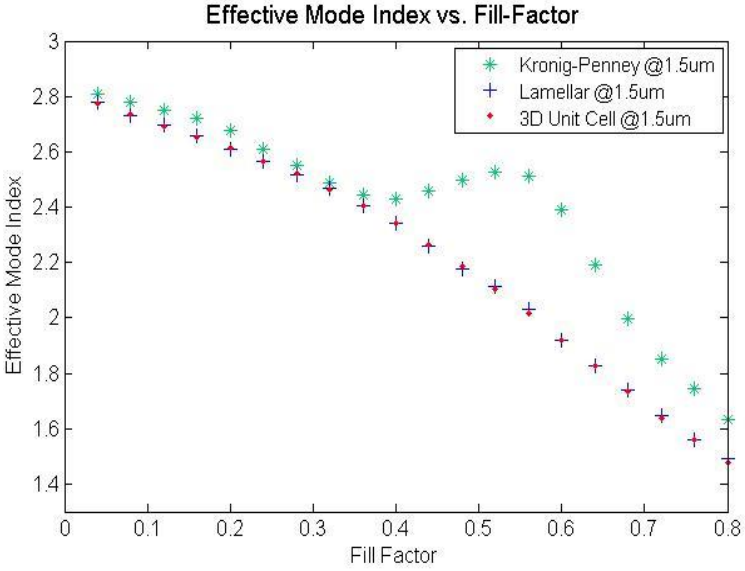

Figure 2. The effective mode index against fill factor (fraction of grating period occupied by air) for the three models at the wavelength of 1.5 μm for E_x like mode (normal incidence assumed in Kronig Penney model).

Figure 3 shows the same comparison as Figure 2 but at the longer wavelength of 2.5 μm. There is good agreement between all three methods in this long wavelength region where the neglect of the transverse wave vector of the plane waves within the waveguide is more justified. Figure 4 shows the same comparison as Figure 2 but with a non-zero self-consistent component of the transverse wave vector used in the Kronig-Penny model. All three methods are then in close agreement over a wide range of frequency. The agreement is found to be accurate even for vacuum wavelengths approaching the 'slow light' region close to the band-edge.

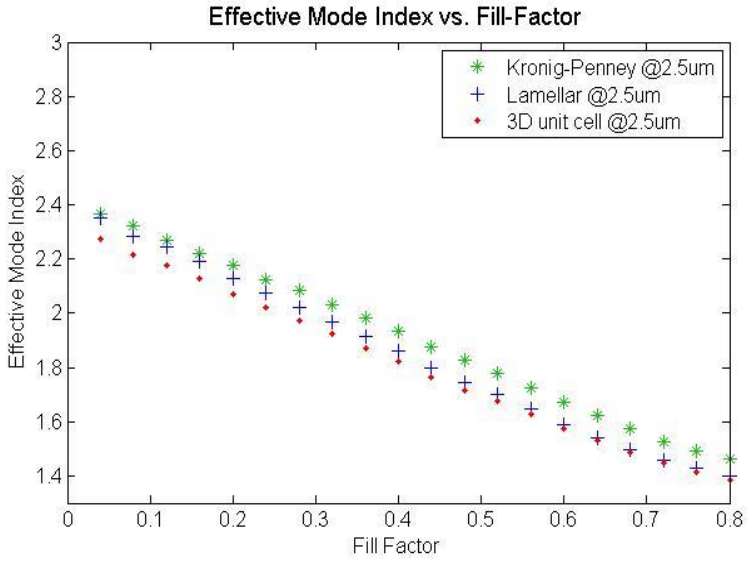

Figure 3. The effective mode index against fill factor for the three models at the wavelength of 2.5 μm for E_x like mode (normal incidence assumed in Kronig-Penney model).

A similar simulation study has been performed with a slab waveguide with a core patterned as a 2D photonic crystal with a hexagonal lattice. The hexagonal lattice is chosen as this offers circular equi-frequency contours in the long wavelength limit. In this case, a 2D band solver is used to predict the homogenised index of a 2D photonic crystal of infinite extent. This homogenised index is then used as the core index of an asymmetric slab waveguide to predict the effective index of the bound mode. This result is then compared to a direct calculation by a 3D band-solver applied to a 3D unit cell (see Figure 5) defined by periodically replication in the out of plane direction a single 2D unit cell in the plane of the waveguide structure. The out-of-plane period is chosen large enough that the waveguide fields are negligible at the boundaries of the cell.

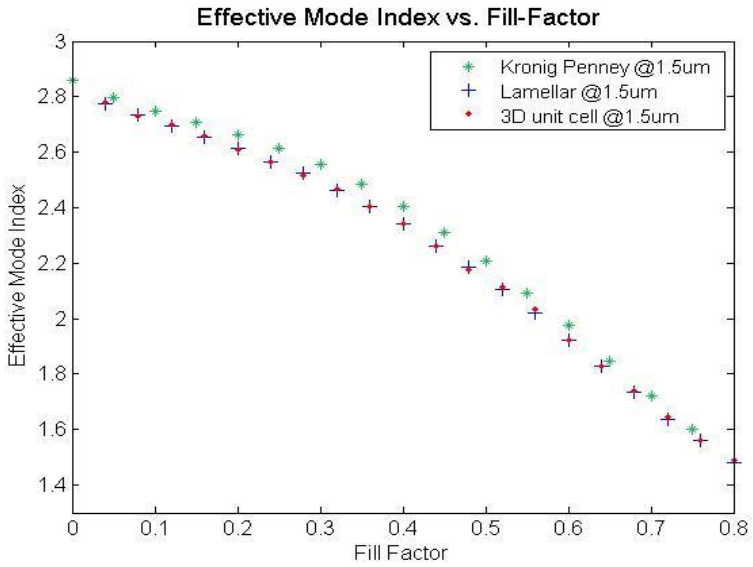

Figure 4. The effective mode index against fill factor for the three models at the wavelength of 1.5 μm for E_x like mode, (non-normal incidence in the Kronig-Penney model).

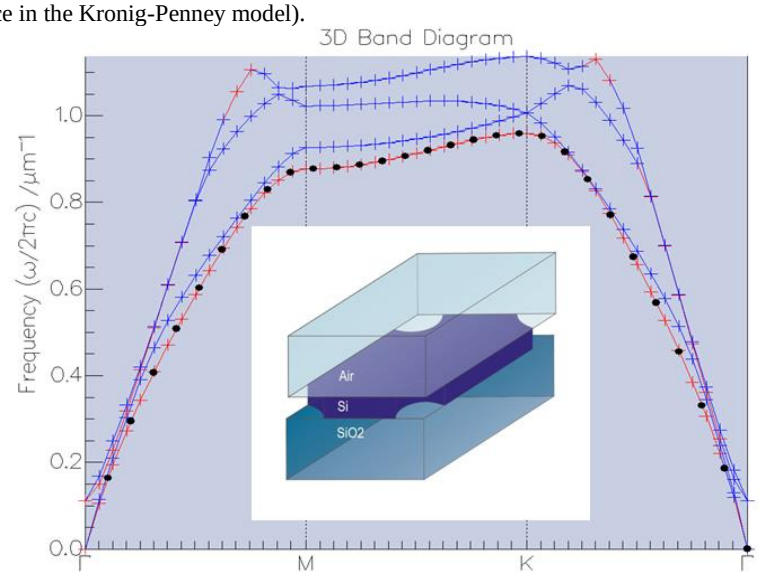

Figure 5. The 3D unit cell contains of three layers of air, silicon and silica with the thickness of 2 μm, 0.35 μm and 2 μm respectively and the 3D photonic crystal band diagram for TE (red), also highlighted by the bold dots) and TM (blue) polarisations for silicon holes of diameter 180 nm on a regular hexagonal unit cell with a lattice constant of 250 nm.

Remarkably, the indirect and direct methods agree closely for both the 1D and 2D photonic crystal cores of the slab waveguides. This indicates that the evanescent fields generated at the core boundaries do not significantly tunnel across thickness of the core and that the field continuity conditions at the core boundaries differ little

from continuous media. Whereas the indirect method must be corrected for spatial dispersion by taking into account the transverse wave vector of the guided mode, no correction for spatial dispersion appears to be necessary for the 2D photonic crystal core. The advantage of the slab grating waveguide is that there is a well-developed rigorous coupled wave analysis that can be adapted to the grating waveguide case. In the regime of interest it is found that only one Bloch mode has significant amplitude and the continuity conditions at the interfaces simplify into essentially those that describe a standard asymmetric waveguide thereby justifying the indirect homogenisation approach in the case of the 1D photonics crystal core and providing credence in the case of the 2D photonics crystal core.

To fully exploit the flexibility offered by SWG they need to be formed into waveguides of finite width and integrated and interconnected by conventional waveguides. Adiabatic structures must be provided that adapt waveguide dimensions and the homogenised index. The latter can be achieved by preserving the local periodicity of the photonic crystal structure while varying the geometrical parameters of the structure on a scale large compared to the lattice constants [2]. Figure 6 shows an example of a Mach-Zehnder interferometer (MZI) with SWG arms adapted to standard silicon waveguides by adiabatic tapers. The imbalance between the arms allows the experimental measurement of the homogenised index. These structures are an example of a case where a nanoscale simulation over the full device is not reliable and reliance must be placed on a homogenisation procedure. The experimental confirmation of the validity or otherwise of the procedure awaits the MZI structures to come out of fabrication.

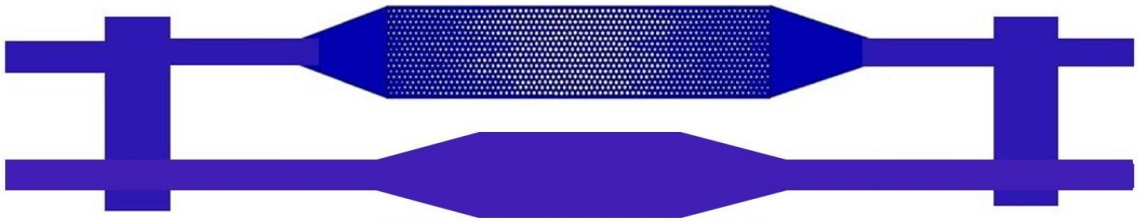

Figure 6. MZI structure with one arm patterned structure and the other arm silicon. The pattern structure contains of holes with the varying diameters from 10 nm to 180 nm in silicon layer.

III. Conclusion

In this paper a study of the homogenisation of sub-wavelength waveguide grating structures described. The properties of waveguides may be modelled using simple design rules. The design rule is found to be justified as an approximation to the precise theory. The temporal and spatial dispersive properties of the subwavelength grating waveguide are also evidenced. The continuing improvement in advanced lithography techniques (such as immersion lithography, extreme-UV lithography, nano-stepping lithography) will enable accurate, large-volume production of SWGs expanding their use in integrated photonics enabling new functionalities and devices to be designed and fabricated.

Acknowledgement

The authors are grateful to Tom Davies of Technix for very helpful technical discussions. Trevor Hall is grateful to the support provided by his Canada Research Chair Tier I in Photonic Network Technology.

References

[1] R. Halir, *et al*., "Waveguide sub-wavelength structures: a review of principles and applications," Laser & Photonics Review, 9.1, 25-49, 2015.
[2] J. H. Hannay, "The Clausius-Mossotti equation: an alternative derivation," Europ. J. Phys, 4, 141-143, 1983.
[3] J. C. Maxwell Garnett, "XII. Colours in metal glasses and in metallic films," Phil. Trans. Royal Soc. A, 203, 385-420, 1904.
[4] S. M. Rytov, "Electromagnetic properties of a finely stratified medium," Sov. Phys. JETP, 2, 466-475, 1956.
[5] V. G. Veselago, "The electrodynamics of substances with simultaneously negative values of ε and μ," Sov. Phys. Usp. 10, 509-514, 1968.

[6] D. R. Smith, J. B. Pendry, “Homogenization of metamaterials by field averaging (invited paper),” J. Opt. Soc. Am. B, 23(3), 391-403, 2006.
[7] V. V. Gozhenko, A. K .Amert, K. W Whites, “Homogenization of periodic metamaterials by field averaging over unit cell boundaries: use and limitations,” New J. Physics, 15, art. 043030, 2013.
[8] J S Pérez-Huerta, G. P. Ortiz, B. S. Mendoza, W. L. Mochán, “Macroscopic optical response and photonic bands,” New J. Physics, 15, art. 043037, 2013.
[9] W. Mochan, R. G. Barrera, “Electromagnetic response of systems with spatial fluctuations. I. General formalism,” Phys. Rev. B, 32(8), 4984-4988, 1985.
[10] W. L. Mochan, G. P. Ortiz, B. S. Mendoz, “Efficient homogenization procedure for the calculation of optical properties of 3D nanostructured composites,” Opt. Exp., 18(21), 22119-22127, 2010.
[11] C. Fietz,Y. Urzhumov, G. Shvets, “Complex k band diagrams of 3D metamaterial / photonic crystals,” Opt. Exp., 19(20), 19027-19041, 2011.
[12] H. Nikkhah, T. J. Hall, “Metamaterial Lüneburg lens for Fourier optics on-a-chip,” SPIE OPTO. International Society for Optics and Photonics, 2014.

2.4 Field Averaging

Optical systems and components have been implemented traditionally using 3D free-space optics and discrete components; leading to bulky optical systems that are vulnerable to environmental perturbations, possess stringent alignment tolerances, and unsuited to volume manufacture. These issues may be addressed by omitting one dimension and implementing the structures on a planar slab waveguide of a silicon integration platform with the advantage of a smaller footprint. For example, the classical 3D optical Lüneburg lens may be implemented in 2D as a slab waveguide gradient index lens to provide a Fourier transform on a chip for a complex optical interconnection system [22]. For a clearer illustration, consider a planar slab waveguide with solid core, such as silicon, with air as the upper cladding and silica as substrate which together form an asymmetric 1D slab waveguide. The light is confined in the direction normal to the plane but the wave-vector of the fundamental mode can be pointed in any direction in a 2D free-space within the plane [22]. The value of the effective index the fundamental mode experiences is lower than the refractive index of the core and higher than the substrate for the light to be confined in the core of the waveguide. To vary the effective index of the mode, a careful selection is needed of the core and cladding materials, their thickness and the operating vacuum wavelength. Hence, to construct a structure such as a lens, where the effective index varies radially from the centre of the lens to its rim, the thickness of the slab waveguide must be varied to fulfill the specified graded refractive index profile which requires multiple steps of etching that would add complexity and high cost to the fabrication process.

However, recent advancements in fabrication, such as E-beam lithography, have enabled sub-wavelength scale nanostructuring of a binary composite material that may decrease the cost and complexity of the fabrication process by offering a single etch step. The binary composite material consists of inclusions of one material within a different material as a host and the composition is adjusted by varying the fill factor to define the effective index of the composite somewhere between the refractive indices of the two materials. The effective index seen by the mode then may be defined by the local effective medium index of the composite in the core layer of the slab waveguide and the upper and lower claddings. As the patterning is on a subwavelength scale, the propagating wave sees the composite as a homogeneous medium with an effective index predicted by a simple mixing formulae [23]:

$$n_{eff}^2 = n_h^2 \frac{(1+2f)n_i^2+2n_h^2(1-f)}{(1-f)n_i^2+(2+f)n_h^2} \tag{2.1}$$

where f is the fill-factor, and n_h, n_i are the refractive indices of the host and inclusion respectively.

In contrast, the lattice constant in photonic crystal structures is close to half a wavelength and hence operation is in the resonance regime. A locally perfect periodic distribution of inclusions supports lossless Floquet-Bloch modes which satisfy a dispersion relation that

displays a photonic band gap in a range of frequencies about a Bragg resonance. To avoid the band-gap, the period of the inclusions must be sufficiently sub-wavelength to avoid the resonance phenomena caused by Bragg scattering which is responsible for the curvature of the band diagram towards the band edge. The curvature of the band diagram complicates design as there is no simple mixture formula for the effective index under such conditions. This is illustrated clearly in Figure 2.1 [22].

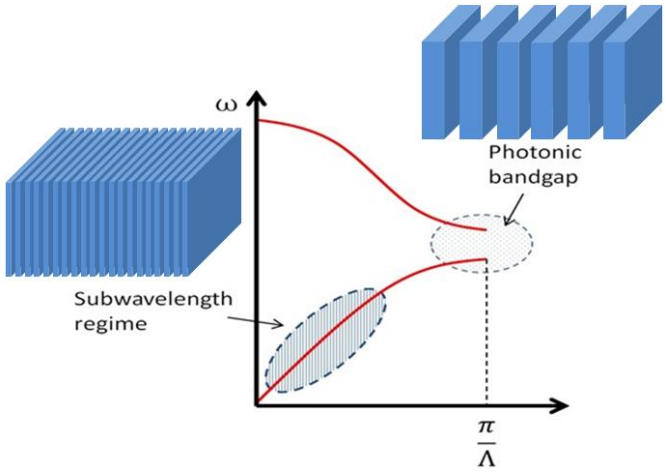

Figure 2.1 A band diagram showing the operating region of photonic crystal structures in the bandgap region and metamaterial structures in the low frequency linear region. The pitch of the periodic multilayer dielectric stack is about the half wavelength in photonic crystals but is less than half the wavelength in metamaterial structures.

In this work, the metamaterial structure is built using a SOI material platform consisting of a 300 nm layer of silicon over a 2μm buried oxide layer on a silicon wafer. The slab waveguide formed by the silicon layer with air upper cladding and silica lower cladding is patterned in a single step etch process to form air inclusions within the core material. The inclusions may form a 1D structure of consisting of a multilayer silicon stack separated by air-slots or a 2D structure of cylindrical air holes in a silicon layer. The width of the stacks or the diameter of the cylinders may vary over a regular lattice.

The challenge to design a subwavelength nanostructure is the requirement of very fine subwavelength computational grids in the simulation tools which becomes a big issue in terms of the provision of the necessary computer resources for devices large compared to the wavelength. Hence, simple design rules are essential to the formulation of a good starting point. An abstraction procedure, which is known as homogenisation, is required to summarise the properties of the nanostructure pertinent to a larger scale and eliminate the unnecessary details at the nanoscale. Conceptually, one is able to replace the metamaterial by an effective continuous medium that enables a larger scale view of electromagnetic wave propagation in the metamaterial through the bulk of the material and at its surface. The classical roots of homogenisation are the Clausius-Mossotti equation that connects the electrodynamics of continuous media to its atomic structure and the Maxwell-Garnet mixture

formulae for the parameters of the composite materials [23]. If Maxwell's equations for a continuous media with the standard boundary conditions at interfaces are defined locally by:

$$\boldsymbol{d} = \boldsymbol{\varepsilon e} \quad ; \quad \boldsymbol{b} = \boldsymbol{\mu h} \tag{2.2}$$

where $\boldsymbol{e}$ and $\boldsymbol{h}$ are the microscopic electric and magnetic fields and $\boldsymbol{\varepsilon}$ and $\boldsymbol{\mu}$ are the permittivity and permeability respectively, then for a homogenised medium the constitutive equations relate the macroscopic fields defined by averaging of the microscopic fields:

$$\begin{gathered} \boldsymbol{E} = \langle \boldsymbol{e} \rangle \quad ; \quad \boldsymbol{H} = \langle \boldsymbol{h} \rangle \\ \\ \boldsymbol{D} = \boldsymbol{\varepsilon E} + \boldsymbol{\xi H} \\ \boldsymbol{B} = \boldsymbol{\zeta E} + \boldsymbol{\mu H} \end{gathered} \tag{2.3}$$

In the preceding, classical methods of homogenisation were reviewed from the perspective of first solving the microscopic problem and then applying an averaging procedure to obtain the solution to the macroscopic problem. Except in some limiting cases the classical methods reach approximate solutions due to simplifications to:

1. the description of the microstructure;
2. the neglect of retardation;
3. the averaging procedure.

Formerly, these simplifications were necessary for reasons of tractability but, today, routine access to powerful computers means that detailed calculations may be performed numerically. Band-structure calculations are routine for photonic crystal structures. Band structure data provides a complete description of the optical properties of a photonic crystal and as a consequence it appears in some guise within a modern homogenisation procedure for periodic structures. Indeed homogenised parameters for the bulk may be extracted directly from band structure data. In developing homogenisation procedures, it is therefore a consideration that the computation involved is less than a full band-structure calculation. Homogenisation should also offer, more readily than band-structure calculations, the constitutive relations needed to adequately describe transmission and reflection at interfaces. It is also important to gain insight into surface boundary layer effects and residual scattering.

The focus of the sequel is on periodic composite structures where the constituent entities are large enough on the atomic scale to possess a dielectric identity but small enough compared to the wavelength that a homogenised description is appropriate. A specification of the optical properties on a unit cell provides a complete description of the microstructures as a whole (thus addressing item 1 in the preceding). The equations subject to homogenisation are Maxwell's equations in full[1] (thus addressing item 2 in the preceding) or their reduced electrostatic form when retardation is not important or when other reduced forms are convenient for pedagogical reasons.

[1] That is Maxwell's equations homogenised over the atomic scale. The object of study here is a second homogenisation procedure over a sub-wavelength scale.

Attention now turns to the specification of the averaging procedure. Let ψ be an arbitrary function of space. It may always be decomposed into a sum of a smooth part ψ_s and a fluctuating part ψ_f. Denote by $\mathcal{P}$ and $\mathcal{Q}$ the operations of extracting the smooth and fluctuating components:

$$\begin{aligned} \mathcal{P}&: \psi \longrightarrow \psi_s \\ \mathcal{Q}&: \psi \longrightarrow \psi_f \end{aligned} \tag{2.4}$$

To agree with intuition, these operators must be idempotent:

$$\begin{aligned} \mathcal{P}^2 &= \mathcal{P} \\ \mathcal{Q}^2 &= \mathcal{Q} \end{aligned} \tag{2.5}$$

That is the smooth part of the smooth part of some function is its smooth part and the fluctuating part of the fluctuating part of some function is its fluctuating part.

It is also desirable $\mathcal{P}$ and $\mathcal{Q}$ are chosen to be linear to preserve the linear properties of the governing equations and to ensure that no error is introduced by the decomposition:

$$\begin{aligned} \mathcal{P}\psi + \mathcal{Q}\psi &= \psi \\ &\Longrightarrow \\ \mathcal{Q} &= I - \mathcal{P} \\ \mathcal{P}\mathcal{Q} &= \mathcal{Q}P = 0 \end{aligned} \tag{2.6}$$

In the classical theory, the methods of averaging include ensemble averaging for random structures and volumetric averaging for regular structures. Volumetric averaging involves integration over a volume centred on a particular point. As this point is moved, the result is a convolution. A convolution in real space may be implemented as a multiplication by a function in Fourier space (reciprocal space) that filters the spatial frequency components of the Fourier transform of the function being smoothed. To satisfy the idempotency requirement, the filter function must either take the value unity or zero. To satisfy the notion of smoothing $\mathcal{P}$ should correspond to an ideal low-pass spatial filter. The support of the filter function determines those spatial frequencies that are passed by the convolution and those that are rejected. In the case of a periodic structure it makes sense to choose the first Brillouin zone as the support – this corresponds to the least smoothing consistent with the rejection of the microscopic detail. Of course smaller supports may be used if lower spatial frequencies are of primary interest.

The compact support in Fourier space leads in real space to a smooth (differentiable) convolutional kernel of infinite extent – albeit square integrate-able and therefore falling-off towards infinity. This has the added advantage that the projections commute with the spatial derivatives thereby ensuring that the homogenised equations preserve the same form as the microscopic equations; an important requirement of a homogenisation procedure. Integration over a finite volume is consequently not idempotent. Whereas little error may be introduced when homogenising over atomic scales, the idempotency requirement is likely critical to the success of sub-wavelength scale homogenisation. However, the boundary layer either side of

a photonic heterojunction in which the field evolves from the Bloch-Floquet-mode expansion of the interior of one medium to the Bloch-Floquet-mode expansion[2] of the interior of the other medium will extend over several unit cells and consequently be on the scale as the wavelength in contrast to the atomic scale of a natural material. As a consequence, the correct boundary conditions to apply to the averaged wave are not known and a continuous media definition of the wave-impedance $Z = \sqrt{\mu/\varepsilon}$ required by the Fresnel reflection formulae may give incorrect predictions of reflection and transmission coefficients especially when evaluated at reciprocal space points off the band structure manifold. These difficulties are by-passed conceptually in this thesis by averaging only transversely to an interface or by eliminating the interface by varying the parameters of the nanostructure adiabatically.

For a periodic metamaterial the field φ consists of a superposition of Floquet-Bloch modes of the form:

$$\varphi(\boldsymbol{x}) = \exp(i\boldsymbol{k}.\boldsymbol{x})\,\boldsymbol{u}(\boldsymbol{x}) \tag{2.7}$$

where $\boldsymbol{k}$ is the Bloch wave-vector $\boldsymbol{u}$ is a complex vector envelop that has the same periodicity as the lattice and hence may be represented by a Fourier series:

$$\boldsymbol{u}(\boldsymbol{x}) = \sum_{\boldsymbol{g}\in G} \boldsymbol{a}_g \exp(i\boldsymbol{g}.\boldsymbol{x}) \tag{2.8}$$

and $\boldsymbol{g}$ is a reciprocal lattice vector.

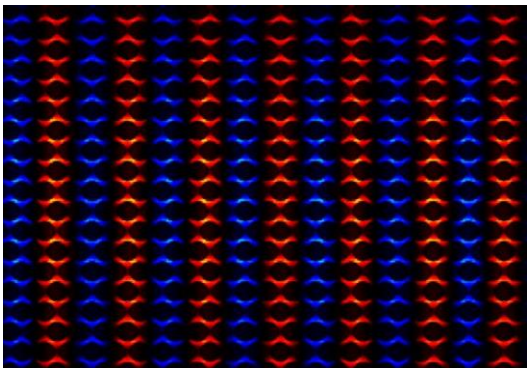

Figure 2.2 A 2D metamaterial structure with hexagonal lattice constant of 250 nm. The periodicity of the complex envelop of the Bloch mode are seen in the black features and the field average is seen in the red-blue plane wave fronts described by the Bloch wave-vector.

The exponential phase factor may range over the unit circle within a real space cell for a wavelength $\lambda \sim 2a$ where a is the lattice constant. This means that field averaging over a real space unit cell limits homogenisation to the deep long wavelength limit. Figure 2.2 illustrates field averaging over a 2D hexagonal lattice of a metamaterial structure visually, whereas the periodicity of the lattice imposed on the Bloch mode by the complex envelop u is plain by

[2] In the case of the interior of a continuous material the appropriate mode expansion is the Rayleigh expansion.

eye, the average over the structure can also be seen by eye to have the structure of a plane wave.

Taking the smoothing operator to be a perfect low pass filter with the first Brillouin zone as its passband, it is clear that its action on a Bloch mode is to extract the zeroth order term:

$$(P\varphi)(\boldsymbol{x}) = \varphi_s(\boldsymbol{x}) = \boldsymbol{a_0}\exp(i\boldsymbol{k}.\boldsymbol{x}) \tag{2.9}$$

and the action its orthogonal complement is simply to set the zeroth order term to zero while retaining all other orders.

$$(Q\varphi)(\boldsymbol{x}) = \varphi_f(\boldsymbol{x}) = \exp(i\boldsymbol{k}.\boldsymbol{x}) \sum_{\boldsymbol{g}\neq\boldsymbol{0}} \boldsymbol{a}_g \exp(i\boldsymbol{g}.\boldsymbol{x}) \tag{2.10}$$

Band structure calculations using the plane wave expansion method represent the Bloch modes by their Fourier series which thereby trivialises the implementation of the projections $\mathcal{P}$ and Q. Proceeding formally, write:

$$L\varphi = M\varphi \tag{2.11}$$

where L is a linear operator representing Maxwell's equations and M is a linear operator representing the constitutive equations of the detailed structure. Eq. (2.11) may be separated into two equations using the properties of the projections $\mathcal{P}$ and Q to yield:

$$PLP\varphi + PLQ\varphi = PMP\varphi + PMQ\varphi \tag{2.12}$$

$$QLP\varphi + QLQ\varphi = QMP\varphi + QMQ\varphi \tag{2.13}$$

Since P and Q are complementary orthogonal projections, $PLQ\varphi$ and $QLP\varphi$ are zero as P and Q commute with L and annihilate each other. Hence Eq. (2.13) may be formally inverted to solve for the fluctuating field in terms of the smoothed field:

$$Q\varphi = [QLQ - QMQ]^{-1}\, QMP\varphi \tag{2.14}$$

The right hand side of Eq. (2.14) is to be understood as short hand for the projection onto the fluctuating part of the output of an electromagnetic mode solver given the structure and microscopic properties of the metamaterial with the smooth field (a plane wave) as its source. Substitution of Eq. (2.14) into Eq. (2.12) then gives an equation in the smooth field only:

$$PLP\varphi = PMP\varphi + PMQ[QLQ - QMQ]^{-1}\, QMP\varphi \tag{2.15}$$

Comparison with Eq. (2.11) permits Eq. (2.15) to be summarised by an equation of exactly the same form as Maxwell's equations:

$$LP\varphi = \bar{\bar{M}}P\varphi \tag{2.16}$$

but with the microscopic constitutive relations M replaced by $\bar{\bar{M}}$ the homogenised constitutive equation:

$$\bar{\bar{M}} = PMP + PMQ[QLQ - QMQ]^{-1}\, QMP \tag{2.17}$$

It is important to note that $\bar{\bar{M}}$ is not simply the average PMP of M which appears as the first term of Eq. (2.17). The second term fully accounts for the multiple scattering by the nanostructure that converts the smooth incident field into the fluctuating field and then converts some of the fluctuating field back into the smooth field.

2.5 Subwavelength Grating Slab Waveguides Homogenisation Methodology (1D Lattice)

At the scale of photonic integrated devices and circuits, metamaterial structures are fabricated in the form of slab waveguides which confine the field in the direction normal to the wafer. The metamaterial slab waveguides may be based on either symmetric or asymmetric continuous media slab waveguides. Figure 2.3 shows an example of a metamaterial slab waveguide where the core consists of 1D multilayer silicon stack. In the case of a symmetric structure, the upper and lower claddings are the same material (here silica); when the slab waveguide is asymmetric the upper cladding (here air) differs from the lower cladding. The gaps may be filled with either air or silica or some other typically polymeric material.

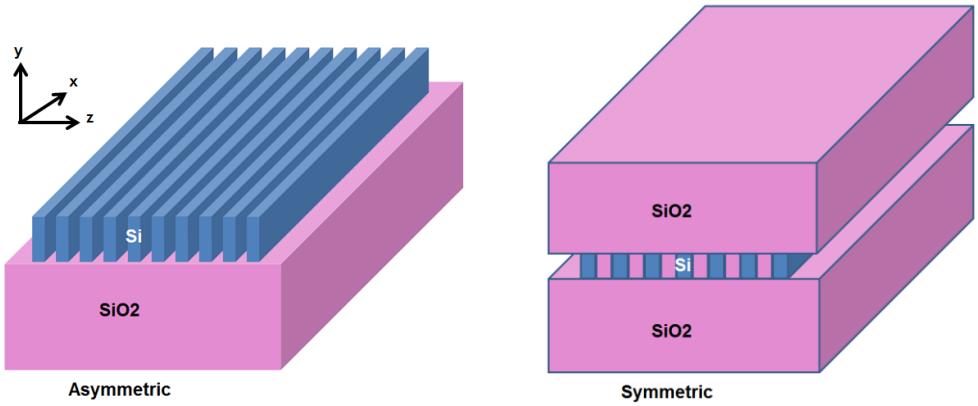

Figure 2.3 Metamaterial slab waveguide with a core consisting of multilayer silicon stack with the gaps filled with air or silica; (left) asymmetric slab waveguide with the upper cladding of air, and lower cladding of silica; (right) symmetric slab waveguide with the silica upper and lower cladding.

For structures such as these, it is difficult to apply a 3D simulation to the whole structure as a fine computational grid with points spaced at a nanometer scale yet spanning a device at a micrometer scale is needed which would consume massive computational resources (memory and time). Homogenisation would help to ease the design and analysis by modelling the periodic metamaterial structure as a continuous medium. Three different methods may be used to obtain the effective index of the metamaterial medium (3D unit cell, 1D to 2D waveguide confinement and Lamellar structure) that were first explained in detail in my Master's thesis [22]. For the structures shown in Figure 2.3, the Kronig-Penney model may be used to obtain the band structure of a 1D multilayer dielectric stack of silicon with air gaps semi-analytically [24]. Figure 2.4 shows the Kronig-Penney model where the optical axis is perpendicular to the stacks and along the propagation direction.

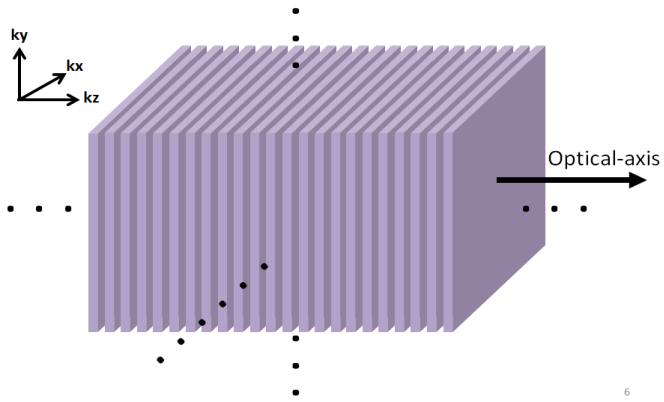

Figure 2.4 Kronig-Penney model consists of a 1D multilayer dielectric stack of silicon with air gaps which are extended to infinity along the x, y and z coordinates. The optical axis is perpendicular to the stack and along the propagation direction.

After first confirming agreement with a Kronig-Penney model band solver implemented in Matlab, the 2D band solver of the CrystalWave tool of the Photon Design software simulation suite is used to calculate the effective index of the fundamental Bloch mode in an extended 1D photonic crystal unit cell for specific fill factors. Figure 2.5 shows the band diagram of the Kronig-Penney multilayer stack for a grating period of 250 nm.

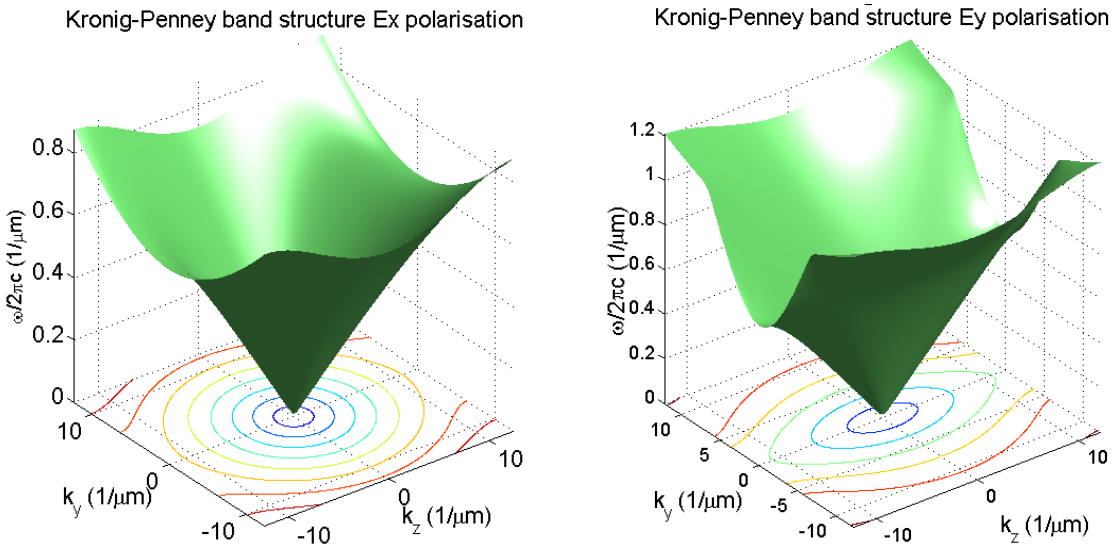

(a) (b)

Figure 2.5 Kronig-Penney band diagram for the grating period of 250 nm (a) ordinary mode, (b) extra-ordinary mode.

As the behaviour of the homogenised Kronig-Penney structure is anisotropic, the terms ordinary mode (circular equi-frequency contours) and extra-ordinary mode (elliptical equi-frequency contours) are used.

The effective index obtained by the 2D band solver is used as the refractive index of the core of a symmetric or asymmetric slab waveguide (Figure 2.6).

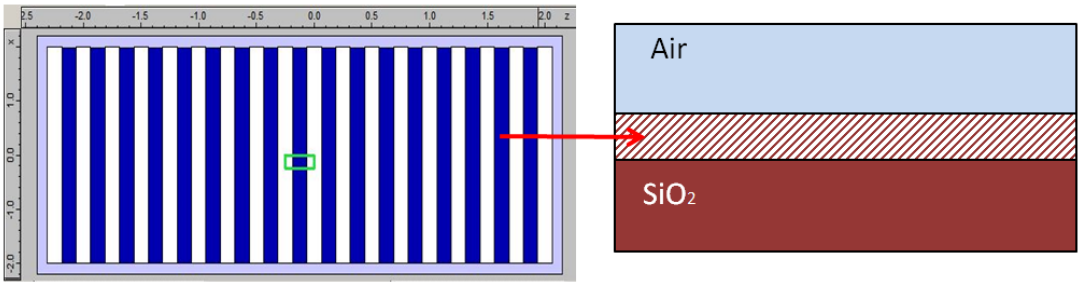

Figure 2.6 A 2D band solver is used to calculate the effective index of the fundamental Bloch mode in an extended 1D photonic crystal unit cell for a specific fill factor and then is used as the refractive index of the core of a continuous medium waveguide to obtain the effective index of the mode in the waveguide.

Due to the confinement in the waveguide and the constraints of the applied boundary condition, spatial dispersion correction is needed in a metamaterial waveguide to avoid the artefact caused by the path in reciprocal space entering the bandgap that was discussed in the paper in section 2.3. In a continuous medium slab waveguide, considering $k_x = 0$, the modal fields in the core consist of two plane wave components with wave vectors inclined at an angle to the optical axis (shown in Figure 2.7) with longitudinal component k_z and transverse component k_y . Since the homogenised metamaterial is anisotropic and spatially dispersive the index used for the core of the continuous medium waveguide must take account of the non-zero value of k_y. The value of k_y is found self-consistently by finding the intersection of the metamaterial band structure manifold and the slab waveguide dispersion relation manifold found by imposing the standard boundary conditions at the core-cladding interfaces of continuity of the tangential component of the electric and magnetic fields. This approach to correcting the core index to account for spatial dispersion neglects the complexity of the metamaterial structure at the slab core-cladding interface, and any lateral confinement which would introduce a non-zero value of k_x.

The path in reciprocal space corrected for spatial dispersion for a metamaterial waveguide with a 300 nm thick core consisting of 1D multilayer silicon stack normal to the optical axis with air gaps and a pitch of 250 nm is illustrated by the blue and yellow contours shown in Figures 2.8 and 2.9 for Ex-like and Ey-like modes respectively. In this analysis, the core refractive index is homogenised using the Kronig-Penney model. An Ex-like waveguide mode propagation in the z direction and confined in y direction corresponds to the ordinary polarised case for the Kronig-Penney model. Unlike a path along the k_z axis, which enters the bandgap at the operating wavelength of 1.55 μm, the trajectory illustrated by the blue and yellow lines in Figure 2.8 and 2.9 stays on the band structure manifold, consequently the Bragg resonance artefact that was observed in section 2.3 is avoided.

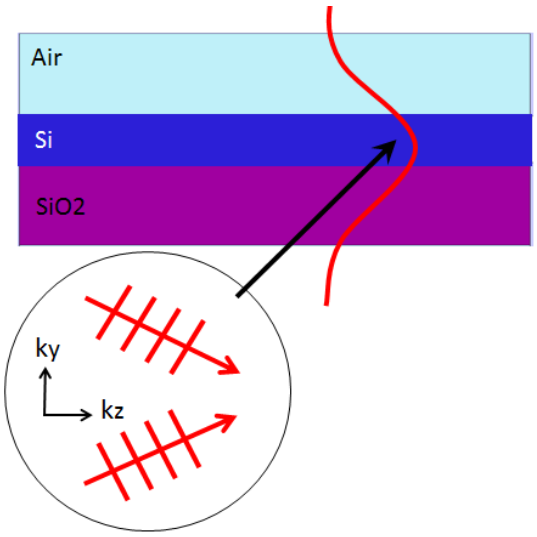

Figure 2.7 A side view of an asymmetric waveguide with three layers of air, silicon and silica top to bottom respectively. A guided mode in a slab waveguide homogeneous medium has two plane wave components in the core region with wave vectors that possess a longitudinal component of $\boldsymbol{k_z}$ and a transverse component of $\boldsymbol{k_y}$.

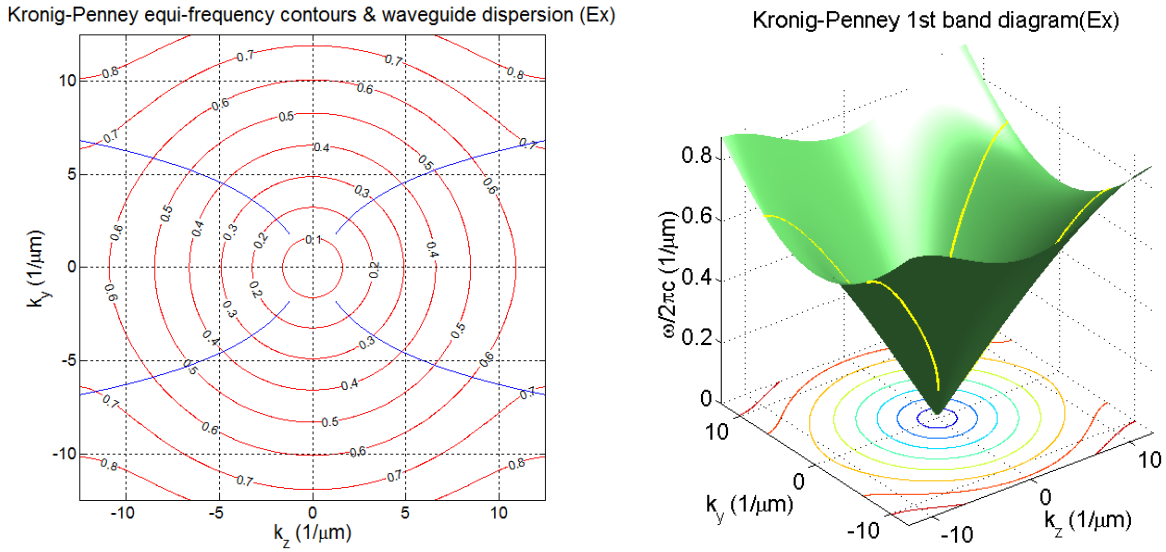

Figure 2.8 Waveguide dispersion relation solutions on the band structure manifold for Ex-like mode, for an asymmetric waveguide with a core 300 nm thick consisting of a 1D multilayer silicon stack with air gaps normal to the z-axis and a pitch of 250 nm and a fill-factor of 50% on an SOI platform with upper cladding of air and lower cladding of silica. The solution is shown (left) by blue lines on the equi-frequency contour plot, and (right) by yellow lines on band structure diagram.

The effective index of the Ey-like mode at lower frequencies is close to cut-off and the solver applies the correction to only the guided modes, hence the dispersion solution is not applied to lower frequencies as may be noticed in Figure 2.9. Figure 2.10 shows the confinement correction dispersion relation using the Kronig-Penney model for the core of the asymmetric

slab waveguide explained in the preceding with a comparison with data from a numerical experiment that applied the CrystalWave 3D band solver to the asymmetric slab waveguide with the multilayer silicon stack at the core. The plot for the Ex-like mode shows excellent agreement between the corrected dispersion relation and the CrystalWave data. As was mentioned above, for Ey the numerical method used is not able to follow the solution to low frequencies but the trend suggests that if the blue curve could be extended there would be excellent agreement in the long-wavelength regime. The divergence at the higher frequencies is most likely due to the neglect of the effect of the anisotropy of the core on the core-cladding boundary conditions that determine the waveguide dispersion relation. Although the breakage behaviour at the rim of the band diagram shown in Figure 2.11 at the right suggests that the CrystalWave data may also be unreliable in this region.

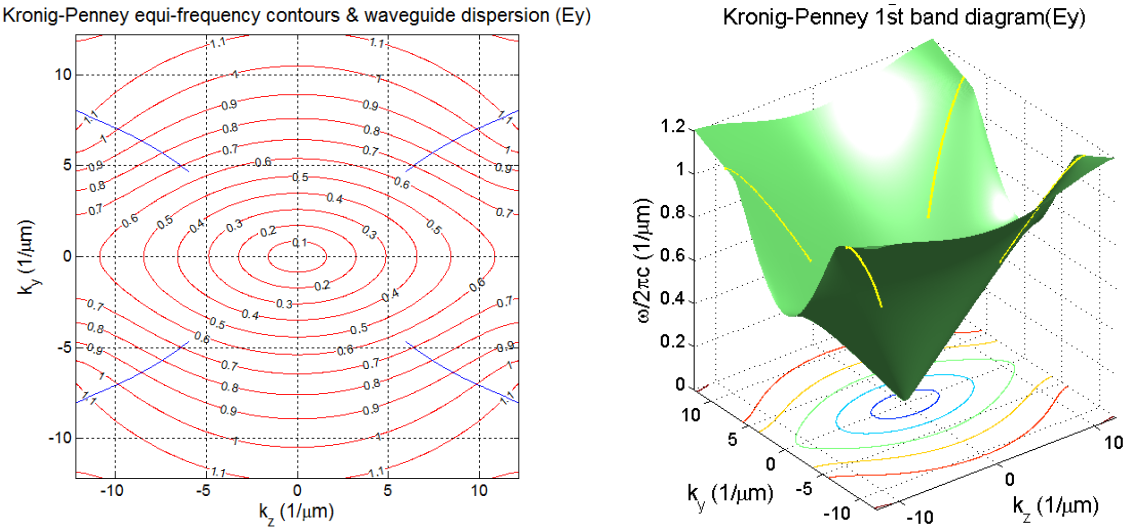

Figure 2.9 Waveguide dispersion relation solutions on the band structure manifold for Ey-like mode, for an asymmetric waveguide with a core 300 nm thick consisting of a 1D multilayer silicon stack with air gaps normal to the z-axis and a pitch of 250 nm and a fill-factor of 50% on an SOI platform with upper cladding of air and lower cladding of silica. The solution is shown (left) by blue lines on the equi-frequency contour plot, and (right) by yellow lines on band structure diagram.

Figure 2.11 shows the complete band structure and equi-frequency contours of the metamaterial waveguide for the Ex-like and Ey-like polarisations found by CrystalWave.

The effective permittivity of the ordinary and extra-ordinary mode in the Kronig-Penney model with silicon stacks and silica barriers at the wavelength of 1.55 μm is shown in Figure 2.12. In these plots k_t is the transverse component of wavevector which is perpendicular to k_z.

Figure 2.13 shows the effective permittivity of the ordinary and extra-ordinary mode in the Kronig-Penney model with silicon stacks and air barriers at the wavelength of 1.55 μm. It is seen that the permittivity is reduced in comparison with Figure 2.12 with silica barrier while the general behaviour is conserved.

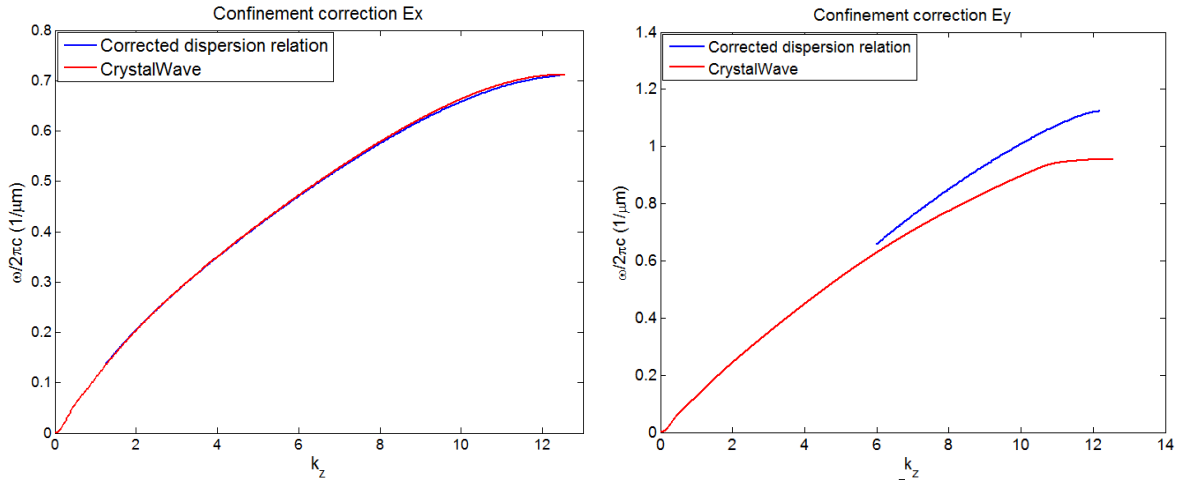

Figure 2.10 Confinement correction dispersion relation, using Kronig-Penney model in the core of a slab waveguide and CrystalWave 3D band solver; (left) Ex mode, (right) Ey mode.

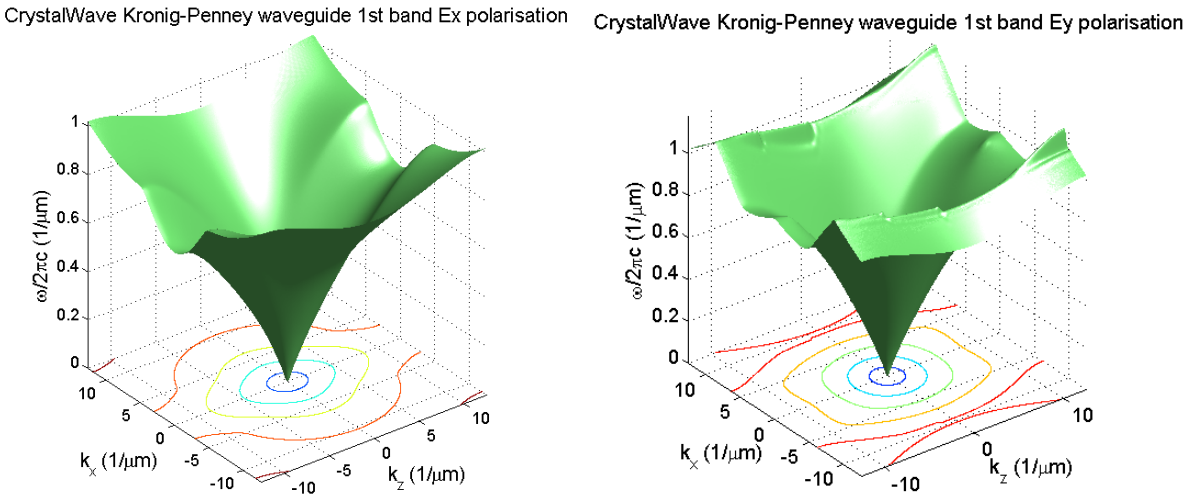

Figure 2.11 Band structure and equi-frequency contours of the dispersion corrected metawaveguide, (left) Ex-like polarisation, (right) Ey-like polarisation.

The homogenised dispersion relation of ordinary and extra-ordinary modes are shown in Figure 2.14 and 2.15 for silicon stacks and barriers of silica and air respectively for a shorter wavelength of 1.5 μm and longer wavelength of 1.55 μm. The homogenised dispersion relation shows the long wavelength anisotropic behaviour, near circular ordinary mode contours and near-elliptical extra-ordinary mode contours.

At longer wavelengths the contours open which illustrate the departure from local anisotropic behaviour (k-independent permittivity tensor) to manifestly spatially dispersive behaviour (k-dependent permittivity behaviour) and indicates the practical issue of achieving deep subwavelength operation. The pitch is 250 nm and the fill factor 50% hence, pushing the feature size to today's limits, yet on–axis propagation of a 1550 nm vacuum wavelength is already hitting a Bragg resonance. It is only the waveguide confinement that rescues a

metamaterial waveguide from Bragg resonance. It is also seen that when the barriers are air, the anisotropic behaviour is stronger and the extra-ordinary contour becomes more elliptical than when the barriers have a refractive index closer the refractive index of the silicon layers.

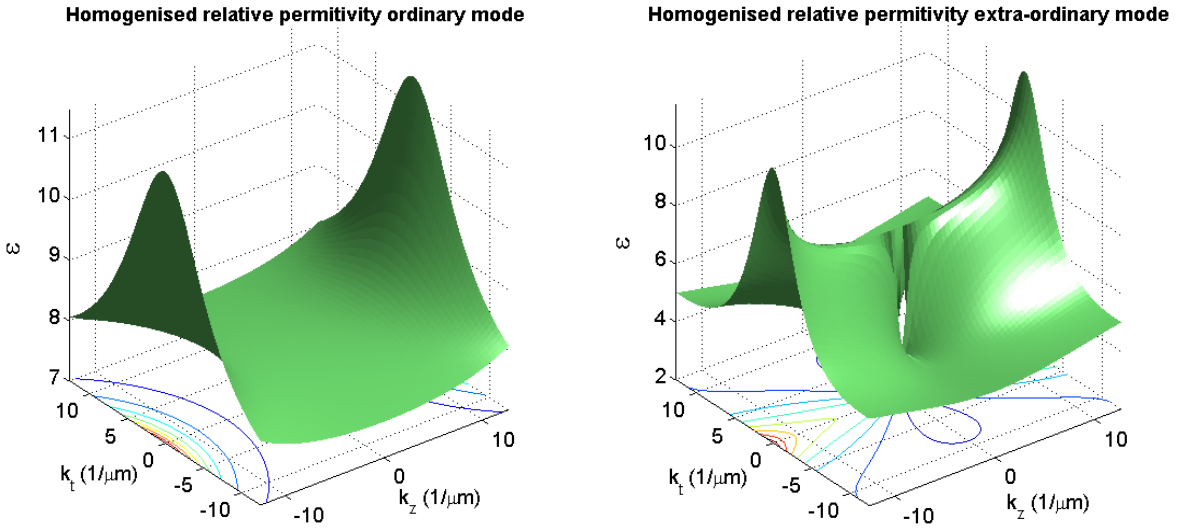

Figure 2.12 The effective permittivity of the ordinary mode (left) and extra-ordinary mode (right) in Kronig-Penney structure contains silicon stacks and silica barriers of fill-factor of 50% and pitch of 250 nm at the wavelengths of 1.55 μm.

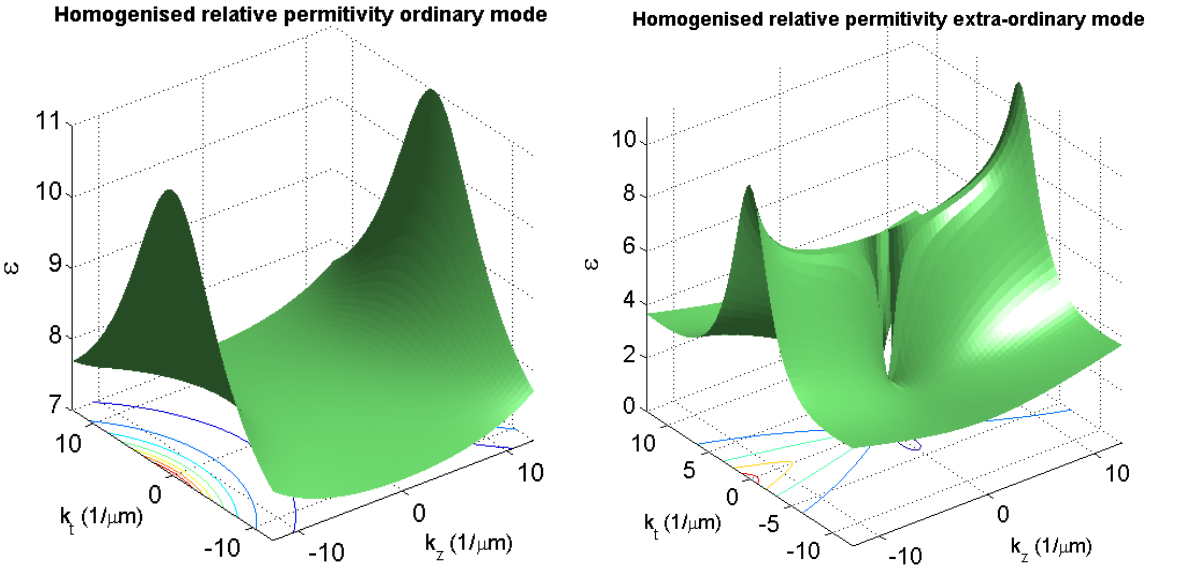

Figure 2.13 The effective permittivity of the ordinary mode (left) and extra-ordinary mode (right) in Kronig-Penney structure contains silicon stacks and air barriers of fill-factor of 50% and pitch of 250 nm at the wavelengths of 1.55 μm.

Using the method that leads to Eq. 2.17 the homogenised permittivity tensor can be found. Substitution of this tensor into Maxwell's equations reproduces the correct dispersion relation of the Floquet-Bloch modes. In the region where the equi-frequency contours are well approximated by an ellipse, the band structure manifold corresponds to a quadratic form

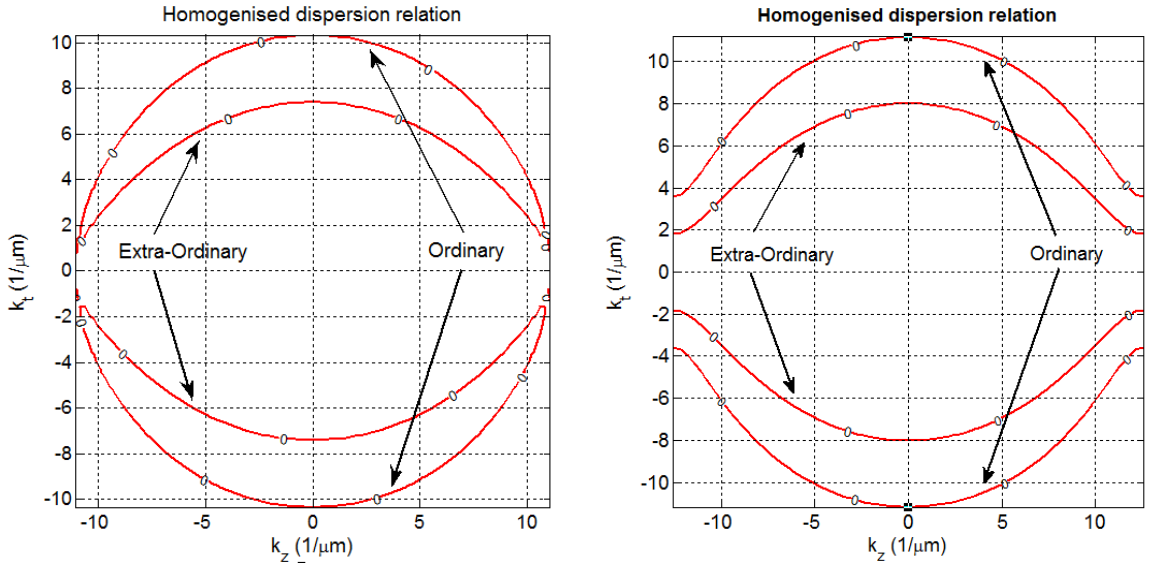

Figure 2.14 The homogenised dispersion relation of ordinary and extra-ordinary modes for silicon stacks and barriers of silica, (left) wavelength of 1.5 μm, (right) longer wavelength of 1.55 μm.

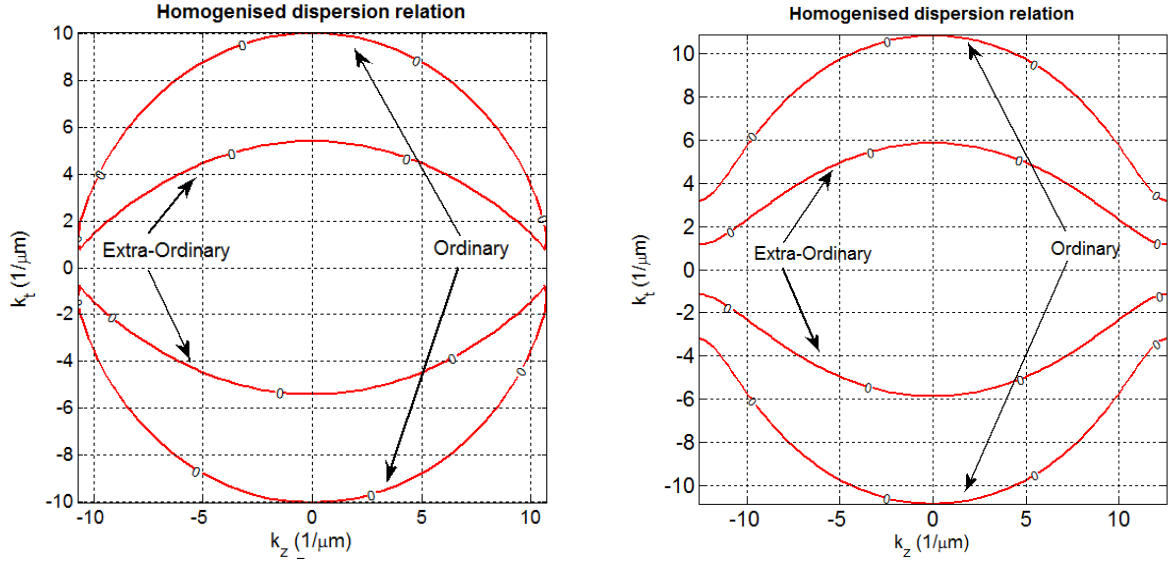

Figure 2.15 The homogenised dispersion relation of ordinary and extra-ordinary modes for multilayer silicon stack and barriers of air, (left) wavelength of 1.5 μm, (right) longer wavelength of 1.55 μm.

in the wave vector. The permittivity tensor may depend upon the frequency (i.e. temporal dispersion) but is independent of the wave vector and the response is local albeit anisotropic. In the case of the metamaterials considered in this thesis the anisotropy is uniaxial with c-axis either normal to the silicon layers in the 1D case or directed along the axis of uniformity in the 2D case. The permittivity tensor can then be defined by a diagonal matrix with elements equal to the ordinary index squared and one component of equal to the extra-ordinary index squared.

$$\bar{\bar{\varepsilon}} = \begin{bmatrix} n_0^2 & 0 & 0 \\ 0 & n_0^2 & 0 \\ 0 & 0 & n_e^2 \end{bmatrix} \tag{2.18}$$

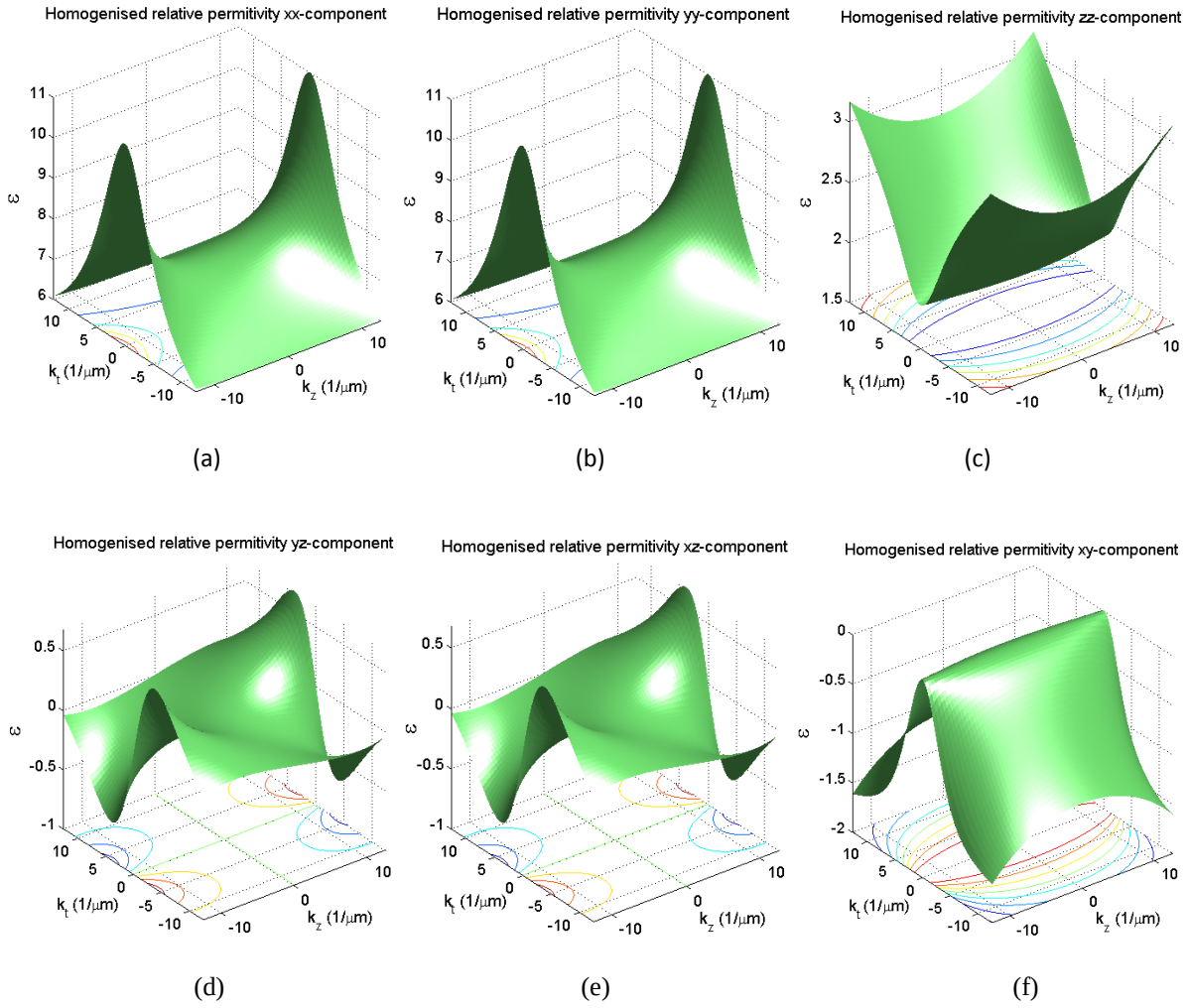

Figure 2.16 The homogenised permittivity tensor for the pitch of 250 nm of the multilayer silicon stack and barriers of air at the wavelength of 1.55 μm. Homogenised relative permittivity (a) xx-component, (b) yy-component, (c) zz-component, (d) yz-component, (e) xz-component, (f) xy-component.

In the non-local regime the permittivity tensor depends upon the wave vector $\boldsymbol{k}$ (i.e. spatial dispersion) and the response is non-local. It is not then possible to diagonalise the tensor for all $\boldsymbol{k}$ despite the uniaxial symmetry of the structure. The symmetry operation that leaves the structure and fields invariant must be applied to the argument $\boldsymbol{k}$ of the tensor as well as to the tensor itself. Formally, the wave vector breaks the symmetry of the tensor. Figure 2.16 shows the variation with $\boldsymbol{k}$ of the components of the homogenised relative permittivity tensor

2.6 Subwavelength Grating Slab Waveguides Homogenisation Methodology (2D Lattice)

In some metamaterial structures such as the lenses a two dimensional lattice may be used. A hexagonal lattice offers higher packing densities than other plane lattices. The 3D band solver for a 2D periodic medium gives an accurate value of the effective index of the structure but is computationally demanding. Hence, the calculation of the effective index of the mode with respect to the atom diameters can follow the method that was explained in section 2.4. In this thesis, the inclusions formed by cylindrical holes filled by air in a silicon layer is used. A 2D band solver on a 2D unit cell is used to calculate the homogeneous core index in a 3D waveguide structure shown in Figure 2.17.

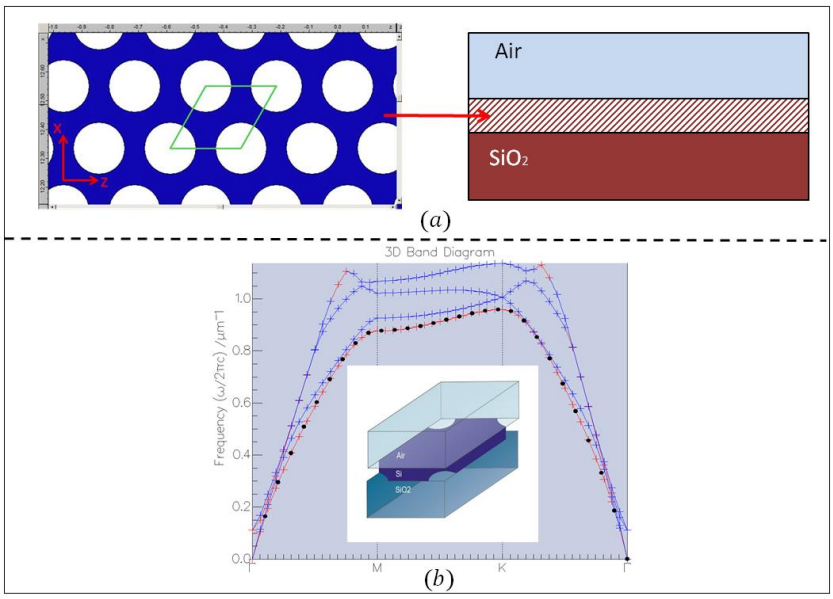

Figure 2.17 Subwavelength grating slab waveguide with 2D hexagonal lattice homogenisation methods; (a) top view of a 2D unit cell of air holes in a silicon layer and side view of an asymmetric slab waveguide with upper and lower cladding of air and silica respectively, (b) 3D unit cell and the corresponding band diagram.

For the structures for which a smooth change of effective index is needed, the hole diameters may change across the device on a regular lattice (in this thesis). The change in atom diameter is smooth enough that in a unit cell the 4 atoms may be assumed to have the same diameter. The hole diameters relative to the lattice constant determine the fill factor f, which for a hexagonal lattice is defined by:

$$f = \frac{\pi}{2\sqrt{3}} \frac{d^2}{p^2} \tag{2.19}$$

where d is the diameter of the atoms and p is the pitch (lattice constant). The validity of the homogenisation procedure described above was evaluated by numerical experiments using CrystalWave. Figure 2.18 shows a comparison between the effective indices obtained

directly from 3D band solver on a 3D unit cell, and the 2D band solver confinement of the 2D unit cell in the core of an asymmetric slab waveguide of silicon with the thickness of 300 nm with upper and lower cladding of air and silica. The plots are close to straight lines and consistent with the Kronig-Penney structure. The confinement corrected Ex-like mode fit to CrystalWave data is good but in Ey case the fit to CrystalWave diverges somewhat in the middle region. This may be due to the neglect of anisotropy in the boundary conditions.

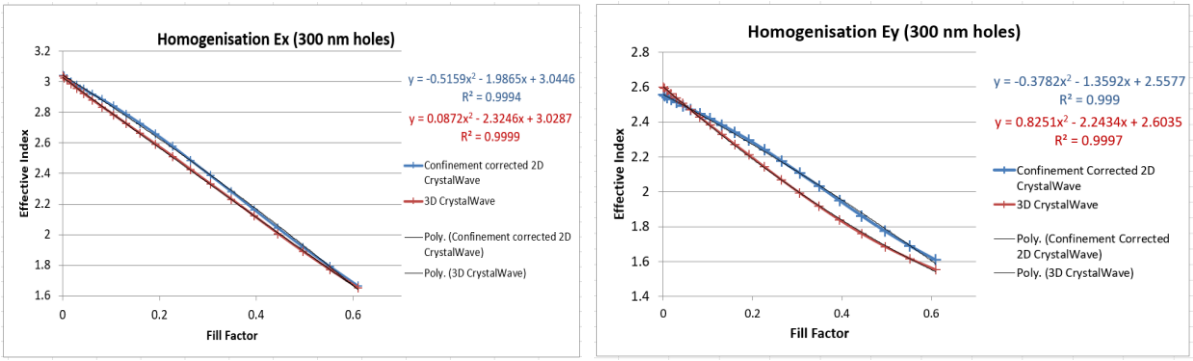

Figure 2.18 Effective refractive index of the mode vs. fill-factor for a hexagonal lattice constant of 250 nm with air hole inclusions in a silicon layer of 300 nm thickness at the core with the upper and lower claddings of air and silica respectively; (left) Ex modes, (right) Ey modes.

2.7 Summary

Nanostructuring of photonic integrated circuit components offers the designer the flexibility to refine the optical properties of a device. Homogenisation summaries the pertinent properties of the structure and omits the detail greatly reducing the computational demands of design tools. The substitution of subwavelength grating layers by continuous media with a refractive index given locally by the homogenised index of a perfectly periodic structure with local values of the structural parameters has been found to be a good design rule, despite the use of continuous media boundary conditions. Layer thickness and lattice period may be comparable. Spatial dispersion is significant for operation close to band edge. The real space averaging is local to a unit cell and the averaged field can be expected to adapt to an abrupt change within a boundary layer a few unit cells thick. The local effective permittivity and permeability parameters are estimated to be valid in a small neighbourhood of the origin Fourier space. Applying a band limit to Fourier space, such as limiting the spatial frequency by low pass filtering, is non-local in real space and the average field can be expected to adapt to an abrupt change along the direction of smoothing only within an extended boundary layer. In this chapter 1D lattice and 2D lattice metamaterial homogenisation was discussed and the dispersion confinement correction was introduced to avoid an artefact caused by the operating wavelength falling into the band gap of the metamaterial for on-axis propagation. In the next chapter, it is explained how to avoid the abrupt junctions by providing adiabatic structures that not only adapt waveguide dimensions but also adapt the homogenised index. The design and simulations of the test structures presented in the following chapters rests on the findings presented in this chapter.

Chapter 3. 1D Metamaterial and Anisotropy

3.1 Introduction

In chapter 2, homogenisation methods were discussed to address the challenges of the design of subwavelength planar light structures, which requires simulation with nanometer resolution, over a device that has dimensions measured in several wavelength units. In this chapter, 1D metamaterial structures and their emergent local anisotropic, and nonlocal temporal and spatial dispersive properties will be discussed. The engineering of the dispersion relation satisfied by the optical modes of a structure is addressed by appropriate design of subwavelength waveguides. This is applied to the reduction of the modal phase error in MMI towards perfect imaging. A novel polarisation beam splitter based on the Talbot effect in a longitudinal metamaterial structure and its connection to conventional waveguides using a matched adiabatic taper is proposed and demonstrated by simulation for the first time.

3.2 Contribution

The results provided in the first part this chapter are published in the journal of Applied Physics A. In this paper the emergent anisotropy and spatial dispersion properties of metamaterials and their engineering in metamaterial is discussed. The Talbot effect in a metamaterial is then analysed as a prelude to the reduction of the modal phase error towards perfect imaging and consequently enhancing the performance of devices that make use of the Talbot effect such as MMIs in applications requiring high port counts such as coherent optical processors and switches. The Talbot effect in a binary multilayer dielectric material is shown to act as a polarisation beam splitter. A novel polarisation beam splitter based on the Talbot effect in a longitudinal metamaterial slab waveguide structure is proposed and demonstrated by simulation for the first time. In the second part of the chapter, the connection of the longitudinal to a conventional access waveguide using a matched adiabatic taper is proposed and demonstrated by simulation again for the first time. I drafted the paper, performed the simulations and contributed the original idea for the polarisation beam splitter and matched adiabatic tapers. Mehedi Hasan contributed to the specification of the end-user requirements. Dr. Hall contributed to the theory, provided advice on the interpretation of the results and helped revise the manuscript.

3.3 Article

The following section is a reproduction of an article published in the Journal of Applied Physics A [39].

The Talbot Effect in a Metamaterial

H. Nikkhah, M. Hasan, T. J. Hall
University of Ottawa, Canada

Abstract- The effect of anisotropy and spatial dispersion of a metamaterial on the Talbot effect may be engineered in principle. This has profound implications for applications of the Talbot Effect such as the design of a multimode interference coupler (MMI). The paper describes how a metamaterial can suppress the modal phase error which otherwise limits the scaling of MMI port dimension. A binary multilayer dielectric material described by the Kronig-Penney model is shown to provide a close approximation to the required dispersion relation. Results of simulations of a multi-slotted waveguide MMI engineered to provide a polarising beam splitter function are given as an example of the method.

Keywords- Talbot Effect, Metamaterial, Subwavelength Waveguide Grating (SWG), Multimode Interference Coupler (MMI), Polarisation Beam Splitter (PBS), Kronig-Penney Model.

Photonic integrated circuit technology has advanced rapidly in recent years and is now seen as a critical enabler of applications in optical communications and quantum computing. These applications have raised the importance of further enhancement of functionality and integration density that has led to the emergence of sub-micron devices implemented on CMOS compatible integration platforms. Developments in lithography have eased the structuring of a material on a sub-wavelength scale and the application of metamaterials within photonic integrated circuits is now feasible within the realm of practical application. A multimode interference coupler (MMIs) is a key component used in the construction of complex photonic integrated circuits that, for example, involve meshes of Mach-Zehnder interferometers [1, 2]. Nanostructuring of photonic integrated circuit components brings an opportunity for novel device concepts and to enhance performance of existing devices [3, 4]. Major improvements in performance have been demonstrated by patterning MMI structures using subwavelength waveguide gratings (SWG) [5]. The operating principal of MMIs relies on the famous phenomenon known as the (fractional) Talbot effect which describes the longitudinally spatially periodic (multiple) self-imaging of a transversely spatially periodic field on propagation in free-space. The theory of the Talbot effect assumes Fresnel diffraction; equivalently, a spectrum of plane wave modes concentrated on-axis, and the phase relation between the self-images predicted evinces an intimate relationship with number theory [6]. The free-space Talbot effect may be mapped to a description of the self-imaging properties of a planar multimode waveguide. The theory of the waveguide Talbot effect follows that of the free-space Talbot effect once account is taken of the (near) zero of the field introduced by the waveguide sidewalls. This somewhat complicates the phase relations [7]. The free-space Talbot effect extends naturally to a homogenous medium and, consequently, to metamaterials.

There have been significant improvements in MMI design to enhance the performance (uniformity, efficiency, and bandwidth) and to reduce foot-print. However, the performance of a MMI on a high-index contrast platform decreases significantly as the number of ports is increased due to a departure of the phase accumulated on propagation by the modes from the value predicted by the paraxial approximation. This can be ameliorated by the use of a low index contrast platform [8] but this expedient conflicts with the requirement for high quality fractional self-imaging that the modal expansion is close to a Fourier series. It is modal phase errors caused by the failure of the paraxial approximation that impair performance, whether introduced by coupling of the access-waveguides or by failure of the paraxial approximation in a multimode section.

Additional degrees of freedom are needed to tune the individual phases of the intermediate modes, which might be introduced by appropriate patterning of the geometrical or optical properties of the multimode section. The perturbation of the lateral refractive index profile in the multimode section to reduce the modal phase errors has been considered theoretically [9]. Shallow etching of the multimode region can also reduce the effective index contrast [10], but these solutions have the demerit of requiring multiple etch steps in the fabrication process. MMIs formed using a SWG structure offer a solution requiring only a single etch step. In this way, the lateral refractive index contrast may be reduced by using SWG in the lateral cladding regions of the multimode section while the high index contrast on the access waveguides remains to be able to place them closely to reduce the size of MMIs when the number of ports increases [11]. Moreover, the modal birefringence of the waveguide

can be controlled by depositing low and high index layers with the subwavelength pitch on the top of the waveguide [12]. MMIs that make use of the anisotropy of SWG structure to achieve ultra-compact footprints have been reported recently [13] and an MMI with ultra-broad bandwidth of 450 nm and phase deviation below 3 degrees has been achieved [5] by engineering the dispersion properties of the multimode region using SWG to mitigate the wavelength dependence of the Talbot distance.

The paper reports findings on how a metamaterial can suppress the modal phase error which otherwise limits the scaling of MMI port dimension, and how a binary multilayer dielectric material described by the Kronig-Penney model may provide a close approximation to the required dispersion relation. The findings may enable the realisation of photonic integrated circuits components of unprecedented performance. For example, a compact broadband MMI with large port counts would constitute a breakthrough in integrated passive coupler / splitter components enabling, *inter alia*, single component discrete space passive DFT functions and large cross-overs with accurate port phase relations.

I. Spatial dispersion and anisotropy of dielectric metamaterials

Metamaterials made from isotropic component materials can show very strong anisotropy leading to new opportunities for compact integrated components for polarisation management and new all-dielectric methods of strong confinement [14] without metals which introduce loss. Metamaterials offer also a new degree of freedom to manipulate the dispersion relation. For example, many devices depend upon the validity of the paraxial approximation. It is conceivable that the spatial dispersion of a metamaterial can be engineered so that the paraxial approximation is accurate throughout the metaxial regime [15] thereby allowing the scaling of devices such as MMI to higher port counts.

The properties of metamaterial structures are analysed by a homogenisation procedure that extracts properties from the microscopic detail pertinent to the macroscopic scale in a way analogous to the treatment of atomic matter as a continuous media [16]. The homogenised properties are emergent from the geometry as much as the constituents of the microstructure and consequently may be engineered. The established procedure requires that the detailed structure of the composite is small compared to the wavelength of the light. Theories of homogenisation applicable to the larger scale subwavelength regime close to Bragg resonance are controversial [17] particularly in respect of boundary conditions at the interfaces between homogenised media. These problems are avoided in this work by limiting the homogenisation process to a direction transverse to an interface and, when that is not possible, through the use of adiabatic transition regions that effectively eliminate the interface.

Homogenised bulk SWG behave as strongly anisotropic materials with a c-axis normal to the layers of a 1D multi-layer (Kronig-Penney structure) or along the axis of uniformity for a 2D photonic crystal in 3D. Anisotropy can help reduce the Talbot length but temporal and spatial dispersion is necessary to control the modal phase error and the wavelength dependence of the Talbot length. A metamaterial can result in a Talbot length substantially independent of vacuum wavelength – thereby permitting broadband operation [13].

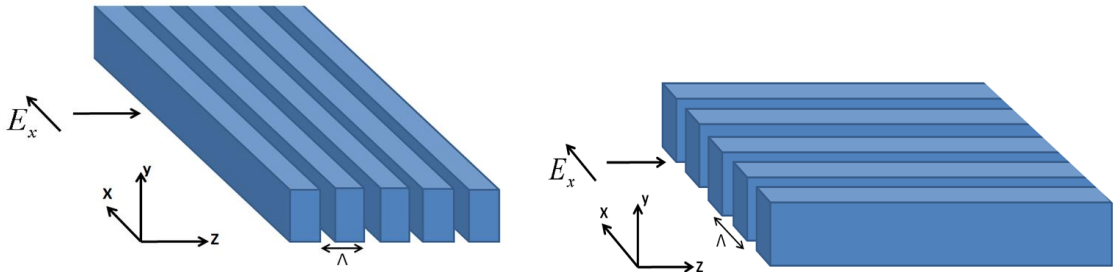

(a) (b)

Fig. 1 (a) Transverse strcuture when the propagation of light is along z axis and the light propagates perpendicular to the slots. (b) Longitudinal structure when the propagation of light is along z axis and the light propagates parallel to the slots.

A MMI with a segmented structure shown in Figure 1(a), where the Ex-like polarized beam propagates in the direction perpendicular to the slots has been reported that achieves an operating bandwidth of 500 nm [5]. Iwanow et al. [18] reported observing Talbot effect in a multi-waveguide array (equivalently a slotted

multimode waveguide) when the Ex polarized beam propagates parallel to the multi-waveguide axes as shown in Figure 1(b). They observed the phenomenon in a structure where the period of the structure was large enough and the slots wide enough for the fields to be accurately described by a tight-bonding nearest-neighbour coupled waveguide mode model rather than by an effective field within a homogenised structure. Subsequent work by Garanovich et al. [19] applied a similar theoretical description to diffraction management using an array of curved waveguides. The segmented waveguide and parallel multi-waveguide array structures are referred to in this paper as transverse and longitudinal structures with respect to the direction of propagation along the z coordinate as shown in Figure 1.

II. The Free Space Talbot effect and Anisotropy

An optical field that is periodic in the transverse plane revives or self-images periodically along the optical axis [20]. This is the phenomenon that is known as the Talbot effect [21, 22]. The theory describes the evolution of the near field (Fresnel) diffraction pattern from a periodic grating in the paraxial approximation that predicts periodic self-images in planes beyond the grating provided the wavelength is far smaller than the transverse period. The self-images are found at rational fractional multiples of the fundamental Talbot distance [20]:

$$Z_T = \frac{\Lambda^2}{\lambda} \tag{1}$$

Where Λ is the period of the grating and λ is the vacuum wavelength of the coherent light source. The detailed theory of the Talbot effect yields the relative phases of the self-images in terms of the Gauss sum of number theory [6]. The theory of the waveguide Talbot effect follows that of the free-space Talbot effect once account is taken of the (near) zero of the field introduced by the waveguide sidewalls. This somewhat complicates the form of the phase relations.

The theory of the Talbot effect may be straightforwardly generalised to a homogenised medium provided adequate account is taken of anisotropy and dispersion. It follows that the Talbot effect occurs in the long-wavelength operating regime of a metamaterial. The metamaterial is specialised here to an infinite regular periodic multilayer two-component dielectric stack of alternating higher refractive index material and lower index materials, shown figure 2. This structure has the advantage of a theoretical description in terms of the Kronig-Penney model [23] which may be analysed using a transfer matrix approach [24].

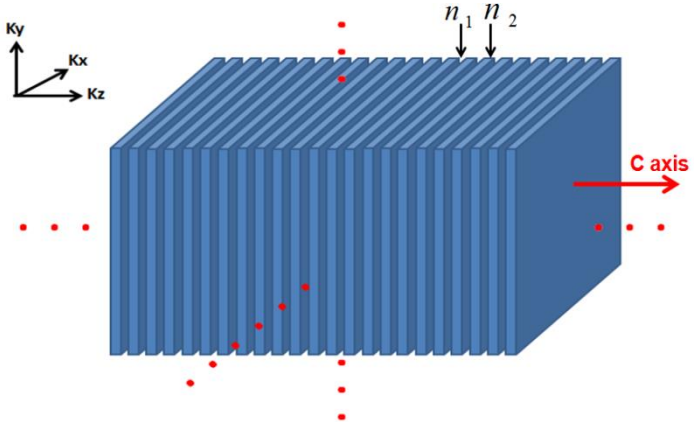

Fig. 2 Kronig-Penney model metamaterial consisting of an infinitely extended periodic binary dielectric multilayer stacks.

The Bloch modes of the Kronig-Penney structure have the form:

$$\Psi(x,z) = \exp(ik_x x)\exp(ik_z z)u(z) \tag{2}$$

where k_z, k_x are the longitudinal and transverse components of the Bloch wavevector, u is periodic with period $\Lambda = d_1 + d_2$, and ρ is a parameter that depends upon the polarisation state:

$$\rho = \begin{Bmatrix} \frac{n_1^2}{n_2^2}\frac{\beta_2}{\beta_1} & TM\ (H_z = 0) \\ \frac{\beta_2}{\beta_1} & TE\ (E_z = 0) \end{Bmatrix} \tag{3}$$

The parameters of the Bloch mode satisfy the dispersion relation which describes the band-structure.

$$\cos\left(k_z(d_1+d_2)\right) = \cos(k_1 d_1)\cos(k_2 d_2) - \frac{1}{2}(\rho^{-1}+\rho)\sin(k_1 d_1)\sin(k_2 d_2) \quad (4)$$

$$k_j = \sqrt{n_j^2 k_0^2(\omega^2/c^2) - \kappa^2} \quad ; \quad k_0 = \omega/c$$

Where n_1 and n_2 are the refractive index and β_1 and β_2 are the associated wavenumber of the well and barrier materials respectively, ω is the frequency and c is the velocity of light. An expansion to second order of the Kronig-Penney dispersion relation valid at operating effective wavelengths large compared to the period predicts circular equifrequency contours function for TE ($E_z = 0$) polarization:

$$\frac{k_z^2}{n_o^2} + \frac{k_x^2}{n_o^2} = k_0^2 \quad ; \quad n_o^2 = f n_1^2 + (1-f) n_2^2 \quad (5)$$

and elliptical equi-frequency contours for TM ($H_z = 0$) polarisation:

$$\frac{k_z^2}{n_o^2} + \frac{k_x^2}{n_e^2} = k_0^2 \quad ; \quad \frac{1}{n_e^2} = f\frac{1}{n_1^2} + (1-f)\frac{1}{n_2^2} \quad (6)$$

where:

$$f = \frac{d_1}{d_1+d_2} \quad (7)$$

is the fill factor,

The homogenised Kronig-Penney structure thereby behaves as a negative $n_o^2 > n_e^2$ uniaxial anisotropic medium with optic axis normal to the plane of the layers within the stack and with the TE and TM Bloch modes (avergeraged over one period of the structure) acting as the ordinary and extra-ordinary plane wave solutions.

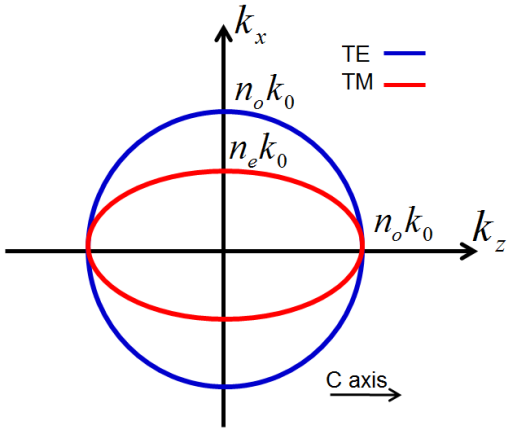

Fig. 3 The equifrequency contour near the origin of the lowest band when the β's axis is aligned with the c-axis, and the ordinary effective index is higher than the extraordinary effective index.

Figure 3 shows the shape of the equi-frequency contours near the origin of the lowest band of the band-diagram. At higher frequencies there is a deviation from a linear scaling with frequency of the equi-frequency contours; the principal values of the effective refractive indices n_o, n_e depend on frequency and the homogenised material is temporally dispersive. At frequencies approaching the edge of the first band, the contours deviate in shape from an ellipse and ultimately become open; the contours deviate from a quadratic dependence on the wave vector and the homogenised material has a nonlocal spatially dispersive response

The deviation of the band structure from the spherical cone of free-space manifested by anisotropy, temporal and spatial dispersion provides an opportunity for enhancement of the performance devices such as MMI implemented using engineered metamaterials.

III. Phase Error Analysis

The perfect self-imaging relies on the accuracy of the paraxial approximation which is equivalent to approximating the equi-frequency contour locally by a parabola. Departures from the parabola are manifest as a

deviation from the ideal of the longitudinal component of the wave vector of the mode. This deviation results in the accumulation of a phase error on propagation. Since any device based on the Talbot effect will have a length determined by the Talbot length, the modal phase error is evaluated here after propagation over one Talbot length. Two orientations of the Kronig-Penney structure with respect to the device, referred to here as 'transverse' and 'longitudinal', are considered. The nominal direction of propagation is taken to be the $z-$axis. The transverse structure has the normal to the dielectric layers (the $c-$axis of the uniaxial material) aligned parallel to the $z-$axis. The longitudinal structure has the normal to the dielectric layers aligned parallel to the $x-$axis. For plane wave propagation nominally along the $z-$axis in the (z,x) plane ($k_x^2 < k_z^2 \quad ; \quad k_y^2 \approx 0$) an E_x-like polarised mode in a transverse structure and an E_x-like polarised mode in a longitudinal structure then correspond to the extra-ordinary polarisation mode (i.e. TM) of the Kronig-Penney structure.

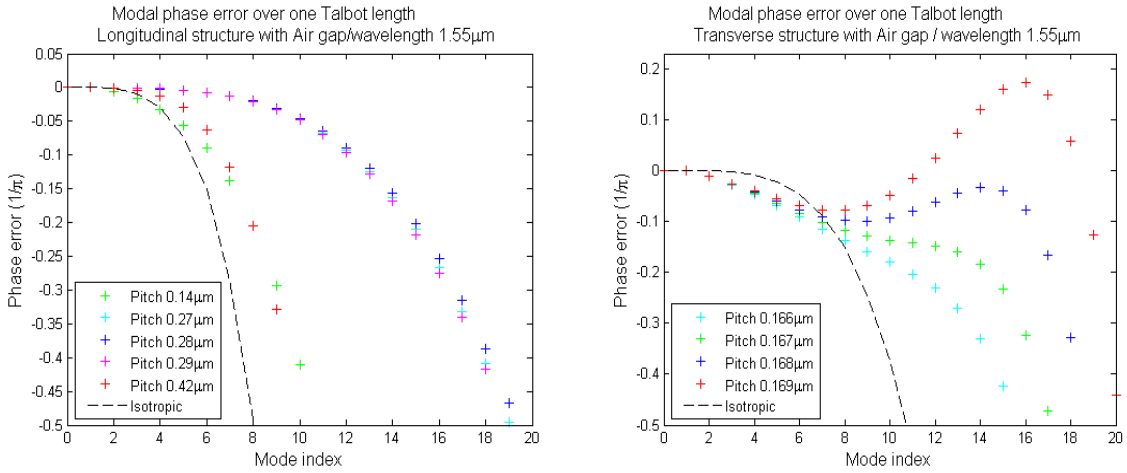

Fig. 4 Modal phase error of metamaterial structure with respect to the pitch change with air-gap at the wavelength of 1.55μm over one Talbot distance, (left) longitudinal structure, and (right) transverse structure.

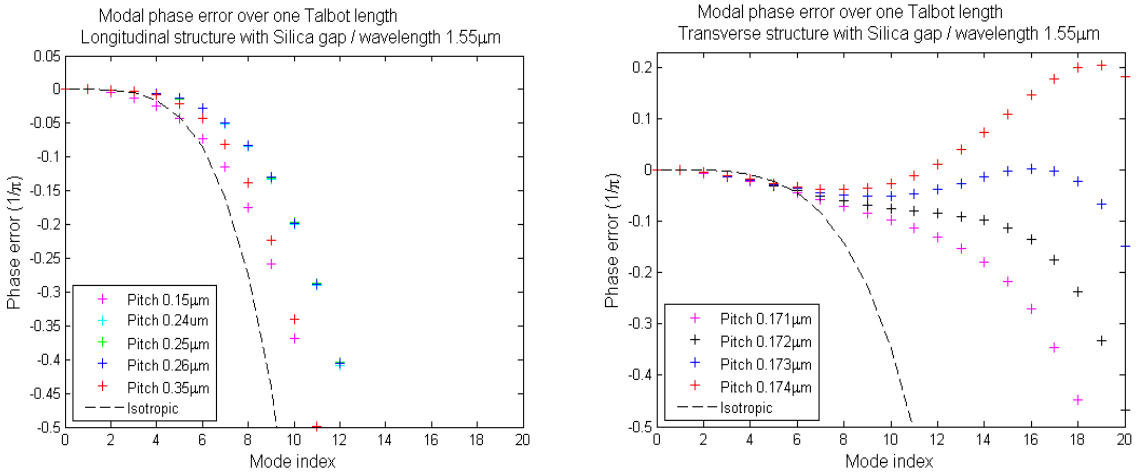

Fig. 5 Modal phase error of metamaterial structure with respect to the pitch change with silica-gap at the wavelength of 1.55μm over one Talbot distance, (left) longitudinal structure, and (right) transverse structure.

In the first case considered, the structure is built of silicon dielectric stacks immersed in air. Figure 4 shows the modal phase error for the transverse and longitudinal structures over one Talbot distance for different mode index m where $k_x = m(2\pi/\Lambda)$, and different pitches of the structure. The best pitch for small phase error of the lowest order modes at an operating vacuum wavelength $\lambda = 1.55$ μm is found to be 0.167 μm and 0.28 μm for transverse and longitudinal structures respectively.

The plots indicate an extreme sensitivity of the transverse structure to small deviations (~1 nm) in pitch around the best value. The longitudinal structure shows greater stability and provides an improved phase error over a

wide range of pitch. The larger feature size and robustness to dimensional errors thereby favours the longitudinal structure over the transverse structure as a practical route to modal phase error reduction. Interestingly for the second case where the barriers are silica rather than air, the transverse structure shows less modal phase error at the operating wavelength but still the longitudinal structure shows greater stability with respect to perturbations in dimensions (Figure 5).

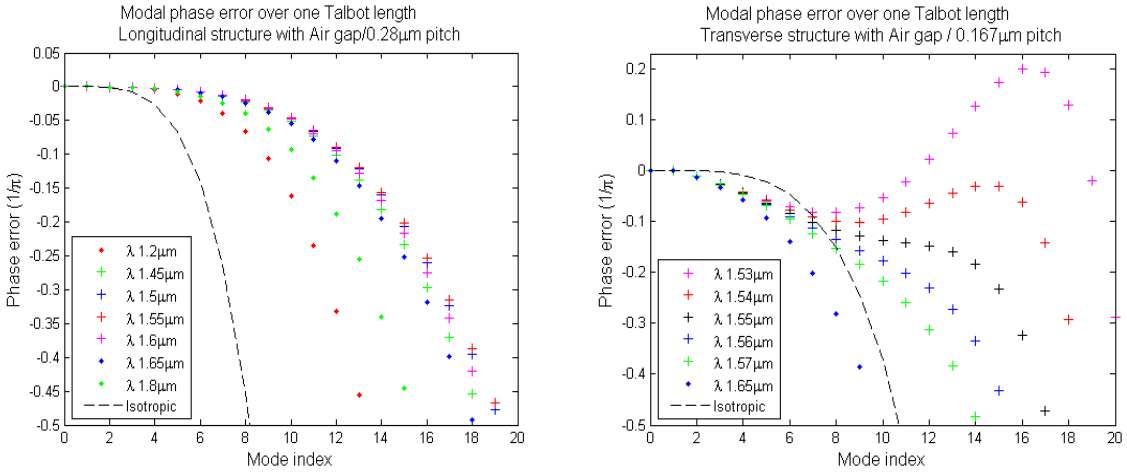

Fig. 6 Modal phase error of metamaterial structure with respect to wavelength change with air-gap at a constant pitch over one Talbot distance, (left) longitudinal structure with the pitch of 0.28 μm, and (right) transverse structure with the pitch of 0.167 μm.

Figure 6 illustrates the dependence on operating vacuum wavelength of the modal phase error for an air-barrier for a pitch selected for best behaviour at 1.55 μm. The modal phase error is smaller and much more stable and for the longitudinal structure over a wider range of operating wavelengths than the transverse structure.

Figure 7 shows the plots of modal phase error for the pitch of 0.26 μm and 0.172 μm selected for the best modal phase error performance at the operating wavelength for the longitudinal and transverse structures with silica barriers respectively. The transverse structure shows an enhancement of the modal phase error performance over a 12 nm range of wavelength variation. Although the modal phase error at the operating wavelength offered by the longitudinal structure is inferior to the transverse structure, nevertheless, it offers improved modal phase error with much greater stability to dimensional errors over a much wider 600 nm range of wavelength variation.

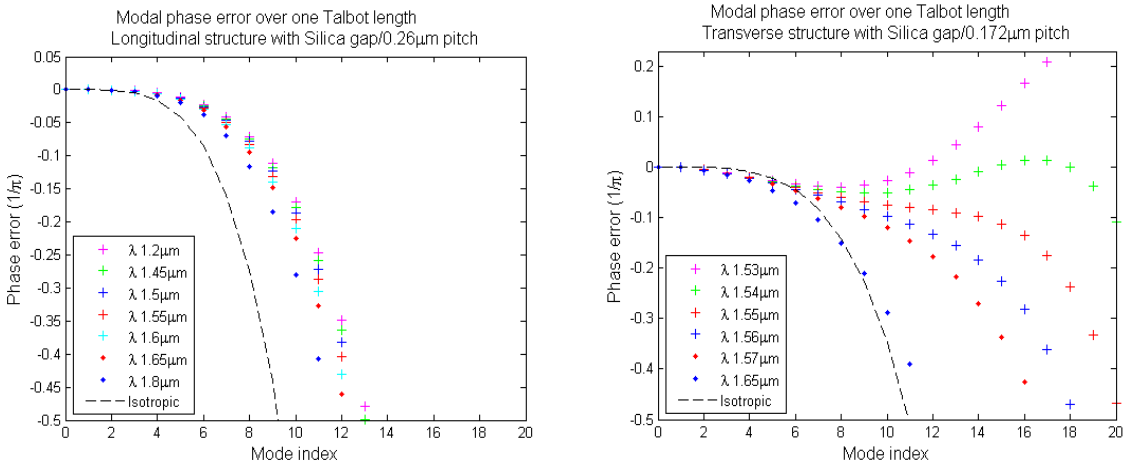

Fig. 7 Modal phase error of metamaterial structure with respect to wavelength change with silica-gap at a constant pitch over one Talbot distance, (left) longitudinal structure with the pitch of 0.26 μm, and (right) transverse structure with the pitch of 0.172 μm.

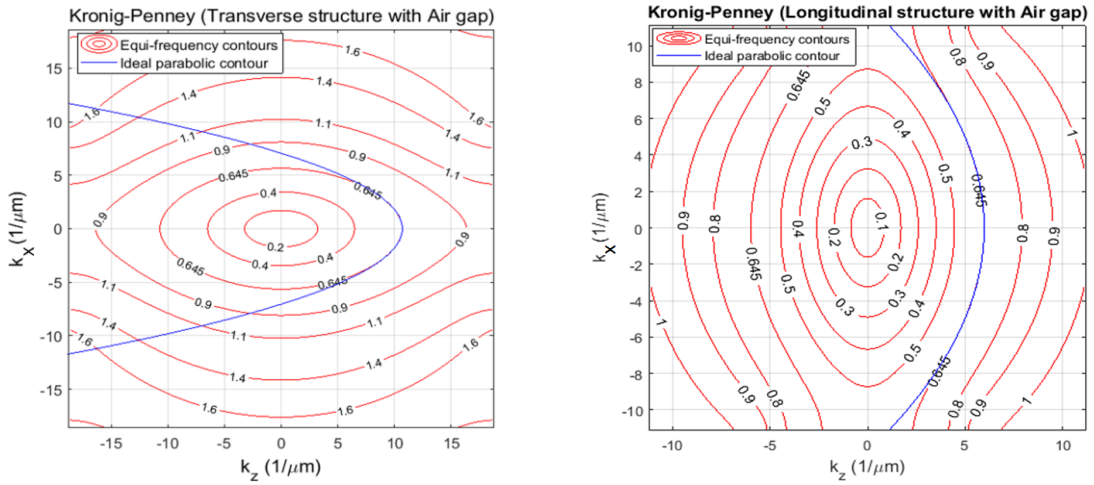

Fig. 8 Equifrequency contours and target parabolic contour for an air-barrier transverse structure for a pitch of 0.167 µm (left) and longitudinal structure for a pitch of 0.28 µm (right)

Figure 8 shows a comparison of the equi-frequency contours and target parabolic contour of transverse and longitudinal structures with an air-barrier for a pitch 0.167 µm and 0.28 µm respectively selected for best behaviour at 1.55 µm. The Figures show the good fit of a parabola with the equi-frequency contour at 1.55 µm.

Figure 9 shows a comparison of the equi-frequency contours and target parabolic contour of transverse and longitudinal structures with a silica-barrier for a pitch of 0.172 µm and 0.26 µm respectively selected for best behaviour at 1.55 µm.

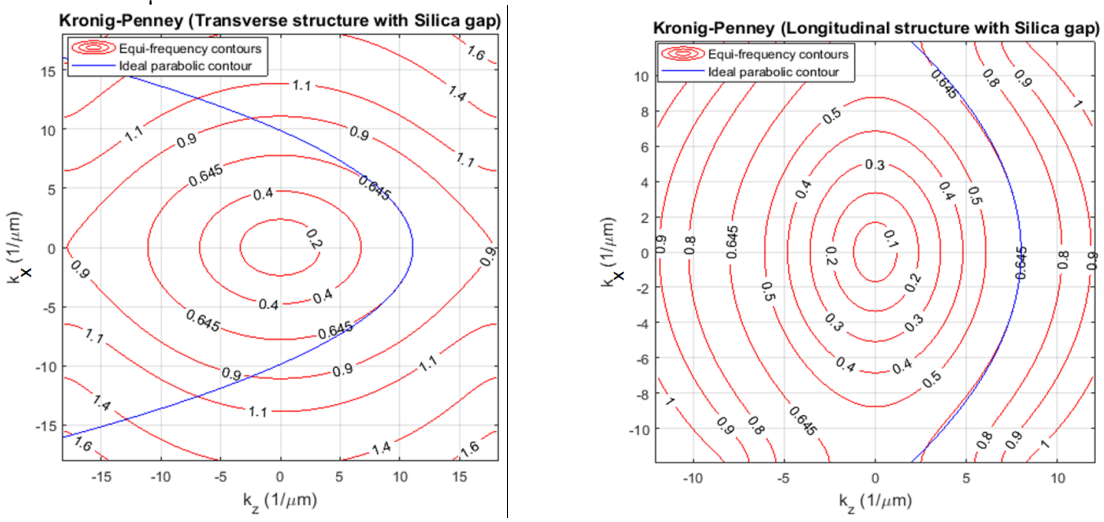

Fig. 9 Equifrequency contours and target parabolic contour for a silica-barrier transverse structure for a pitch of 0.172 µm (left) and longitudinal structure for a pitch selected of 0.26 µm (right)

IV. Simulations and Verifications

The high birefringence of metamaterials suggests their application as wave plates for the manipulation of the state-of-polarisation. A plane-wave propagating along the z-axis of the longitudinal Kronig-Penney structure experiences giant birefringence. In contrast, the ordinary and extra-ordinary polarised modes are degenerate for propagation along the z-axis in the transverse Kronig-Penney structure. In waveguide formats the details of the dispersion relation satisfied by a mode depends on both the orientation and detail of the microstructure of the metamaterial and the waveguide confinement provided by the overall device. Any curvature in the equi-frequency contours will however result in a Talbot length that depends on the state-of-polarisation. An integrated polarisation beam-splitter is proposed here, for the first time as far as the authors are aware, that uses this polarisation dependence of the Talbot length.

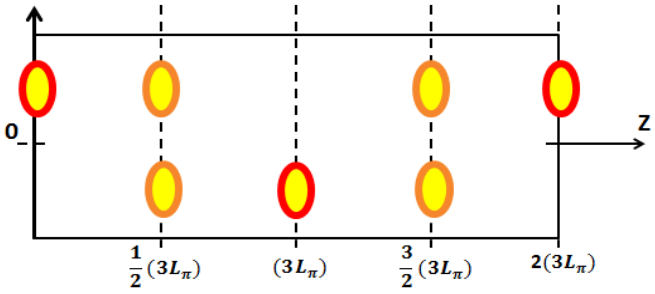

Fig. 10 The Talbot effect in a waveguide and the reproduction of the in-phase and opposite-phase self-images.

The self-image in a waveguide structure is defined by a beat length which is obtained from the propagation constants of the first two lowest order modes:

$$L_\pi = \frac{\pi}{\beta_1 - \beta_2} \equiv \frac{1}{3} z_T \tag{8}$$

The Talbot effect in a waveguide and the reproduction of the primary (in-phase) and secondary (anti-phase) self-images is illustrated in Figure 10. To achieve a polarisation splitter based on the Talbot effect the ratio of beat lengths of the E_x and E_y modes is ideally two so that the device length may be chosen to form a primary image at twice the Talbot distance of one polarsation and a secondary image for the orthogonal polarisation. For a longitudinal structure consisting of an array of 18 parallel waveguide, this ratio can be obtained at a pitch of 0.455 µm for 0.355 µm wide and 0.35 µm thick silicon waveguides seperated by an air-gap of 0.1µm with air over-cladding, which meets the minimum feature size of the fabrication process. Figure 11 shows the schematic of the slotted multimode waveguide regionof the polarisation beam splitter that illustrates the two input ports and the two output ports by the yellow triangles.

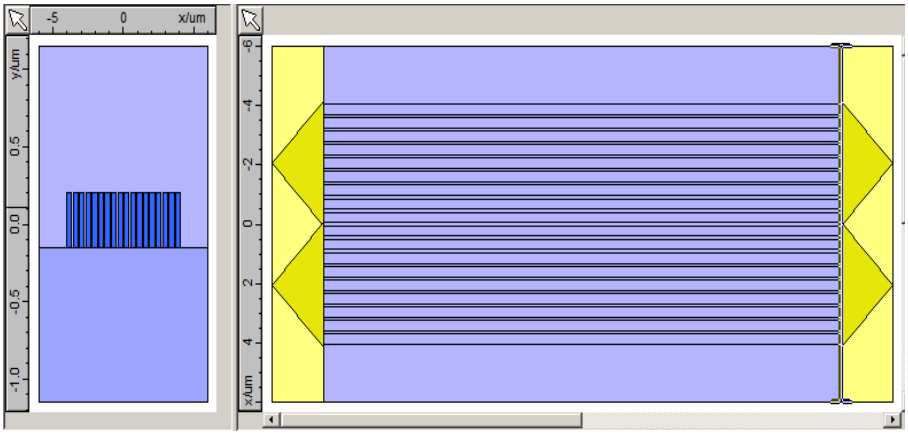

Fig. 11 The FimmProp schematic of the slotted multimode waveguide region of the polarisaton beam splitter that illustrates the two input ports and the two output ports by the yellow triangles. The left panel shows the cross section of the multi-slotted waveguide.

Figures 12 and 13 show visualisations of wave propagation along the longitudinal structure for the Ex and Ey polarization respectively over the optimised device length (excluding access tapers) of 964.844 µm. The simulation was done using the FimmProp tool of the PhotonDesign software suite. Figure 12 shows the imaging of an Ex mode launched by the upper input port onto the lower output port. Conversely, figure 13 shows the imaging of an Ey mode launched by the upper input port onto the upper output port. A transmission of 98.43% and 99.76% and an extinction ratio of -40.71 dB and -45.49 dB were achieved for the Ex and Ey modes respectively at the optimum length of 964.844 µm.

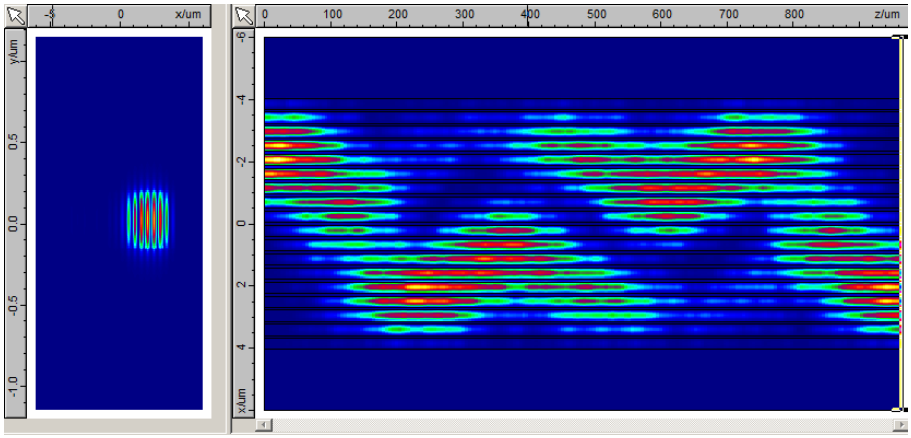

Fig. 12 The simulation of propagation (right panel) of Ex mode over the device length of 964.844 μm. The left panel shows the cross section of mode at the output port.

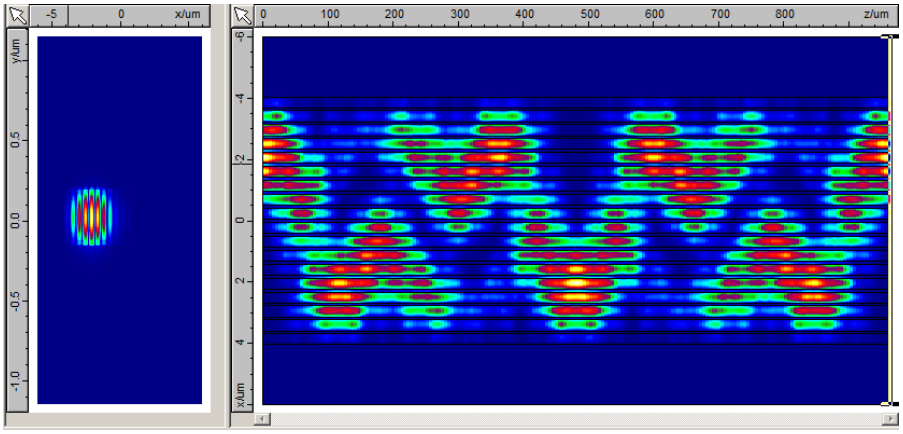

Fig. 13 The simulation of propagation (right panel) of the Ey mode over the device length of 964.844 μm. The left panel shows the cross section of mode at the output port.

V. Conclusions

The Talbot effect in longitudinal and transverse multi-layer metamaterial structures has been discussed in this paper. In the deep subwavelength regime, the metamaterial can be described by its local anisotropic response but at optical frequencies this requires feature sizes that are beyond current volume fabrication processes. Structures meeting current fabrication constraints require account of spatial and temporal dispersion. Modifying the dispersion relation by subwavelength engineering can improve the accuracy of the paraxial approximation and consequently reduce the error of modal phase from perfect imaging in MMIs. A silicon integrated polarisation beam splitter based on the Talbot effect in a longitudinal metamaterial structure has been proposed in this paper with promising results of simulation. The results obtained suggest that a combination of transverse and longitudinal subwavelength patterning may offer a route to a compact, broadband, low modal phase error MMI.

References

1. D. A. B. Miller, *"Silicon photonics: Meshing optics with applications."* Nature Photonics 11 (2017): 403-404.
2. T. J. Hall, M. Hasan, *"Universal discrete Fourier optics RF photonic integrated circuit architecture."* Optics Express 24.7 (2016): 7600-7610.
3. H. Nikkhah, T. J. Hall, *"Subwavelength grating waveguides for integrated photonics."* Applied Physics A, **122**:368 (2016): 1-6.

4. H. Nikkhah, T. J. Hall, *"Metamaterial Lüneburg lens for Fourier optics on-a-chip*." Proc. SPIE OPTO, Integrated Optics: Devices, Materials, and Technologies, Photonics West, San Francisco, United States (2014): 89880J-89880J.
5. A. Maese-Novo, R. Halir, S. Romero-García, D. Pérez-Galacho, et al., *"Wavelength independent multimode interference coupler."* Optics Express 21.6 (2013): 7033-7040.
6. L. Auslander, R. Tolimieri, *"Is computing with the finite Fourier transform pure or applied mathematics?"* Bulletin of the American Mathematical Society 1.6 (1979): 847-897.
7. H. Nikkhah, Q. Zheng, I. Hassan, S. Abdul-Majid, T. J. Hall, "*The Free Space and Waveguide Talbot Effect: Phase Relations and Planar Light Circuit Applications*." Photonics North, Montreal, Canada, (2012): 841217-841217.
8. J. Z. Huang, R. Scarmozzino, R. M. Osgood, *"A new design approach to large input/output number multimode interference couplers and its application to low-crosstalk WDM routers."* IEEE Photonics Technology Letters 10.9 (1998): 1292-1294.
9. I. Molina-Fernandez, A. Ortega-Moñux, J. G. Wangüemert-Pérez, *"Improving multimode interference couplers performance through index profile engineering."* Journal of Lightwave Technology 27.10 (2009): 1307-1314.
10. R. Halir, G. Roelkens, A. Ortega-Moñux, J. G. Wangüemert-Pérez, *"High-performance 90 hybrid based on a silicon-on-insulator multimode interference coupler."* Optics Letters 36.2 (2011): 178-180.
11. A. Ortega-Monux, L. Zavargo-Peche, A. Maese-Novo, et al., *"High-performance multimode interference coupler in silicon waveguides with subwavelength structures."* IEEE Photonics Technology Letters 23.19 (2011): 1406-1408.
12. D. Pérez-Galacho, R. Halir, A. Ortega-Moñux, C. Alonso-Ramos, et al., *"Integrated polarization beam splitter with relaxed fabrication tolerances."* Optics Express 21.12 (2013): 14146-14151.
13. R. Halir, P. Cheben, J. M. Luque-González, J. D. Sarmiento-Merenguel, et al., *"Ultra-broadband nanophotonic beamsplitter using an anisotropic sub-wavelength metamaterial."* Laser & Photonics Reviews 10.6 (2016): 1039-1046.
14. S. Jahani, Z. Jacob, *"Transparent subdiffraction optics: nanoscale light confinement without metal."* Optica 1.2 (2014): 96-100.
15. K. B. Wolf, *"Fourier transform in metaxial geometric optics."* JOSA A 8.9 (1991): 1399-1403.
16. L. D. Landau, E. M. Lifshitz, *"Course of Theoretical Physics."* Electrodynamics of Continuous Media. Oxford, 1960.
17. V. A. Markel, I. Tsukerman, *"Current-driven homogenization and effective medium parameters for finite samples."* Physical Review B 88.12 (2013): 125131.
18. R. Iwanow, D. A. May-Arrioja, D. N. Christodoulides, G. I. Stegeman, Y. Min, W. Sohler, *"Discrete Talbot effect in waveguide arrays."* Physical Review Letters 95.5 (2005): 053902.
19. I. L. Garanovich, A. A. Sukhorukov, Y. S. Kivshar, *"Broadband diffraction management and self-collimation of white light in photonic lattices."* Physical Review E 74.6 (2006): 066609.
20. K. Patorski, *"I the self-imaging phenomenon and its applications."* Progress in optics 27 (1989): 1-108.
21. H. F. Talbot, *"LXXVI. Facts relating to optical science. No. IV."* The London and Edinburgh Philosophical Magazine and Journal of Science 9.56 (1836): 401-407.
22. L. Rayleigh, *"XXV. On copying diffraction-gratings, and on some phenomena connected therewith."* The London, Edinburgh, and Dublin Philosophical Magazine and Journal of Science 11.67 (1881): 196-205.
23. R. D. L. Kronig, W. G. Penney, *"Quantum mechanics of electrons in crystal lattice."* Proc. R. Soc. London, Ser. A (1930): 130, 499-513
24. P. Yeh, A. Yariv, C. S. Hong, *"Electromagnetic propagation in periodic stratified media. I. General theory."* JOSA 67.4 (1977): 423-438.

3.4 A Longitudinally Slotted Taper for Smooth Transition

For a smooth transition from a standard access waveguide to the multimode region of a longitudinally slotted polarisation splitter MMI, an adiabatic taper is suggested at the ports of MMI which matches both the effective index and geometry of the ports and the slotted multimode region. The taper consists of a number of stages. The first stage contains a single access waveguide. At each subsequent stage a pair of waveguides is placed symmetrically about the continuation of the waveguides of the previous stage. An exponential function of weight -4 is used to curve the walls of the waveguides to introduce coupling adiabatically between the existing and additional waveguides to ensure an effective index match at the interface between sections and to assist mode expansion. Special care was taken over the positioning of the added waveguides to avoid a sudden change in effective index and hence reflection at the section interfaces.

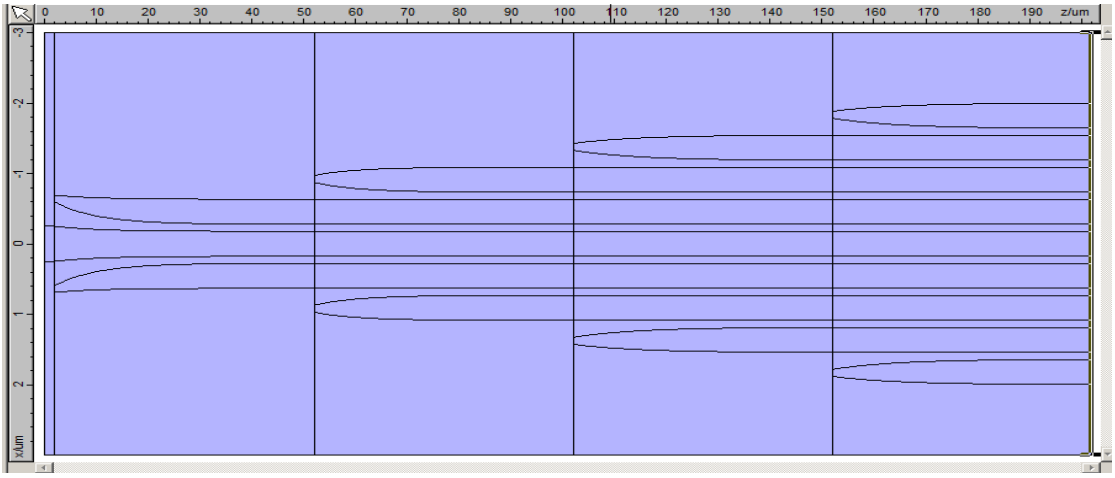

(a)

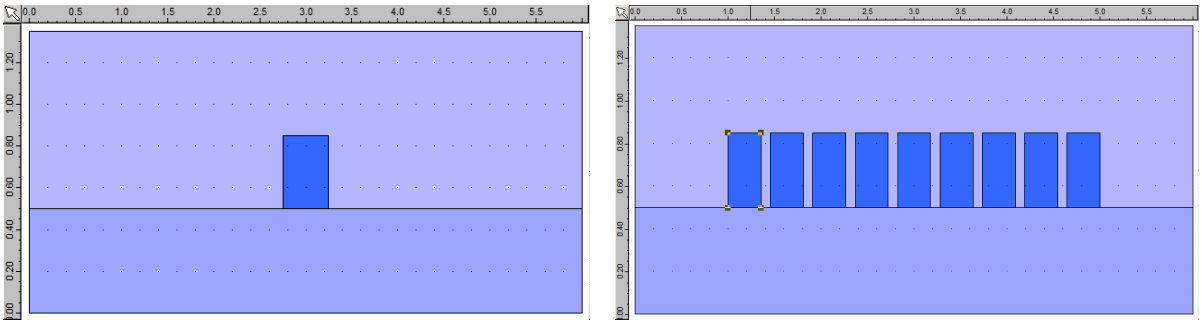

(b) (c)

Figure 3.1 The longitudinal taper, (a) top view of the 5 sections (b) cross section of the left end, (c) cross section of the right end.

The 0.5 µm width of the access waveguide in the first section is reduced to a 0.355 µm width waveguide in the second section using an exponential taper of the central waveguide. In the

following sections all waveguides with the exception of the additional outer pair are straight and parallel with a gap of 0.1 µm between adjacent side walls. The length of each section is 50 µm. Figure 3.1 shows a top view and side views at the both ends of the taper, which consists of 5 sections including the access waveguide.

Figure 3.2 shows the Ex and Ey mode profiles at the left end of the taper with the effective index of 2.72 and 2.51 respectively, on an access waveguide with a width of 0.5 µm.

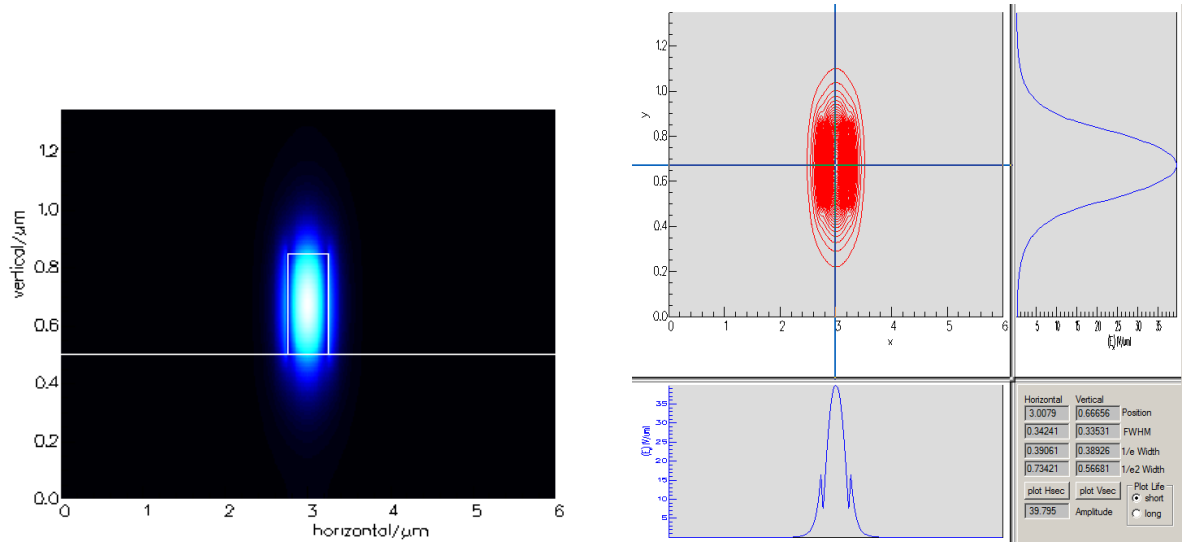

(a)

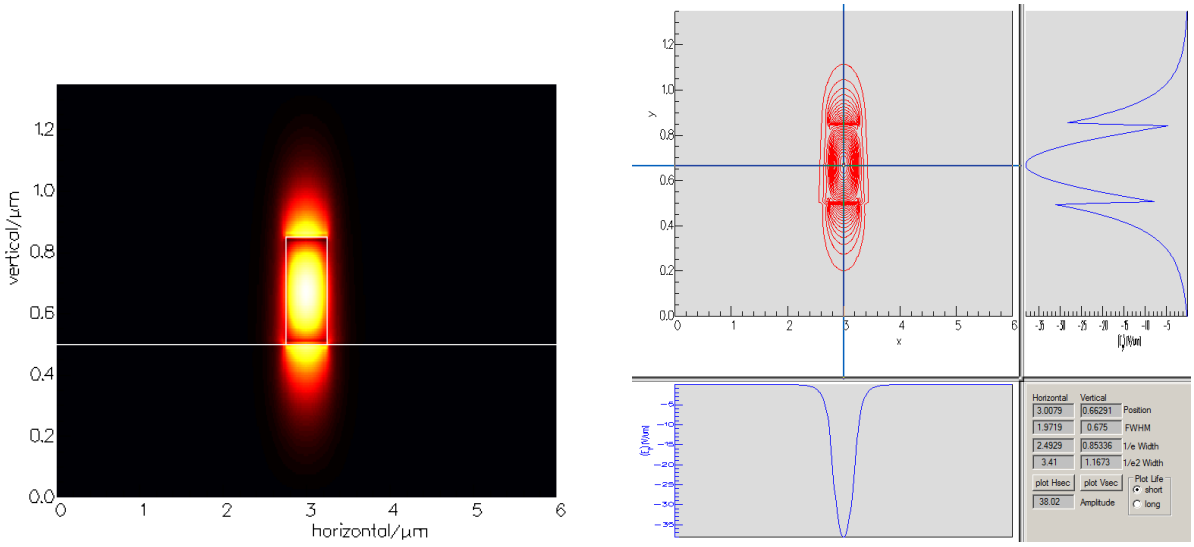

(b)

Figure 3.2 (a) Ex mode profile at the left end taper (b) Ey mode profile at the left end taper; on an access waveguide with the width of 0.5 µm.

Figure 3.3 shows the Ex and Ey mode profiles at the right end of the taper where the effective mode indices are 2.39 and 2.49 respectively, on slotted waveguide composed of a

multi-waveguide array with individual waveguide width of 0.355 µm and air gap of 0.1 µm edge to edge.

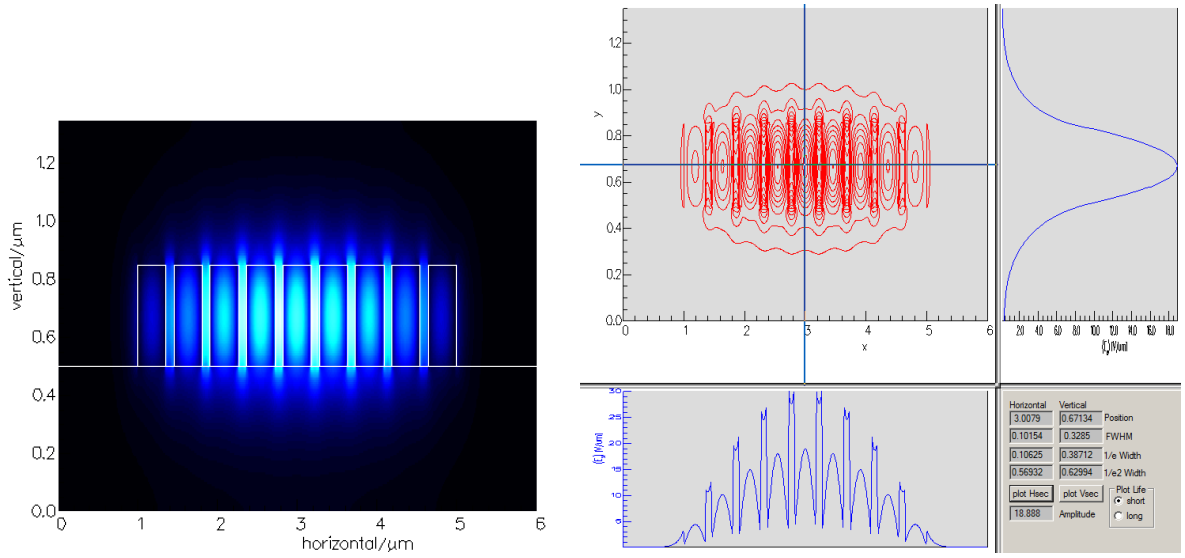

(a)

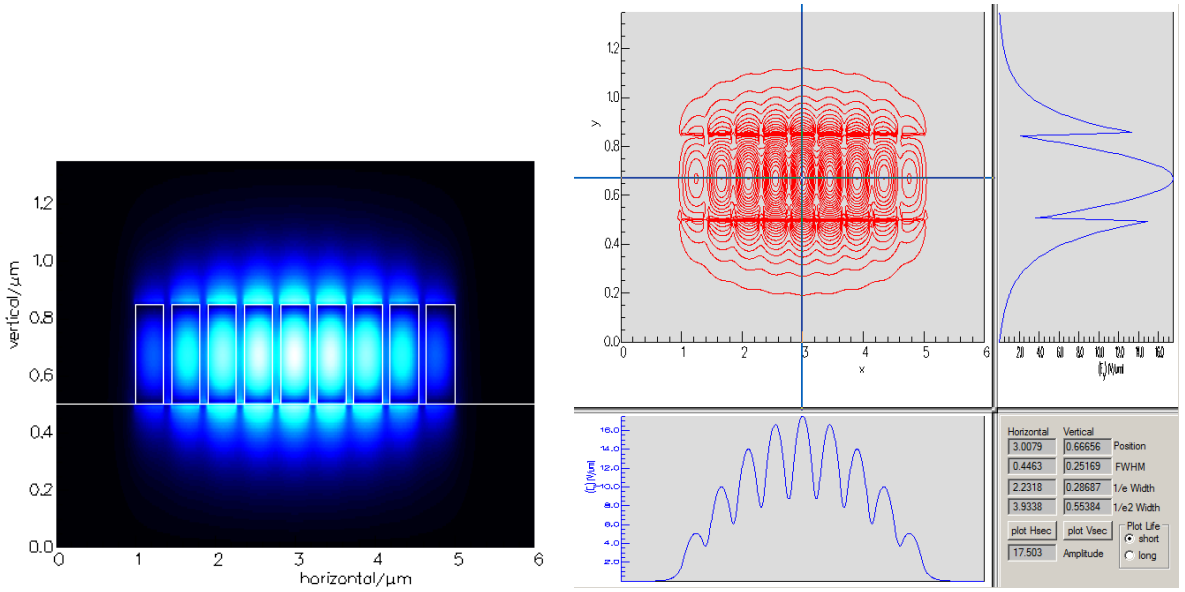

(b)

Figure 3.3 (a) Ex mode profile at the right end taper (b) Ey mode profile at the right end taper; on slotted waveguides with the width of 0.355 µm and the air gap of 0.1 µm edge to edge.

A 3D simulation on the longitudinal taper shows a transmission of 92% for Ex mode (-0.36 dB loss) and a transmission of 99% for Ey mode (-0.043 dB loss). Figure 3.4 shows a top view of the wave propagation in the longitudinal taper and a cross section of the mode at the right end.

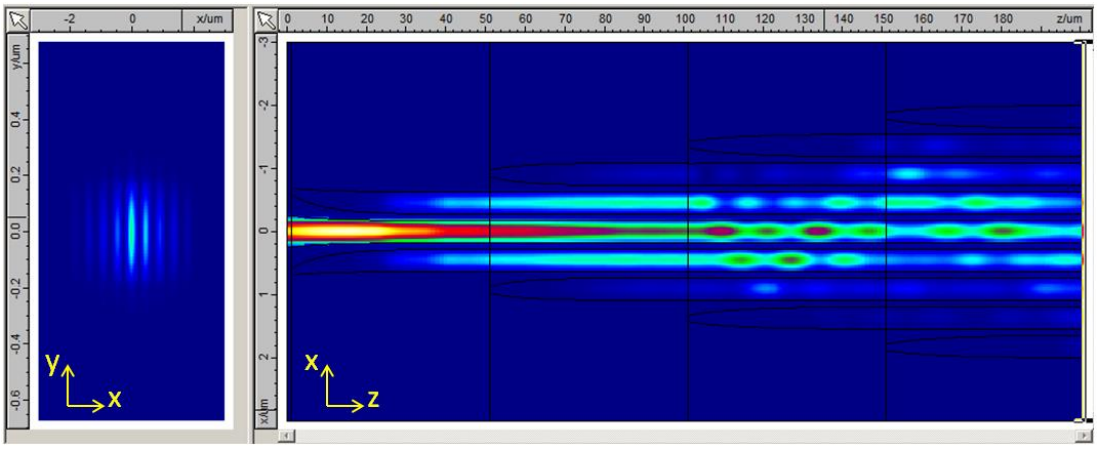

Figure 3.4 A 3D propagation simulation of the longitudinal taper, left: a cross section of the right end mode. The side panel illustrates the field intensity profile at the right-hand end of the taper. The purity of the transition of the fundamental mode of the access guide to the fundamental mode of the slotted waveguide mode can be observed. The interference seen on the visualisation of the total intensity of the light propagating along the tape is misleading for reasons explained in the main text.

The misleading nature of the visualisation despite the high transmission is due to the strong side lobes of the higher order modes in locations where the side-lobes of the fundamental mode are weak. Even if very weakly excited, the side lobes of the higher order modes can be comparable to the fundamental mode amplitude towards the edge of the structure. Moreover, the magnitude of the fluctuation due to interference of a strong wave and a weak wave is disproportionate to their respective intensities. Let P_0 and P_1 denote the local intensity (or equivalently the local power in a specified area), then the fluctuation of the intensity of the total field is:

$$\left|\sqrt{P_0} \pm \sqrt{P_1}\right|^2 = P_0 + P_1 \pm 2\sqrt{P_0 P_1} \tag{3.1}$$

where the positive sign corresponds to constructive interference and the negative sign corresponds to destructive interference. Hence:

$$\delta = P_1/P_0 \qquad \Longrightarrow \qquad 2\sqrt{P_0 P_1}/(P_0 + P_1) = 2\sqrt{\delta}/(1+\delta) \tag{3.2}$$

For example:

$$P_1/P_0 = 10\% \qquad \Longrightarrow \qquad 2\sqrt{P_0 P_1}/(P_0 + P_1) = 57\%$$

$$P_1/P_0 = 3\% \qquad \Longrightarrow \qquad 2\sqrt{P_0 P_1}/(P_0 + P_1) = 33\%$$

That is, if the weak mode has an intensity at some location that is only 10% of the intensity of the main mode at the same location a fluctuation in intensity as great as 57% may be expected, moreover, if the weak mode has an intensity at some location that is as little as 3% of the intensity of the main mode at the same location a fluctuation in intensity as great as 33% may be still expected. So the interference between the fundamental and another mode

with a fraction of the energy of the fundamental can be quite visibly observed in the total intensity.

The side lobes are shown in figure 3.5 for the fundamental and 1st order modes of Ex and Ey intensity profile at the length of 78 µm on the taper approximately where the visualisation starts to misbehave. The higher order modes are asymmetric modes and can be seen to have side-lobes that are greater in magnitude relative to the main lobes in comparison to the fundamental mode.

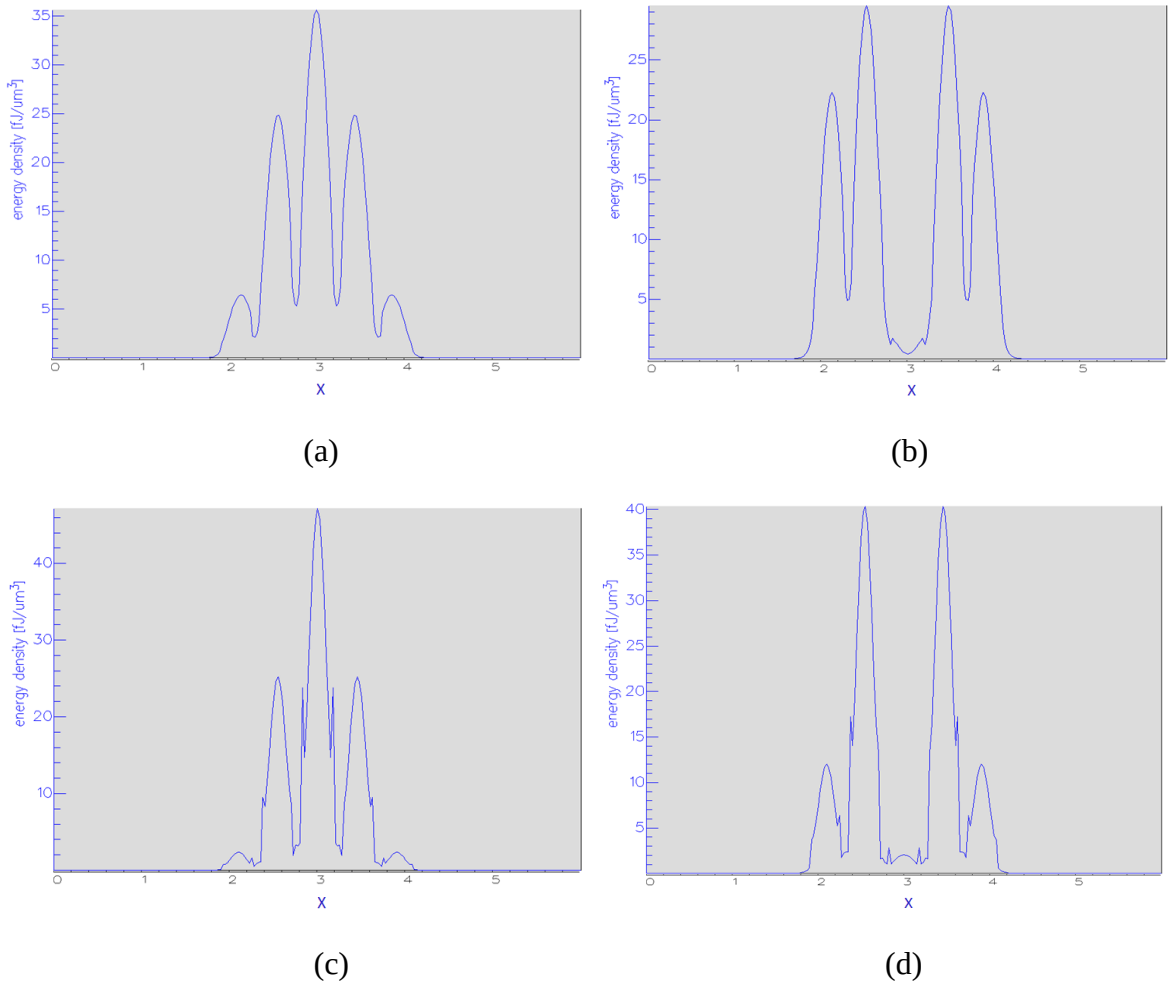

Figure 3.5 (a) Intensity profile of the fundamental Ey mode; (b) Intensity profile of the 1st order Ey mode; (c) Intensity profile of the fundamental Ex mode; (d) Intensity profile of the 1st order Ex mode; at 78 µm on taper on slotted waveguides with the width of 0.355 µm and the air gap of 0.1 µm edge to edge.

The separate simulations of the individual tapers and the multimode section of the longitudinal MMI provide complete confidence that the longitudinal MMI with its tapers connected will function correctly. Whereas a simulation of the complete device could dispel any remaining doubt, it was not possible to perform such a large scale simulation. A full-scale 3D simulation in FimmProp of a longitudinal MMI complete with tapers demands

excessive computer resources as the structure contains multiple parallel tapered waveguides which requires a progressive refinement of a partition of each section of the tapers in the computation and placing two slotted tapers in parallel for a 2×2 MMI only compounds the problem.

3.5 Summary

In this chapter, by applying homogenisation methods to more sophisticated structures, the Talbot effect in longitudinal and transverse multi-layer metamaterial structures has been considered using a Kronig-Penney model. In the deep subwavelength regime, the metamaterial can be described by its local anisotropic response but at optical frequencies this requires feature sizes that are beyond current volume fabrication processes. Spatial and temporal dispersion must be accounted for in structures meeting current fabrication constraints and subwavelength engineering can help by modifying the dispersion relation to improve the accuracy of the paraxial approximation. This may reduce the error of modal phase towards perfect imaging in MMIs which is one of the key components in PICs. On the basis of the simulations and the findings on modal phase error correction, a novel silicon integrated polarisation beam splitter based on the Talbot effect in a longitudinal metamaterial structure has been proposed for the first time in the manuscript reproduced within this chapter of the thesis with promising results of simulation. An adiabatic longitudinal taper with Ex transmission of 92% and Ey transmission of 99% has also been proposed for the first time in this chapter of the thesis to match the effective index and geometry of the access waveguides to the ports of the multimode region of the multi-slotted MMI. The results obtained suggest that a combination of transverse and longitudinal subwavelength patterning (i.e. a 2D metamaterial MMI) may offer a route to a compact, broadband, low modal phase error MMI. In the next chapter, 2D metamaterials are considered and devices based on them, such as Lüneburg lenses and MZI test structures are proposed and verified by simulation.

CHAPTER 4. 2D Metamaterial

4.1 Introduction

In Chapter 3, the one dimensional metamaterial was considered and its emergent properties of anisotropy and spatial dispersion explained. The ramifications of these properties on the Talbot effect led to the exploration of how the metamaterial might be engineered to suppress the modal phase error which limits the scaling of MMI port dimension. In this chapter, with the objective of supporting Chapter 5, which describes experiments on fabricated devices, the two dimensional metamaterial is considered and the effect of smoothly varying its structural parameters is illustrated by the design and simulation of a Lüneburg lens and adiabatic structures to interface SWG structures to conventional waveguides. The use of a MZI as a test harness for the 2D metamaterial is introduced and verified by simulation. All these structures were laid out and subsequently fabricated. The mask layout procedure using the Mentor Graphics Pyxis tool is consequently also explained in this chapter.

4.2 Contribution

The results provided in the first part of this chapter were published in the journal of Applied Physics A. In this paper the implementation of a metamaterial Lüneburg lens to provide Fourier optics on a chip and the design of adiabatic structures to provide a smooth interface between SWG structures and conventional waveguides are considered. The MZI structures to characterise the metamaterial structures and adiabatic transitions are introduced. In the second part of the chapter supplementary information is provided on the design, verification by simulation, and layout of the various test structures. I designed, verified by simulation, laid out all the structures and their variations; and drafted the manuscript. It was my suggestion to use confocal telescopes to test the Luneburg lenses. Dr. Hall contributed to my understanding of the theory, suggested using MMI couplers to form MZI test structures, provided advice on the selection of the variations necessary to limit the footprint to the allocated chip area, and assisted with the interpretation of the results and the revision of the manuscript.

4.3 Article

The following section is a reproduction of an article published in the Journal of Applied Physics A in 2016 [25].

Subwavelength Grating Waveguides for Integrated Photonics

Hamdam Nikkhah, Trevor J. Hall

Centre for Research in Photonics, University of Ottawa, School of Electronic Engineering & Computer Science, 800 King Edward Avenue, Ottawa, ON CANADA K1N 6N5

Abstract

Subwavelength waveguide gratings (SWG) are locally periodic structures with parameters that may vary slowly on the scale of a wavelength. Here the implementation of a Lüneburg lens as a SWG to provide Fourier optics on a chip and the design of the adiabatic structures that must be provided to interface SWG structures to conventional waveguides are considered. Preliminary findings are reported on the dispersion engineering of multimode interference couplers towards the ideal port phase relations needed in coherent applications.

Introduction

There is considerable interest in the field of Optical Communications in the integration of devices using a silicon-based materials platform to decrease component footprint and cost. Immense advances have been made; all the basic functions needed having been demonstrated. Nevertheless there remain technical and economic roadblocks to widespread adoption of the technology. A fundamental difficulty is that silicon is not suitable for light emission or, to a lesser extent, modulation. Si photonics has therefore been primarily restricted to the integration of passive functions. Active functions are provided by discrete devices such as off-chip lasers based on InP and separately packaged $LiNb0_3$ modulator circuits. Even then there remains a formidable challenge to the efficient transfer of light energy between the different waveguide technologies that must be interfaced.

Rapid and continuous progress in nanofabrication means that electromagnetic materials can now be engineered at a subwavelength scale. A recent break-through is to use sub-wavelength structures to tailor the refractive index and dispersion properties of integrated components. This has been applied with great success in a wide variety of applications of silicon photonics to radically reduce coupling loss, excess insertion loss and crosstalk; and to dramatically increase the operational bandwidth of components [1].

Fortunately, it is now practical to engineer the optical properties of structures on a chip by subwavelength patterning in a single etch step of binary nanocomposite material with a feature size that is not limited to expensive high resolution techniques such as electron-beam lithography. This offers fabrication processes amenable to the economics of mass manufacture.

Our work focuses on sub-wavelength waveguide gratings (SWG): that are periodic on the scale of a sub-wavelength lattice with parameters that vary on a scale larger than a wavelength. In section 2 the SWG structure, the design & verification challenges and the principles of homogenisation are discussed. In section 3 results of simulations of graded SWG structures are presented and a Mach-Zehnder interferometer structure for the measurement of the effective refractive index of SWG is introduced. Section 4 provides a brief discussion on the use of SWG to control spatial dispersion in the context of approaching an ideal multimode interference couplers; and section 5 draws some conclusions.

Homogenisation

In photonic crystal structures a waveguide is typically created by introducing a line defect. At an operating frequency within the band-gap, guiding may occur due to the mirror-like effect of the lattice surrounding the defect. At an operating frequency outside the band-gap, guiding may occur when the effective index of the lattice is lowered from that of the line defect (e.g. by hole inclusions). Sub-wavelength waveguide gratings are a sub-category of photonic crystal structure that operate at frequencies below the band-gap and require no surrounding lattice to guide. The fundamental wave-guiding principle is the propagation of the Floquet-Bloch modes of the SWG. Silicon SWG crossings and photonic wires have been demonstrated that have experimentally measured losses of -0.07 dB per crossing and 3.1 dB cm^{-1} respectively [2], which is astonishing given that the light passes through 60,000 interfaces every centimeter.

The combination of sub-wavelength scale nanostructures with overall component dimensions measured in hundreds of wavelengths creates computational problems of massive scale as the current tools require computational meshes that are sufficiently fine to adequately sample the nanostructure. Available tools rapidly run out of resources, or produce results that cannot be trusted. The absence of a reliable means to model and simulate large scale nanostructures is a major roadblock to advances in nanophotonics. Current tools for component simulation require sub-wavelength computational meshes that can only be applied to nanostructured

regions a few wavelengths in extent. Modelling at larger scales requires an abstraction of the properties of the nanostructure, which summarises its properties pertinent to the larger scale and smooths over the detail at the smaller scale. This abstraction is known as homogenisation. Investigation of the behaviour of the mode and effective mode index with respect to fill factor of the patterned structure outside parameter regions where simple effective material theory applies is the motivation for the study reported in this paper.

There is a vast literature on homogenisation. Its classic roots are the Clausius-Mossotti equation [3] that links the electrodynamics of continuous media to their atomic structure and the mixture formulae of Maxwell-Garnet [4] for the constitutive parameters of composite materials. Early studies applied long-wavelength asymptotic approximations because all but simple problems, such as the 1D lamellar structure analysed by Rytov [5], are intractable theoretically. A resurgence of interest in homogenisation can be traced to Prof. Sir John Pendry's corpus of work on negative refractive index materials, first postulated by Veselago [6]; and to an influential paper by Smith & Pendry [7] in which they pointed out that the electromagnetic fields in a unit cell of a photonic crystal may be calculated advantageously by commercial tools; albeit there remains additional coding to complete the homogenisation. The method of Smith & Pendry has been shown to be flawed in certain circumstances [8]; but that of Pérez-Huerta et al. [9], which draws on early work by Mochán & Barrera [10], and Mochán et al. [11] is compelling.

In the case of periodic dielectric structures, one may use a (commercially available) band solver to find the homogenised parameters for internal Bloch modes that describe light well away from the surface of a finite sized photonic crystal where the translation symmetry is broken. The Bloch mode expansion must be completed by evanescent Bloch modes, i.e. modes with a complex Bloch wave-vector, which represent waves bound to the surface [12]. Commercial band solvers assume a material of infinite extent; consequently, resort must be made to general purpose Finite Element Method (FEM) or Finite Difference Time Domain (FDTD) solvers with additional programming effort. For a slab, one must match a Rayleigh plane wave expansion in the exterior domain to a Bloch plane wave expansion in the interior domain. The transverse component of the exterior plane wave and internal Bloch wave-vector must match by field continuity considerations. This justifies the use of the effective index of the Bloch mode as the homogenised index. It also suggests that the correct method of smoothing the field is to set the amplitude of spatial frequencies outside the first Brillouin zone to zero. A plane wave expansion approach similar to that used in band solvers can then be used to solve for the averaged fields to find material constitutive parameters. The result is essentially exact: the full band structure accessible by an exterior wave may also be reconstructed from the homogenised parameters.

Graded structures may be described by introducing two spatial scales; a 'slow' base-space co-ordinate pertinent to the variation of the nanostructure parameters (e.g. atom size, lattice 'constant') and a 'fast' tangent space coordinate pertinent to a periodic extension of the local nanostructure. The hope is that the structure in the neighbourhood of the base-space position is well approximated by the periodic extension of the nanostructure at that position. This is an asymptotic approximation that we have applied with success in numerical experiments on the metamaterial Lüneburg lens [13]. A similar approach to grading but relying on the less precise Maxwell-Garnett effective index formulae is described in [14].

Simulation Results

An interest in Fourier optics on a chip [13] provided our starting point: the implementation a planar Lüneburg lens as a slowly-varying photonic crystal slab waveguide (or 'metamaterial'). A hexagonal lattice was chosen as this offered a band structure with circular equi-frequency contours in the long wavelength operational limit, shown in Figure 1.

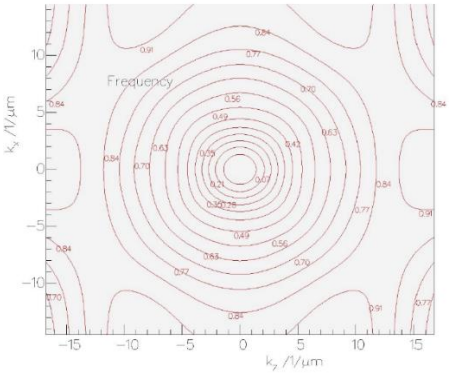

Figure 1. The equi-frequency contours of the band surface displayed on the wave vector plane.

The local index was found by two methods. In the first method, a band solver was used to predict the homogenised index of a Bloch mode in a two dimensional photonic crystal of infinite extent. This homogenised index was then used as the core index in an orthodox model of an asymmetric slab waveguide to predict the effective index of the mode bound to the slab.

In the second approach, a 3D band unit cell is defined by periodically replicating, in the direction normal to the plane, the waveguide structure containing a single 2D unit cell in the plane. The out-of-plane period is chosen large enough that the waveguide fields are negligible at the upper and lower end faces of the unit cell. A 3D band solver is then used to directly determine the effective index of the fundamental mode of the patterned slab waveguide structure. A representative 3D unit cell is shown in Figure 2, consisting of three layers of air, metamaterial and silica.

The assumption of an infinite number of replications of the 3D unit cell normal to the plan of the slab is an approximation given that the slab is only one unit cell thick, which causes a small error in the field due to the periodicity assumption. Hence, the 3D band structure solver for a 2D periodic medium can give an accurate value of the effective index of the metamaterial but is computationally more demanding.

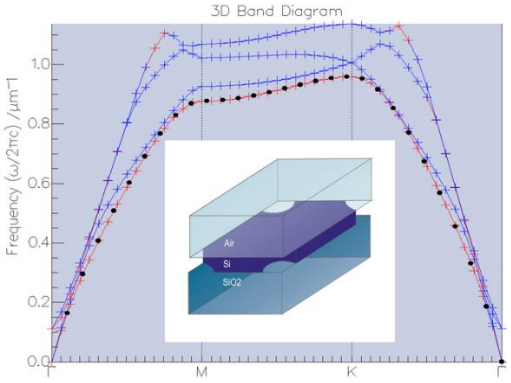

Figure 2. The 3D unit cell analysis and the band diagram of 3D FDTD simulation.

Remarkably, the two methods agree very closely [13]. This indicates first that the evanescent fields generated at the upper and lower boundaries of the core do not significantly tunnel across the core despite its small thickness of the of 300 nm and second that the field continuity conditions at the core boundaries differ little from that for continuous media despite the patterning of the core.

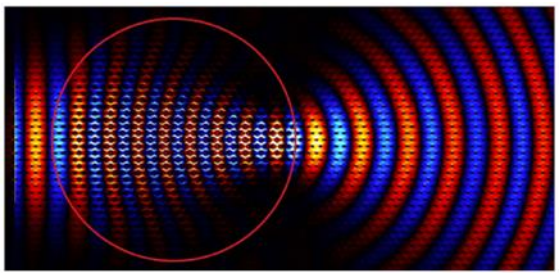

Figure 3. A FDTD simulation of an incident plane wave focused by a planar graded metamaterial lens. The local structure of the Bloch wave as a product of a periodic function with the same period as the lattice and a Bloch phase factor describing the phase advance across unit cells is clearly visible.

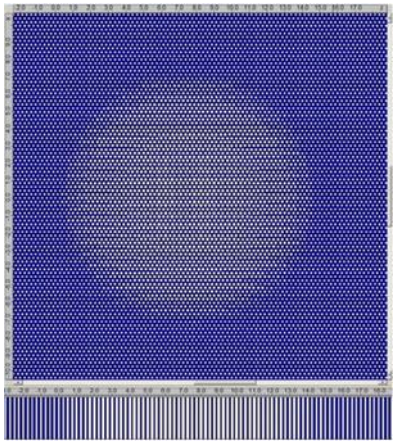

Figure 4. A metamaterial Lüneburg lens with a diameter of 15 μm; with the rod diameters varying from 151 nm on the rim to 202 nm in the centre placed on a hexagonal lattice with lattice constant of 250 nm. The effective refractive index on the rim was set to 1.4, which leads to an effective index at the centre of the lens of 1.98. The calibration used was appropriate to 2D FDTD simulation.

To fully exploit the flexibility offered by subwavelength grating structures they need to be integrated and interconnected by conventional waveguides. In the case of the Lüneburg lens, it is fortunate that the structure

naturally features an adiabatic transition from the exterior domain at the rim to the interior structure of the lens [13]. The lens can be made in two ways; either using air holes in silicon layer or silicon rods in air. Figure 3 shows an example of subwavelength structure implementation of a planar Lüneburg lens, using air holes in silicon layer. Figure 4, shows the metamaterial lens structure using silicon rods in air. The structure of air holes in silicon layer is preferred in this study because it offers a wider range of homogenised index compared to silicon rods in air.

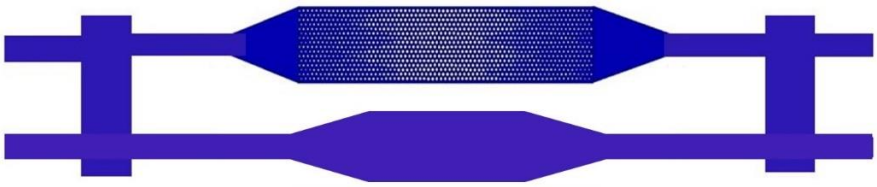

Figure 5. MZI structure with one arm patterned structure and the other arm silicon.

In general, however, it is necessary to provide adiabatic structures that not only adapt waveguide dimensions but also adapt the homogenised index. Figure 5 shows an example of a Mach-Zehnder interferometer with a length of subwavelength grating waveguides within their arms adapted to standard silicon waveguides by adiabatic tapers. The SWG is interfaced to standard silicon waveguides first by an adiabatic taper with varying width and constant refractive index and then by an adiabatic taper of constant width but varying homogenised index. The lower arm contains standard silicon waveguide and identical in the length with the upper arm but the length is deducted only the length of centre section of the upper arm that contains the SWG section with the holes in constant diameter. The imbalance between the arms will allow the experimental measurement of the homogenised index. Figure 6 shows an enlargement of the arm showing the detail of the homogenised refractive index taper, while the diameter of the air holes is increasing from left to right. Figure 7 shows the first SEM released of the two arms of MZI at the central section where the diameter of holes are constant. These structures are an example of a case where a nanoscale simulation over the full device, say using FDTD, is not reliable. Rather, we have relied on simulation of the homogenised structures using FimmProp as shown in Figure 8, together with the calibration procedure described for the Lüneburg lens.

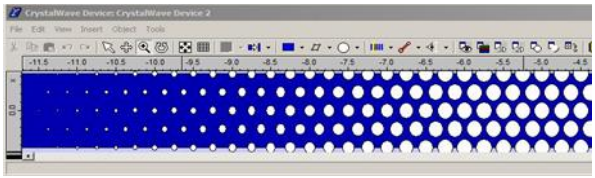

Figure 6. An enlargement of the upper arm of the MZI showing detail of the homogenised refractive index taper.

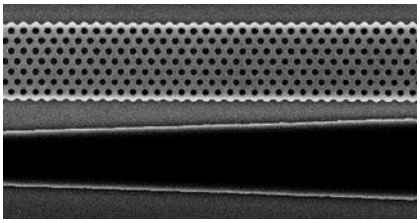

Figure 7. The SEM of two arms of MZI at the central section, holes with constant diameters.

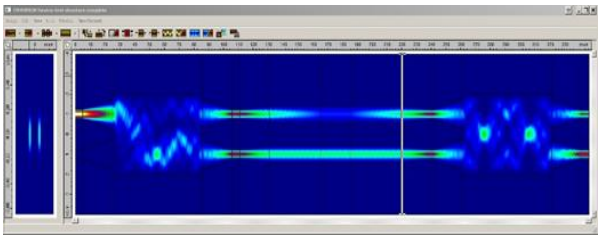

Figure 8. FimmProp simulation of a MZI structure with upper arm containing homogenised SWG waveguide and the lower arm containing standard silicon waveguides.

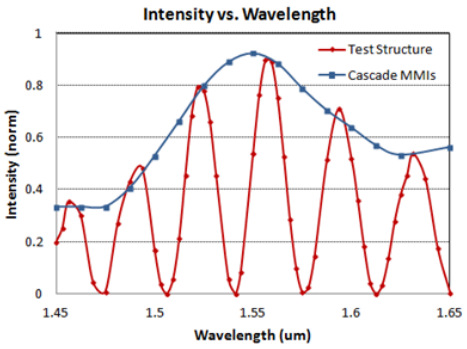

Figure 9. MZI output intensity against wavelength for a SWG test structure of the length 20 μm (red) illustrating the spectral fringes due to the optical path imbalance introduced by the SWG section. Also shown is the output intensity of an empty MZI (back-to-back MMIs) (blue) which follows the envelope of the spectral fringes.

The experimental confirmation of the validity or otherwise of the calibration approach awaits the Lüneburg lens and MZI structures to come out of fabrication.

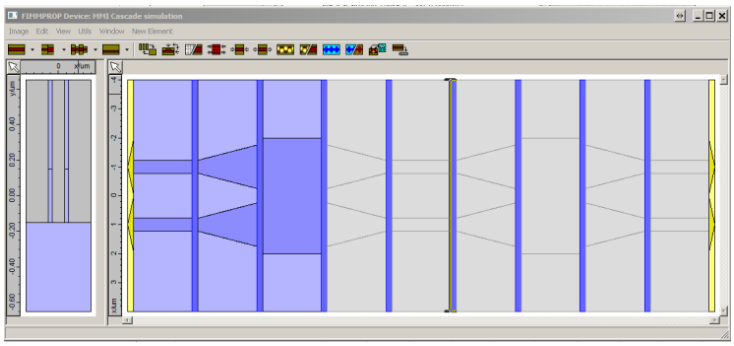

Figure 10. Back-to-back MMIs to obtain the envelope of the spectral fringes.

Figure 9 shows the intensity at the output port of the MZI with wavelength scanned from 1.45 μm to 1.65 μm for a SWG test structure (shown in Figure 8) of length 20 μm (red) which illustrates the spectral fringes due to the optical path length imbalance introduced by the test section. These fringes provide a measurement of the homogenised refractive index. Also shown is the output intensity of an empty MZI (back-to-back MMIs, shown in Figure 10) (blue) which follows the envelope of the spectral fringes.

Discussion

Now that coherent transmission is so well entrenched, extra care is required to control the phase in addition to the amplitude of light propagating in photonic integrated circuits. The phase relationship between the ports of splitters and couplers is particularly important in applications to microwave frequency multiplication, advanced I-Q modulation, optical hybrids for coherent receivers and more [15-20]. In particular, this leads to the search for a perfect Multimode Interference coupler (MMI) in which subwavelength waveguide gratings are used to engineer the dispersion and anisotropy of the MMI so that a practical device provides close to the ideal (but normally approximate) self-imaging behaviour. To this end, a slab waveguide patterned as a photonic crystal in one-dimension is being investigated. Very good agreement between the bandsolver and the Kronig-Penney model has been obtained for Bloch vectors in the plane of the slab and not just normal to the grating structure. There is however a substantial difference between the mapping of the homogenised index to the mode effective index via the asymmetric slab waveguide model and the predictions of the band-solver for a 3D unit cell. Whether this is because of the difficulties in ensuring that a commercial band solver finds the correct band structure for this geometry or the assumptions inherent the indirect approach remain valid is the subject of further investigation.

Conclusions

The continuing improvement in advanced lithography techniques (such as immersion lithography, extreme-UV lithography, nanostepping lithography) will enable accurate, large-volume production of subwavelength structures and devices. The use of SWG structures in integrated photonics devices is thus likely to continue to expand, enabling new functionalities and devices to be designed and fabricated, and these SWG structures will become an essential tool set in advanced photonic design libraries.

Acknowledgements

The authors are indebted to Tom Davies of Technix for his technical support of the Photon Design suite of software tools used in the work. The authors acknowledge the financial support of the Natural Sciences and Engineering Research Council of Canada (NSERC) though an Engage Grant with Technix. Trevor J. Hall is grateful to the Canada Research Chair (CRC) Program for their support of his CRC-I in Photonic Network Technology.

References

[1] R. Halir, et al., “Waveguide sub-wavelength structures: a review of principles and applications”, *Laser & Photonics Reviews* 9.1: 25-49, 2015.

[2] P. J. Bock, P. Cheben, J. H. Schmid, J. Lapointe, A. Delage, D. X. Xu, S. Janz, A. Densmore, T. J. Hall, “Subwavelength grating crossings for silicon wire waveguides”, *Opt. Exp*., 18(15), 16146-16155, 2010.

[3] J H Hannay, “The Clausius-Mossotti equation: an alternative derivation”, *Europ. J. Phys*, **4**, 141-143, 1983.

[4] J. C. Maxwell Garnett, “XII. Colours in metal glasses and in metallic films”, *Phil. Trans. Royal Soc*. A, **203**, 385-420, 1904.
[5] S. M. Rytov, “Electromagnetic properties of a finely stratified medium”, *Sov. Phys. JETP*, **2**, 466-475, 1956.
[6] V. G. Veselago, “The electrodynamics of substances with simultaneously negative values of and μ”, *Sov. Phys. Usp.* **10,** 509-514, 1968.
[7] D. R. Smith, J. B. Pendry, “Homogenization of metamaterials by field averaging (invited paper)”, *J. Opt. Soc. Am. B*, **23**(3), 391-403, 2006.
[8] V. V. Gozhenko, A. K .Amert, K. W Whites, “Homogenization of periodic metamaterials by field averaging over unit cell boundaries: use and limitations”, *New J. Physics*, **15**, art. 043030, 2013.
[9] J S Pérez-Huerta, G. P. Ortiz, B. S. Mendoza, W. L. Mochán, “Macroscopic optical response and photonic bands”, *New J. Physics*, **15**, art. 043037, 2013.
[10] W. Mochan, R. G. Barrera, “Electromagnetic response of systems with spatial fluctuations. I. General formalism”, *Phys. Rev. B*, **32**(8), 4984-4988, 1985.
[11]W. L. Mochan, G. P. Ortiz, B. S. Mendoz, “Efficient homogenization procedure for the calculation of optical properties of 3D nanostructured composites”, *Opt. Exp*., **18**(21), 22119-22127, 2010.
[12]C. Fietz,Y. Urzhumov, G. Shvets, “Complex k band diagrams of 3D metamaterial / photonic crystals”, *Opt. Exp.*, **19**(20), 19027-19041, 2011.
[13] H. Nikkhah, T. Hall, “Metamaterial Lüneburg lens for Fourier optics on-a-chip”, *SPIE OPTO. International Society for Optics and Photonics*, 2014.
[14] B. Vasic, G. Isic, R. Gajic, K. Hingerl, “Controlling electromagnetic fields with graded photonic crystals in metamaterial regime”, *Opt. Exp.*, **18**(19),20321-20333, 2010.
[15] M. Hasan, R. Guemri, R. Maldonado-Basilio, F. Lucarz, J. de Bougrenet de la Tocnaye, T. J. Hall, “Theoretical analysis and modeling of a photonic integrated circuit for frequency 8-tupled and 24-tupled millimeter wave signal generation”, *Optics Letters*, **39**(24), pp. 6950-6953, 2014.
[16] M. Hasan, R. Maldonado-Basilio, T J Hall, “Comments on X. Yin, A. Wen, Y. Chen, and T. Wang, 'Studies in an optical millimeter-wave generation scheme via two parallel dual-parallel Mach-Zehnder modulators, Journal of Modern Optics, 58(8), 2011, pp. 665-673”, *Journal of Modern Optics*, 62(7), pp. 581-583, 2015.
[17] R. Maldonado-Basilio, M. Hasan, H. Nikkhah, S. Abdul-Majid, R. Guemri, F. Lucarz, J.-L. de Bougrenet de la Tocnaye, T. J. Hall, “Electro-optic up-conversion mixer amenable to photonic integration”, Journal of Modern Optics, 2015.
[18] M. Hasan, R. Maldonado-Basilio, T. J. Hall, “Dual-function photonic integrated circuit for frequency octo-tupling or single-side-band modulation”, *Optics Letters*, 40, pp. 2501-2504, 2015.
[19] R. Maldonado-Basilio, M. Hasan, R. Guemri, F. Lucarz, T. J. Hall, Generalized Mach-Zehnder “Interferometer Architectures for Radio Frequency Translation and Multiplication: Suppression of Unwanted Harmonics by Design”, *Optics Communications*, (in press), 2015.
[20] S. Abdul-Majid, I. I. Hasan, P. J. Bock, T. J. Hall, “Design, Simulation and Fabrication of a 90 degrees SOI Optical Hybrid Based on the Self-imaging Principle”, *Photonics Europe 2010, Conference on Silicon Photonics and Photonic Integrated Circuits II, Brussels, Belgium*, 12-16 April, Proc SPIE, 7719, 2010, art. 77190E, 2010.

4.4 Metamaterial Lüneburg Lens Implementation

A Lüneburg lens may be implemented in planar form and provide a Fourier transform function on a chip by stigmatic imaging of an object at infinity in its rear focal plane [22, 26, 27]. The graded refractive index of a Lüneburg lens, which was first introduced by Rudolf Karl Lüneburg in 1944, is described by [28]:

$$n(r) = n_0\sqrt{2-(r/a)^2} \quad r \le a \qquad (4.1)$$
$$= n_0 \qquad\qquad r > a$$

where r is the distance from the centre of the lens, a is the outer radius of the lens, and n_0 is the ambient refractive index. The metamaterial Lüneburg lens design procedure was described in detail in Chapter 3 and 4 of my Master's thesis [22]. The implementation considered envisaged a SOI wafer with a silicon layer thickness of 350 nm [22]. The process used in this thesis uses an SOI wafer with a 300 nm silicon core thickness layer and consequently all design and verification by simulation were redone in this work. The effective refractive index of the Lüneburg lens is engineered by nano-structuring an SOI slab waveguide core layer. This offers the simplicity of single etch step in the fabrication process. The cylindrical inclusion is either solid (silicon) or voids (air); in a host that is either void (air) or solid (silicon) respectively. The inclusions may be placed on a regular sub-wavelength lattice and the diameter of cylinders varied according to the local effective index required. In the thesis work, the host is a silicon slab waveguide with cylindrical inclusion of air as it offers higher effective index with larger minimum feature size which would be otherwise limited by the fabrication process [22].

To assess the insertion loss that may arise from the approximation of a continuous graded index material by a graded metamaterial, the most useful test structure is a confocal telescope lens system in which two Lüneburg lenses are placed side-by-side with their rims touching on axis shown in Figure 4.1. In this way, the input to the lens through a single mode access waveguide may be considered as a point source at the rim of the lens. The first lens transforms the point source at its input rim to a plane wave at its output rim and the second lens then transforms the plane wave at its input rim to a point source at its output rim. The input access waveguide is thereby imaged onto the output access waveguide and any imperfection of the lenses will be registered as an excess loss.

In this design, each lens diameter is 15 µm with the effective index varying from 1.925 at the rim to 2.722 in the centre with the hole diameter of 0.182 µm and 0.093 µm respectively. A single mode ridge waveguide is used to launch the light in and out the telescope system (figure 4.2). The width of the access waveguide is 0.45 µm constrained by the fabrication process development kit (PDK), which gives a mode effective index of 2.527.

Figure 4.3 illustrates the fundamental Ex-like and Ey-like modes, in the single mode waveguide with a width of 0.45 µm, and silicon thickness of 0.3 µm.

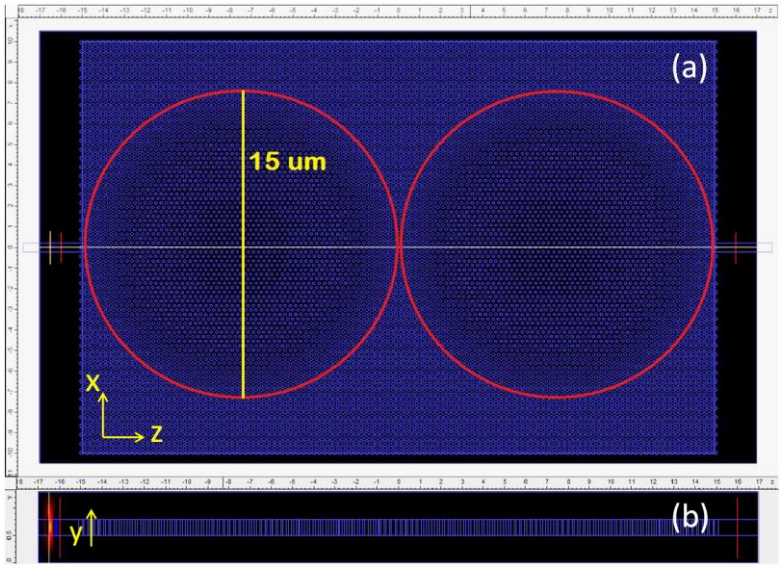

Figure 4.1 Confocal telescope Lüneburg lens system with each lens having a diameter of 15 µm; the two lenses are placed side-by-side with their rims touching on axis. (a) top view, (b) side view.

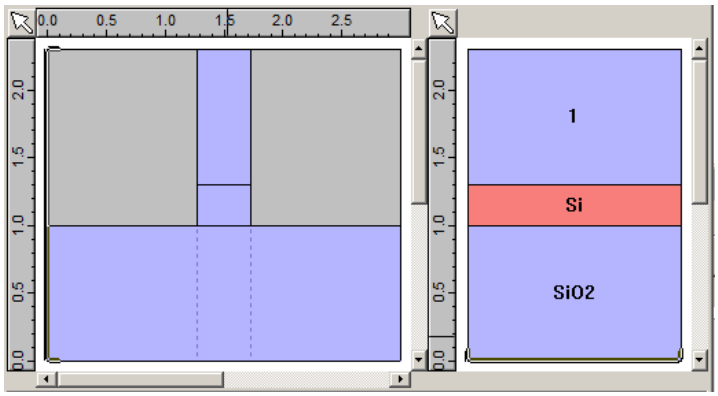

Figure 4.2 Waveguide with the width of 0.45 µm and height of 0.3 µm Si in the core.

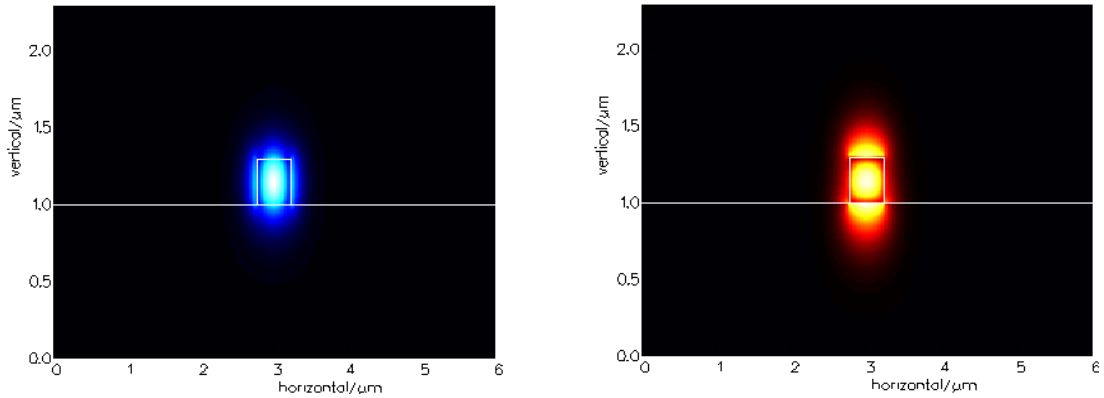

Figure 4.3 Mode profiles in the ridge waveguide of width 0.45 µm, with a silicon thickness of 0.3 µm. Left, fundamental Ex-like mode. Right, fundamental Ey-like mode.

A 3D finite difference time domain (FDTD) simulation was performed of the confocal telescope metamaterial Luneburg lens system by defining the three layers of air, silicon and silica with the thickness of 0.5 μm, 0.3 μm and 0.5 μm respectively. The thickness of claddings may appear small but it is sufficient for the fields at the window boundary to have decayed to negligible proportions. Increasing the thickness demands more computational resources for a fine computational grid. There is therefore a trade-off between the computational window size and the resolution of the computational grid, which was set to 0.015 μm.

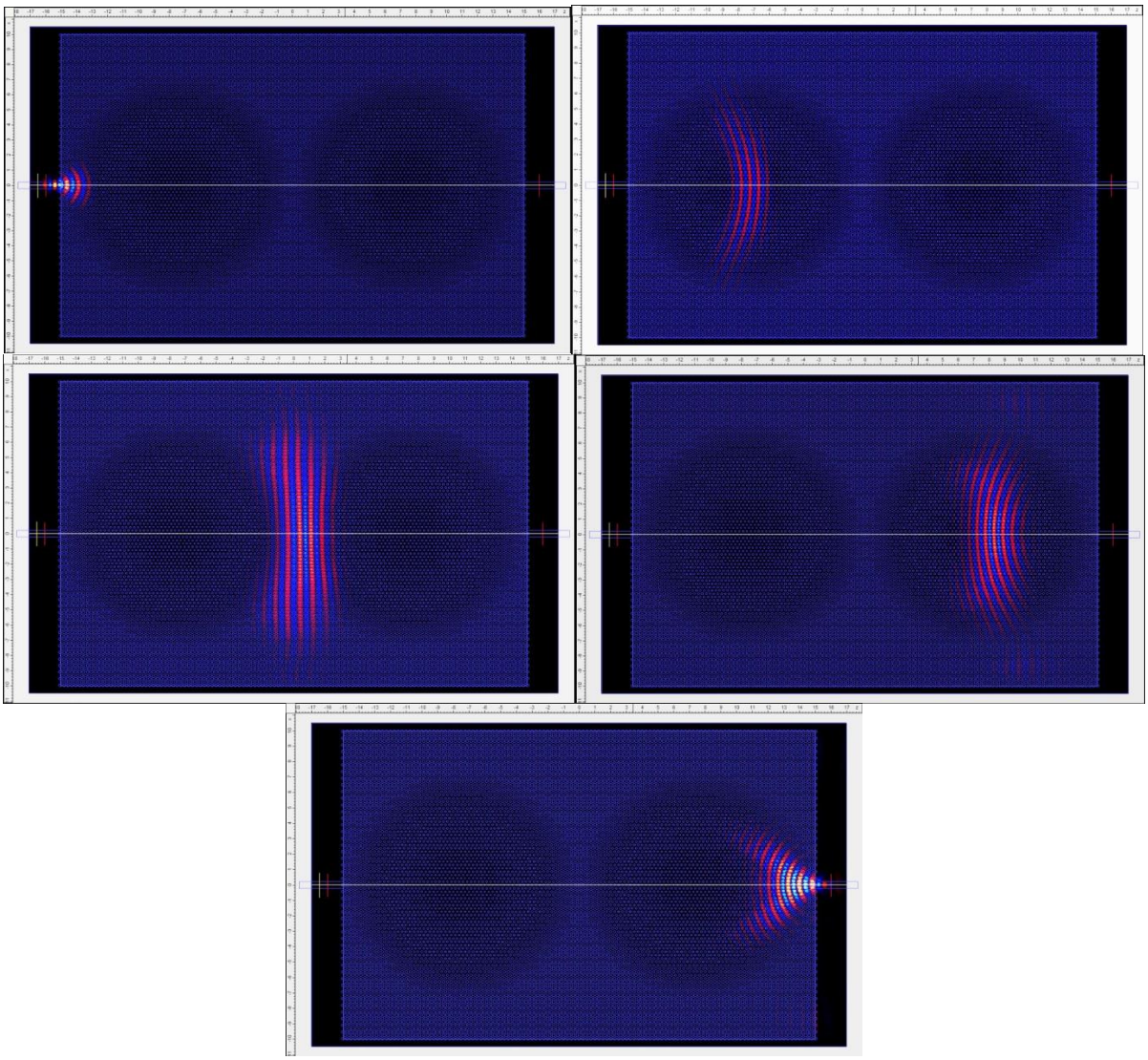

Figure 4.4 A sequence of frames of a 3D FDTD simulation of a confocal metamaterial Lüneburg lens telescope between two optical waveguides. A computational grid spacing of 15 nm and a mode excitor source with a sinusoidal pulse of 50 fs duration, for hole diameter changing from 0.182 μm on the rim to 0.093 μm in the centre.

A sinusoidal pulse field TE mode excitor with a duration of 50 fs was used to provide the relative flux measurements. The mismatch between the effective index of the access

waveguide causes a reflection at the rim. This can be resolved if there is more freedom in fabrication process, such as higher thickness of the core or tapering down the waveguide in case the width of waveguide is larger for a different process. Figure 4.4 shows a sequence of frames of a 3D FDTD simulation of a confocal Lüneburg lens telescope.

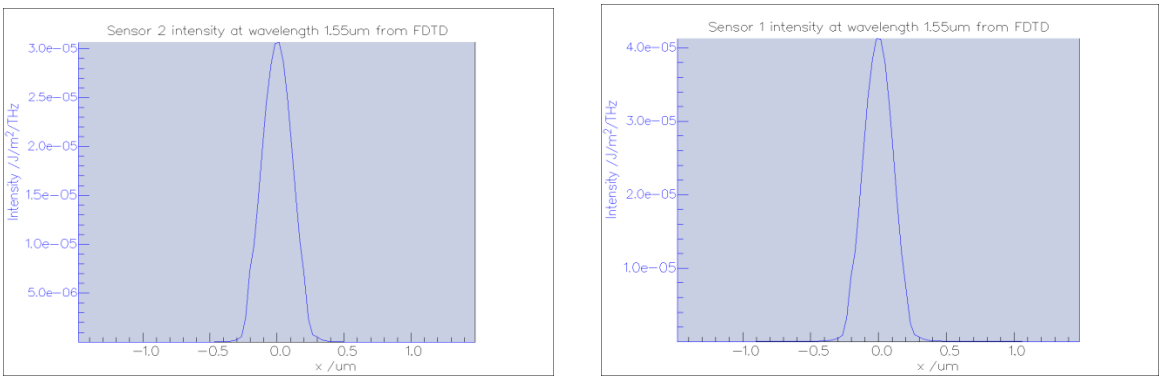

(a)

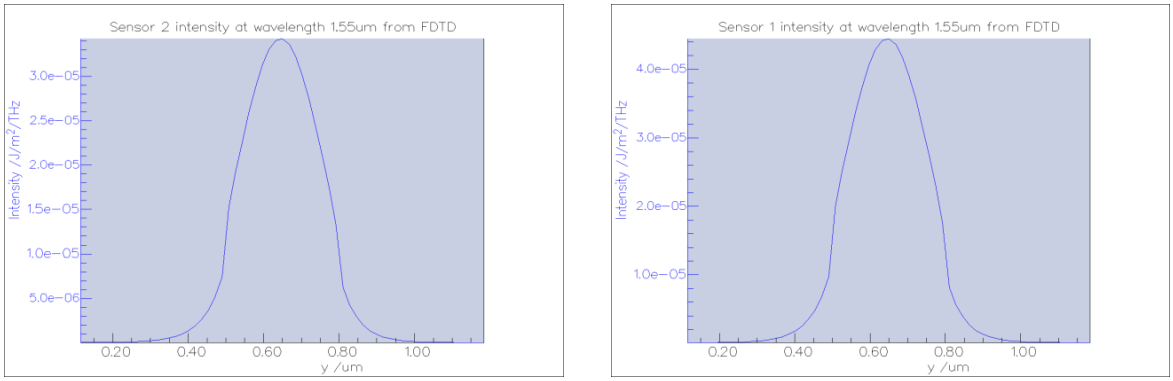

(b)

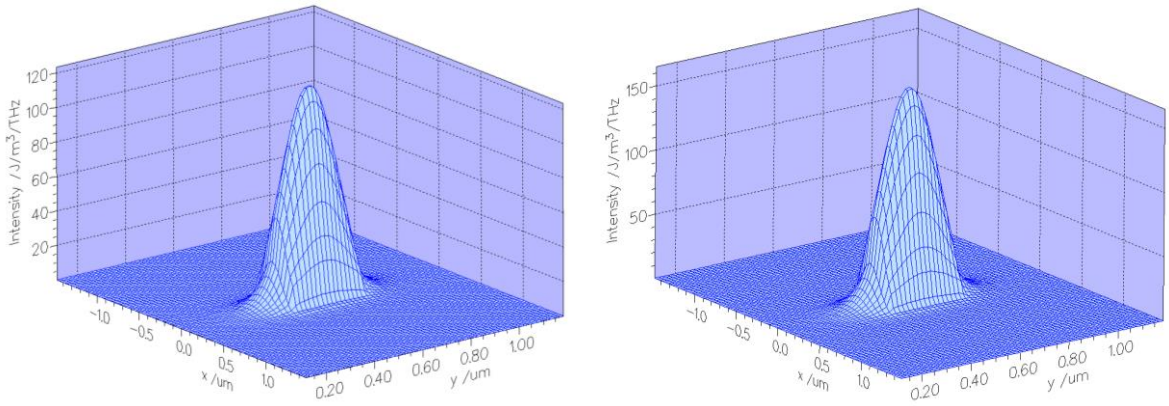

(c)

Figure 4.5 The intensity profile at the output waveguide (left), and at the input waveguide (right) for the two metamaterial lens system predicted by 3D FDTD simulation, a) the cross-section of the field in the x direction, b) the cross-section of the field in the y direction, c) a perspective plot.

Figure 4.5 shows the intensity profile on coordinate x and y (shown in figure 4.1) and on sensor 2 at the output waveguide and sensor 1 at the input waveguide. The predicted total

system insertion loss is -1.035 dB which is -0.517 dB per lens with the assumption that the waveguide-lens insertion loss is small.

4.5 Test Structure Implementation

It was decided to use MZI test structures to better investigate the dependence on structural parameters of the effective index of a mode guided within a metamaterial waveguide; the transition between metamaterial structures and conventional waveguides on PICs; and to compare the results of simulations with the results of experimental measurements of fabricated structures. A pair of 2×2 MMIs, designed in accordance with the methodology given in my Master's thesis [22], were used to construct the MZI. At each port, an adiabatic taper is used to make a smooth transition from the access single mode waveguide to the multimode region of the MMI. Table 4.1 provides the dimensions of the MMI.

Table 4.1 Specification of MMI and taper at its ports

MMI	Dimensions (µm)	Taper	Dimensions (µm)
Width	4	Width Narrow	0.45
Length	60.7344	Width wide	1.5
Core Height	0.3	Length	20
Core material		Silicon	
Under-cladding material		Silica	
Over-cladding material		Air	

Figure 4.6 shows a simulation of the taper in FimmProp. The simulator partitions the adiabatic structure into segments at different cross-sections and calculates the field at each cross-section, refining the partition to achieve a specified accuracy. It must be taken into account that the resolution of the computation should be sufficient that each segment can be treated accurately as a straight waveguide in addition to the structure as a whole possessing the desired adiabatic behaviour. A transmission of 99.77% was predicted in a 3D simulation.

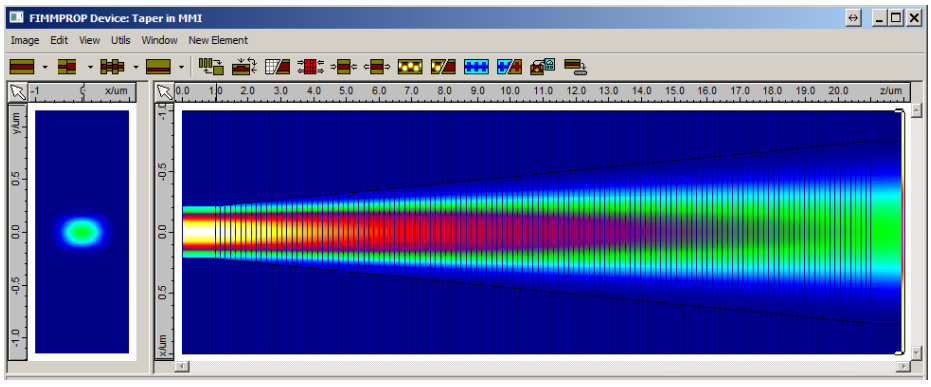

Figure 4.6 The computational cross-sections in the Fimmprop simulator of a taper with a length of 20 µm and with a width of 0.45 µm at the narrow end and the width of 1.5 µm at the wide end.

The fundamental Ex-like mode profiles are shown in Figure 4.7.

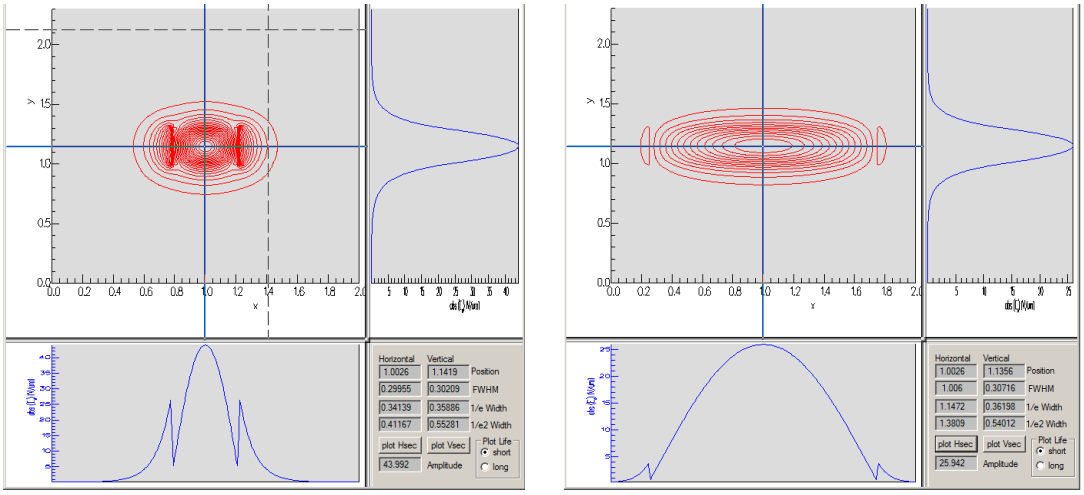

Figure 4.7 The absolute Ex-like profile of the taper with a length of 20 µm (left), at the narrow end of the taper with a width of 0.45 µm (left) and at the wide end of the taper with width 1.5 µm.

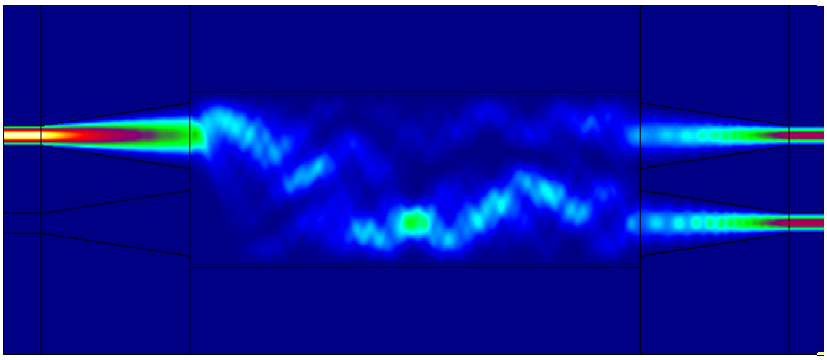

Figure 4.8 A 2×2 MMI splitter with the width of 4µm and the length of 60.73 µm.

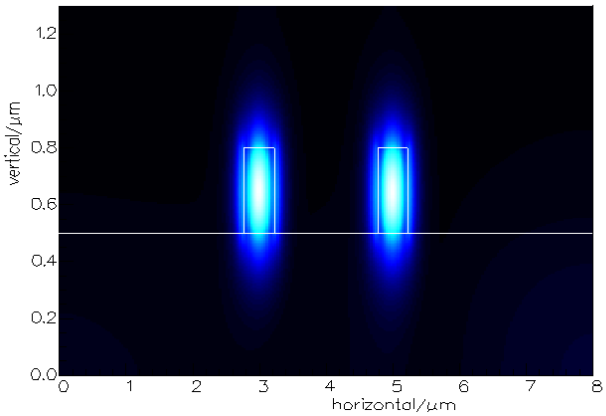

Figure 4.9 The fundamental mode profiles on the output ports of the 2×2 MMI.

MMIs can be designed for different purposes such as splitter (symmetric or non-symmetric) or cross-overs, only by adjusting the length of the multimode region which is related to the corresponding Talbot effect length. The MMIs that are used in a MZI function as splitters and the length of the multimode region is chosen so that light emanating from an excited input port is split equally between the two output ports. The simulation of a complete

individual MMI with the specifications given in Table 4.1 predicts a transmission of more than 48% on each output port. Figures 4.8 to 4.10 show simulation of the MMI and the output field profile for an Ex-like mode.

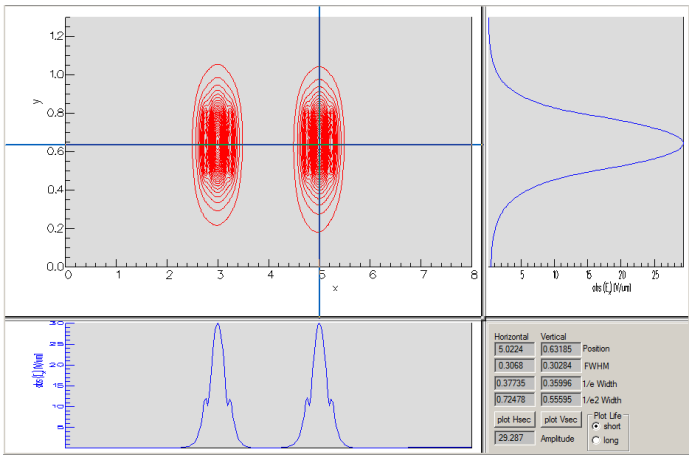

Figure 4.10 The Ex-like field profile on the two output ports of a 2×2 MMI used as a 1×2 power splitter.

Two MMIs back to back form a simple MZI that functions as a cross-over if the two arms are identical and consequently provides a sensitive test of the imbalance caused by fabrication errors. To investigate the sensitivity to errors, the width of the arms was changed differentially and it was found that for every 0.31 nm change in the differential width of arms 1100 µm long, a $\boldsymbol{2\pi}$ phase change would occur. So in the case where an exact phase shift is important, a slight fabrication error causes a large impairment of the device function. This can be mitigated by keeping the arms short, using an over cladding, and by better process control to ensure both waveguides have only common width variations and minimal differential variations, or by using phase controllers [29]. In contrast the tolerance of the MMIs to the width and length change in the multimode region is high; 8 µm for the length change and 0.3 µm for the width change for 1dB loss.

4.6 MZI Designs and Simulation

The chip that was fabricated for the experimental component (see Chapter 5) of this research, featured three different sets of MZI test structures. Each set was distinguished by a common width of 1.732 µm, 0.866 µm and 0.433 µm of the metamaterial section of the MZI arms. These widths were obtained on the basis of an integer number of one, three and seven rows of complete holes. A half row at the two sidewalls was retained to avoid an asymmetric cut of the hexagonal lattice and to maintain the periodicity of the lattice under the assumption that the sidewalls act as mirrors given the high index contrast. Each set is divided into three subsets with respect to the length of 0 µm, 50 µm, 200 µm and 1000 µm of the central region where the holes stay constant in diameter. This subset is again divided into another four subsets with respect to the diameter of 80 nm, 100 nm, 120 nm and 180 nm of the holes in the central region. To obtain the characteristics of these waveguides, the effective index of a

unit cell with the desired hole diameters is calculated using a 2D band solver in CrystalWave. The effective index then obtained is placed in the core of a continuous medium waveguide structure with the desired widths mentioned above with upper and lower claddings of air and silica. The mode solver in FimmWave is then used to calculate the effective index and group index of the mode in the waveguide. Figure 4.11 gives the plot of effective index profile versus hole diameters for different widths of the meta-waveguide of 1.732 µm, 0.866 µm and 0.433µm.

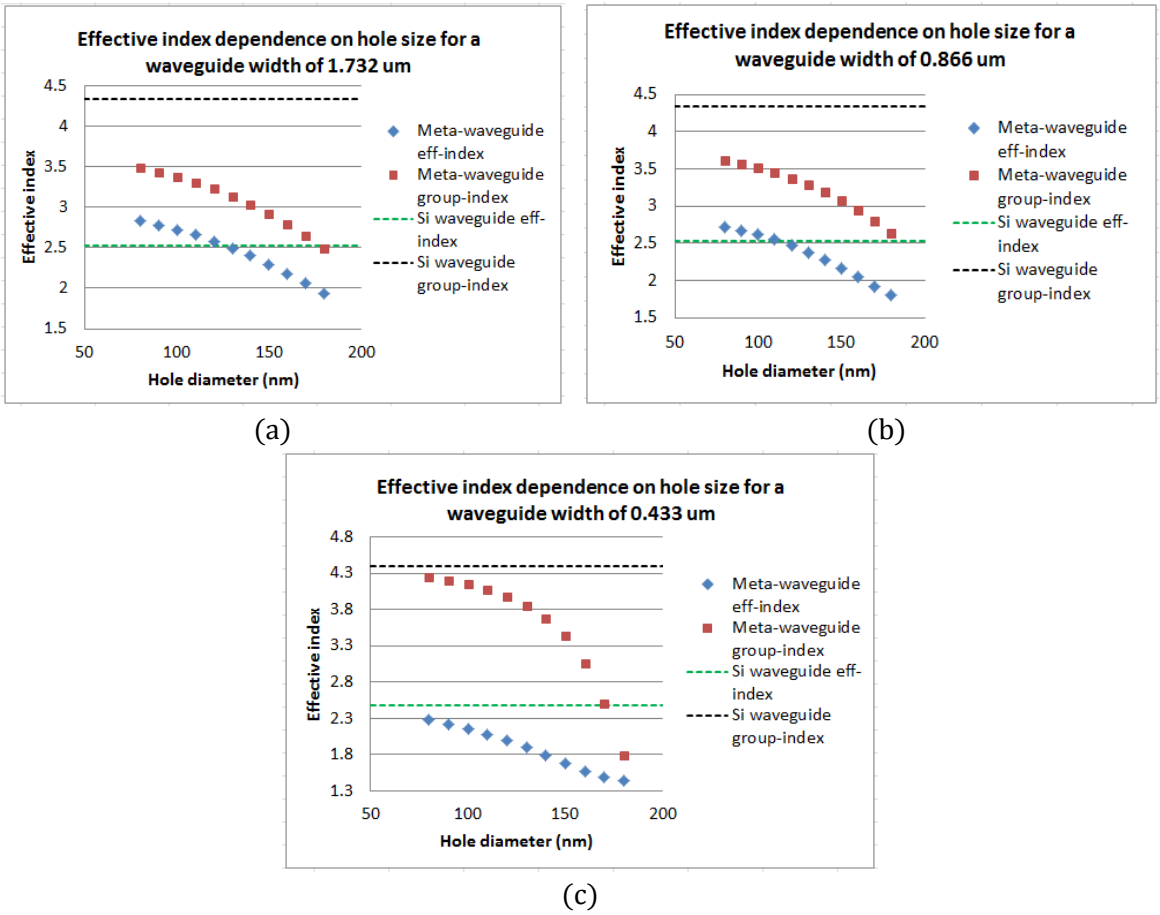

Figure 4.11 The mode effective index dependence on hole diameters for different widths of meta-waveguide; (a) waveguide width of 1.732 µm, (b) waveguide width of 0.866 µm, (c) waveguide width of 0.433µm.

The central constant hole diameter region is connected to the MMI access waveguides by an adiabatic taper consisting of the concatenation of a constant-width metamaterial linear atom diameter taper (approximately a quadratic effective index taper), in which the hole diameters are smoothly reduced to zero, and a conventional geometrical taper, in which the width of a solid silicon waveguide is smoothly reduced to the access waveguide width of 0.45 µm. Figure 4.12 shows the sections more clearly on the upper arm where the metamaterial structure is placed. The lower arm is uniform silicon with the same width and geometrical taper of the upper arm, followed by the uniform silicon with a length equal to the two linear

effective index tapers of the upper arm. Only the central constant hole diameter region is omitted.

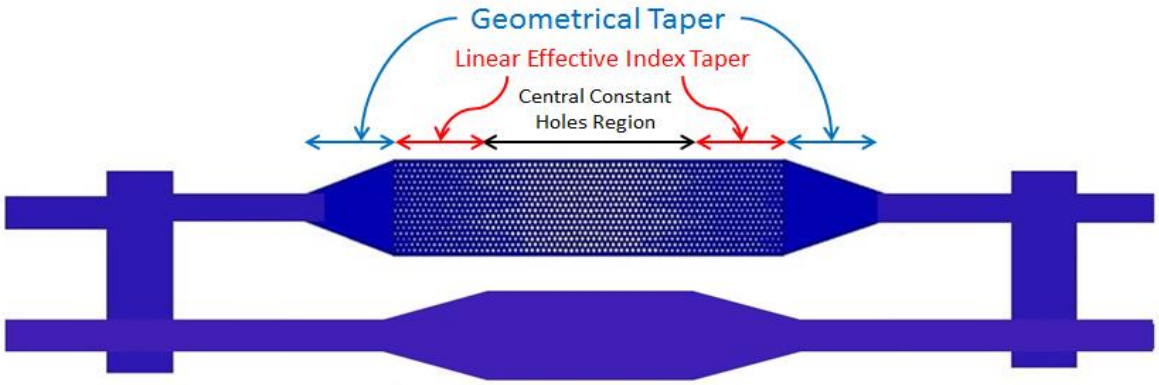

Figure 4.12 MZI test structure with metamaterial structure used on the upper arm, containing three main elements: a central constant hole diameter region, which is sandwiched between two linear atom diameter tapers, which are in turn sandwiched between two geometrical tapers. The tapers act to adiabatically adapt the mode of the metamaterial section to the mode of the conventional waveguide.

As was explained in the previous sections, FDTD simulation on a large scale graded periodic structures demands high computational resources and time which were outside the scope of the facilities available. To simplify the simulations of the complete structure, a continuous medium with the homogenised index of the periodically patterned structures may be substituted as an approximation. The homogenised index is found using the CrystalWave band solver. In sections with constant diameter holes, the homogenised index found by CrystalWave of the 2D unit cell is used globally as the core index of a continuous medium waveguide. In the taper regions where the hole diameters smoothly vary along the structure, the homogenised index of the 2D unit cell at the two ends were obtained.

Table 4.2 Specifications of the MZI structures, with different width, length and hole diameters in the central region of upper arm.

Device specifications		
Arm width (µm)	**Hole diameter (nm)**	**Length of constant central region (µm)**
1.732	180	0
	120	
	100	
0.866	180	50
	120	
	100	200
0.433	120	
	100	1000
	80	

A script written in Python provided in Appendix III automated the creation of the device. As the position of the holes along the taper determine the desired refractive indices, a raster scan

across the lattice using the Bravais vectors over an area that contains the device is performed. The script checks whether or not the lattice site visited falls within the device or not. If it falls within the device, the default atom is updated with an atom from an indexed palette. The local effective index corresponding to a unit cell composed of the indexed atom may found by the calibration process described in the preceding. The desired local effective index at the atom co-ordinate normally determines the hole diameter and hence the index by a look up process. In the case of the test structure tapers, it was found simpler and more direct to vary the hole diameters linearly between the two ends of the taper. This results in an effective index that varies approximately linearly with fill-factor and hence quadratically with respect to diameter which is close to the optimum profile of a taper and was found to work well. Figure 4.13 shows the simulations on the full MZI structures for three different arm widths in Fimmprop.

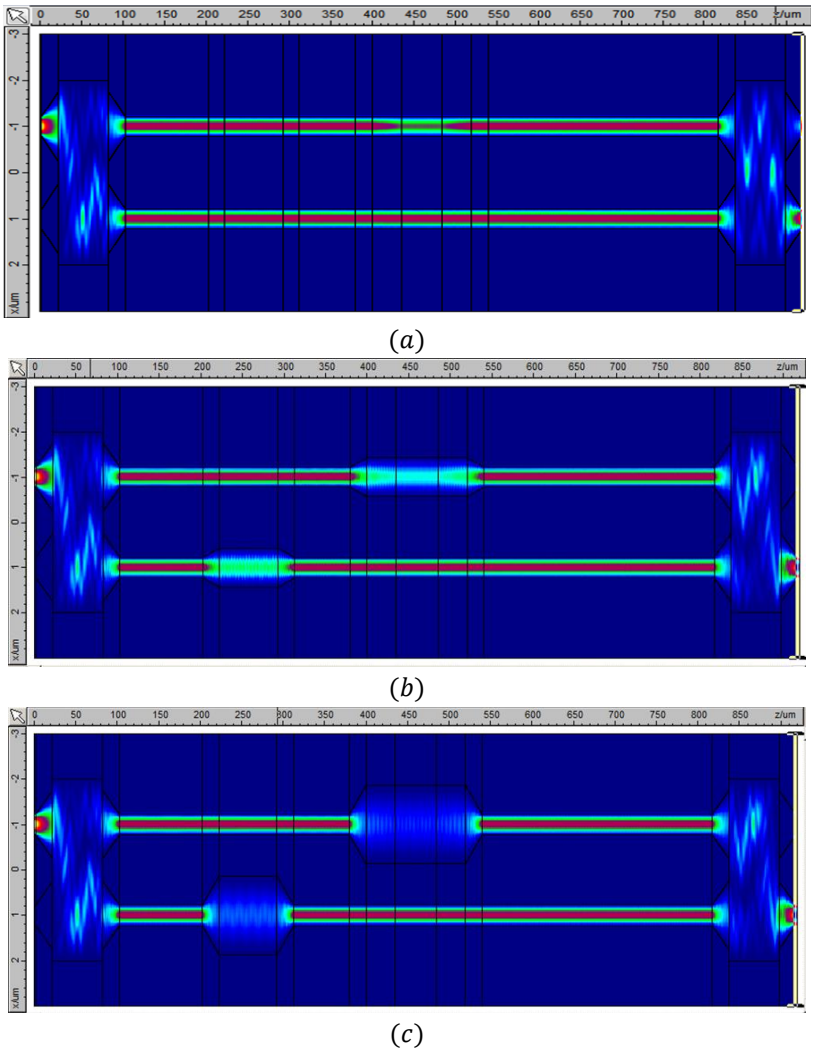

Figure 4.13 Simulations of the full MZI structures with homogenised metamaterial regions in FimmProp for a central constant 120 nm diameter hole region of length 50 µm and three different arm widths; (a) arm width of 0.433 µm, (b) arm width of 0.866 µm, (c) arm width of 1.732 µm.

In the structure with the arm width of 0.433 µm, the whole access waveguide was set to the same width, which yields an effective index of 2.47 for the fundamental Ex-like mode and 2.162 for fundamental Ey-like mode, which are far from the substrate refractive index. Table 4.2 gives the specifications of the MZI structures; in total 36 different devices. To avoid repetition, the results of simulations are given and discussed with experimental results in Chapter 5.

4.7 Mask Layout Using Pyxis

The mask layout was done using the Mentor Graphics Pyxis design tool. Pyxis has two functions; a front-end design tool which contains schematic tools to design and simulate structures, and a back-end design tool that enables the designer to implement the layout, modify it and perform physical verification such as design rule checks (DRC). The schematic and simulations in this work were all performed using the Photon Design suite, which has the facility to convert the schematic to GDSII. Consequently only the back-end design tool of Pyxis was used. The schematics used by the Photon Design suite can be converted to layout, stored as layout cells and be called by Pyxis. The Pyxis layout was fully automated using its scripting interface language, Ample, either by calling the layout cells and placing them at the targeted location or plotting the required or complementary geometries.

The mask layout was done on a $10\,mm \times 10\,mm$ design area which was cleaved perpendicular to the horizontal axis at $2.5\,mm$ in from the edges with a ±15µm error. Figure 4.14 shows the layout design area with the four triangular cleaving marks. The access waveguides were extended to the sides of the chip with a taper from a width of 0.45 µm to 0.3 µm (with an effective index of 1.89 for the fundamental Ex like mode) and of length 5 µm to the edge of the chip. The reason for using the inverse taper at the edge is to expand the mode to be a closer match to the mode of the lensed fibres used to couple light into and out of the chip.

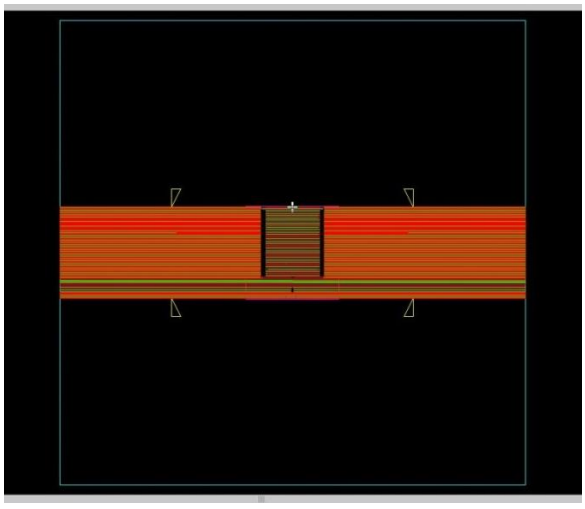

Figure 4.14 The design layout area of 10 mm × 10 mm with four triangular cleaving marks at 2.5 mm from the edges.

As the whole structure required one 300 nm etch-step only, the structures are drawn or placed on one unique layer. A 4 µm wide trench layer was drawn to isolate the structures. Figure 4.15 shows the layout of three different arms with the width of 0.433 µm, 0.866 µm and 1.732 µm, and MMI with the trench layer in green.

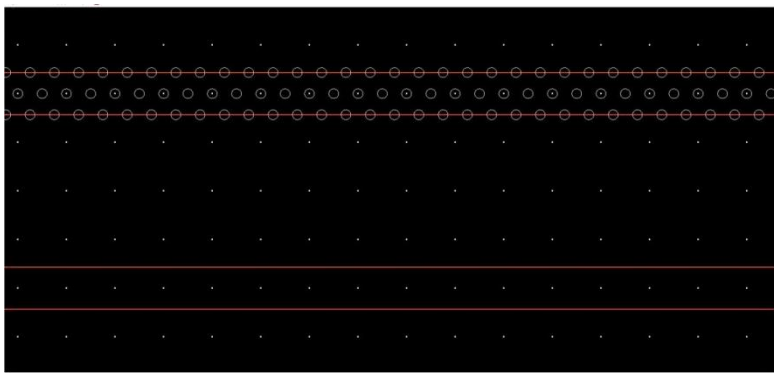

(a)

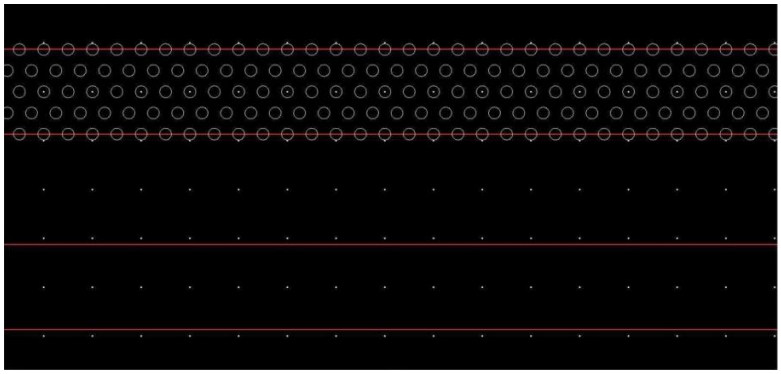

(b)

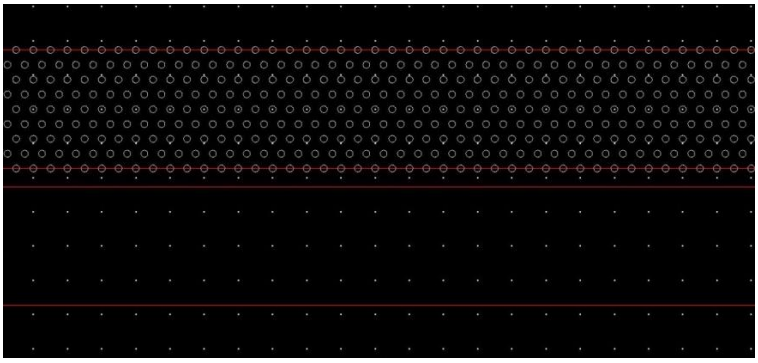

(c)

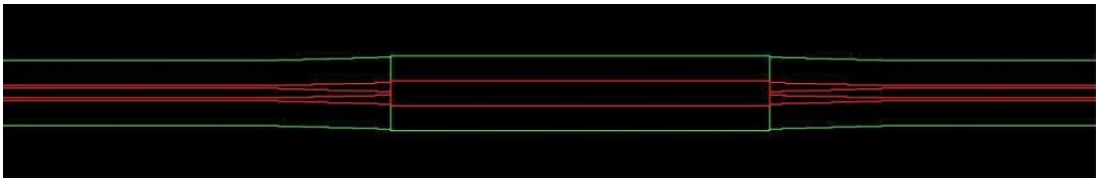

(d)

Figure 4.15 Layout of three different arms with the width of: (a) 0.433 µm, (b) 0.866 µm, (c) 1.732 µm, and (d) layout of MMI (red) and the trench (green).

The layout of the metamaterial Lüneburg lens was also drawn, by importing a GDSII file created from a schematic in Crystalwave and converted to cell layout in Pyxis. Figure 4.16 shows the central part of the lens illustrating that the diameter of the holes is increasing from centre toward the sides.

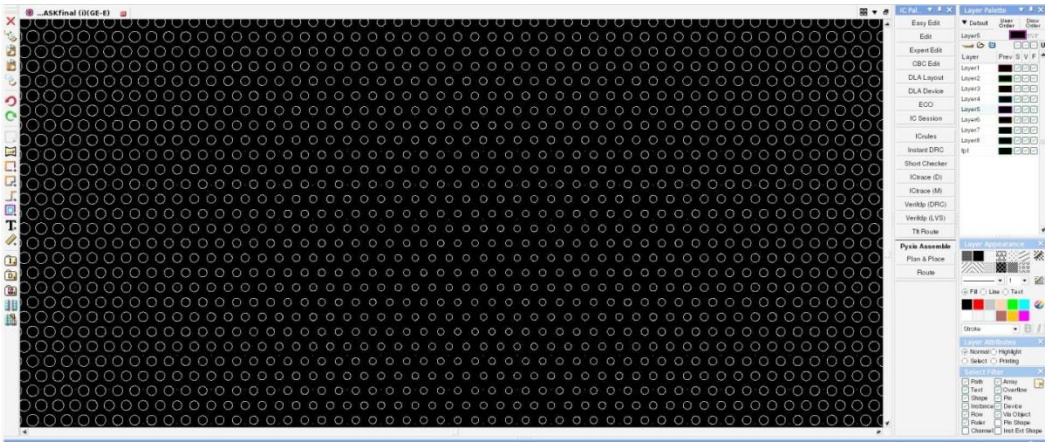

Figure 4.16 Layout of central region of the metamaterial Lüneburg lens.

4.8 Summary

In this chapter the design, verification by simulation and the layout of 2D metamaterial structures including planar metamaterial Lüneburg lenses have been discussed. The simulations of the confocal telescope lens combination with the diameter of each lens of 15 µm on a slab waveguide based on silicon with the thickness of 0.3 µm on a silica substrate showed a -0.517 dB loss on each lens. The MZI structures with metamaterial structures on one arm were introduced and the two different types of tapers needed to adapt the metamaterial section to the conventional access waveguides adiabatically, which is important to avoid the sudden change in effective index and the consequent reflection, were discussed. Three different arm widths, lengths in central region and hole diameters in the central constant region were implemented. Here the homogenisation methods explained in Chapter 2, section 2.5 were used to simplify the calculation of 3D mode effective index, which otherwise demands large computational resources, by obtaining the effective index of the Floquet-Bloch mode using the 2D band solver in CrystalWave and placing the predicted (homogenised) index in the core of a continuous medium waveguide structure used by the FimmWave mode solver to predict the waveguide mode effective index. It is clear that the use of SWG can provide more freedom to enhance the performance of the devices with improved functionalities such as reducing the footprint of MZI by using metamaterial to apply the optical path difference (OPD) rather than by using a physical length difference which may increase the dimension of the device. The mask design procedure using the Mentor Graphics Pyxis tool and the means to simplify the layout procedure using cell layouts and fully automation of drawing have been described.

The findings of this chapter are of direct relevance to Chapter 5, which follows and describes the test and measurement methodology, reports the experimental measurements of a photonic integrated circuit fabricated according to the design that has been described herein, and compares the experimental measurements with the results of simulations performed according the methodology described in this chapter.

Chapter 5. Fabricated Devices and Experimental Results

5.1 Introduction

In this chapter, the modelling and simulation studies that were explained in the previous chapter are augmented by the experimental characterisation of relevant components on a test chip specifically designed to support this research and to provide insight into improvements that might be needed in the design methodology, the theoretical modelling, simulation, and fabrication processes. The measurement techniques used to characterise the optical components and the principal tools used such as optomechanical stages; a tuneable laser and polarimeter are described. The analysis of the recorded experimental data is performed using Matlab and the results are compared with the predictions of simulations.

5.2 Contribution

The complete chapter is original work. The SEM images were provided by the CRPuO core facility.

5.3 NanoSOI Lithography Process, Fabricated Devices and SEM Images

The test chip was fabricated using the NanoSOI process through CMC Microsystems. NanoSOI is a nanomachining process for silicon-based nanostructures development on a SOI substrate [30]. The SOI wafer consists of a buried oxide thickness of 1 μm over a silicon substrate that supports a 300 nm thick silicon layer which is patterned using e-beam lithography. E-beam lithography is able to achieve a minimum feature size in the scale down to 80 nm, but as was mentioned in the NanoSOI design manual, a low throughput is expected due to the serial procedure of direct writing on the resist.

To target the adiabatic transition between the conventional waveguide and the SWG structure, the holes on the mask layout started at a diameter of 7 nm at the beginning of the patterned adiabatic waveguide taper with an initial width of 0.433 μm. In the case of SWG structure with the width of 0.866 μm, the hole diameter starts at 8.43 nm at the beginning of patterned taper, and, in the device with width of 1.732 μm, the hole diameter starts at 12.65 nm at the beginning of the taper. From the SEM images, it is clearly seen that the holes in a range of small diameters are missing on the chip as expected from the minimum feature size fabrication limit and the smallest hole that emerges has a diameter of 27 nm. Figure 5.1 shows an example of the measurement of the hole diameter using SEM micrographs of two different structures with a width of 1.732 μm and a length of the constant central region of 1000 nm with 100 nm diameter holes (left panel) and 180 nm holes (right panel). It can be observed that the perimeter of the holes are far from circular. Moreover, the diameter of the best circular fit to the perimeter differ from the target values defined on the layout.

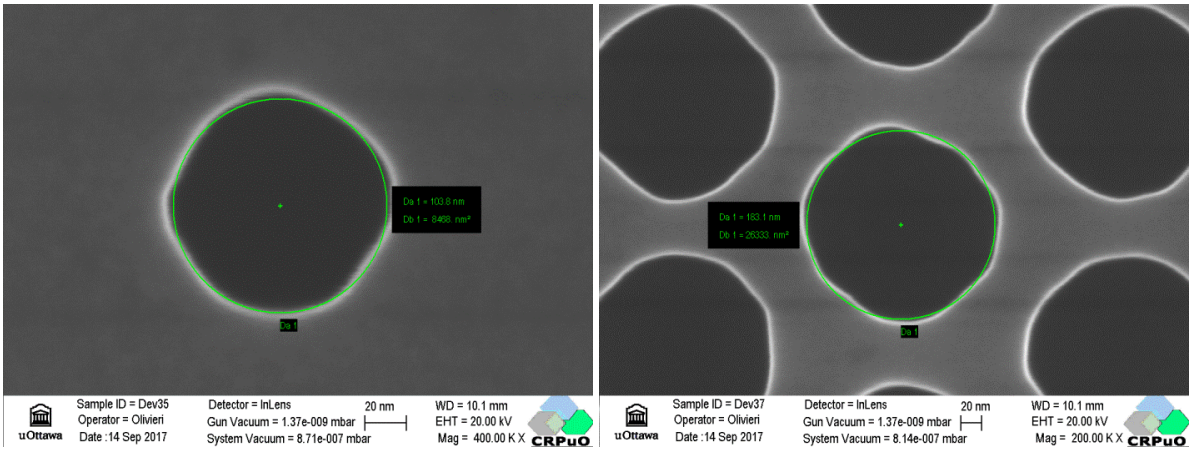

Figure 5.1 (left) the hole diameter on device with the width of 1.732 µm, central region length of 1000 µm and hole diameter of 100 nm which was measured as 103.8 µm on SEM, (right) device with the width of 1.732 µm, central region length of 1000 µm and hole diameter of 180 nm which was measured on SEM as 183.1 µm.

Table 5.1. The original diameter of holes on the mask and a comparison with the diameters on the chip and error calculations.

Diameter on the mask (nm)	Diameter on the chip (nm)	Error (%)
80	**78.23**	**2.21**
100	**102.7-103.8**	**2.7-3.8**
120	**120.8-126.3**	**0.66-5.25**
180	**182.1-183-1**	**1.16-1.72**

Table 5.1 shows the percentage error between the highest and lowest diameters measured and the target diameters on the layout. Figure 5.2 the left panel shows that the holes are missing on the SWG taper section where the target hole diameters are in the range of 37.5 nm and lower while the right panel shows that the holes with diameter of 100 nm in centre region are well defined with diameter error of 2.7%.

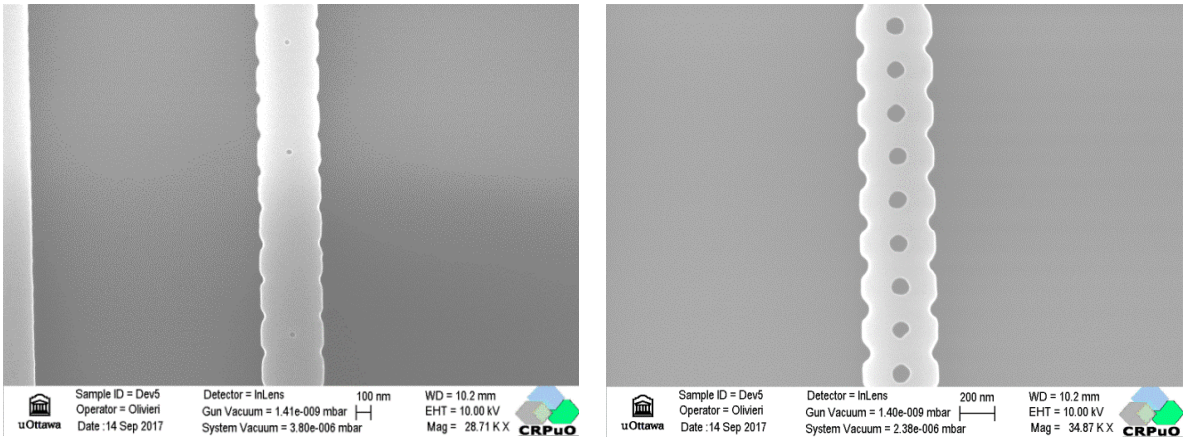

Figure 5.2 Device with the width of 0.43 µm and length of 50 µm centre region with constant hole size of 100 nm diameter (device 6), Left the smaller holes with the diameter of lower than 37 nm missing, right the constant centre region of arm with the hole diameter of 100 nm).

Figure 5.3 shows the arms of the MZI structures with the widths of 0.866 µm (left panel) and 1.732 µm (right panel). Figure 5.4 shows the arms of the MZI structures with the width of 1.732 µm in the constant centre region with a hole diameter of 120 nm. The width of the patterned waveguide measured is 1.717 µm and the width of the conventional waveguide on the arm measured is 1.795 µm. This difference in width creates an additional imbalance of the MZI.

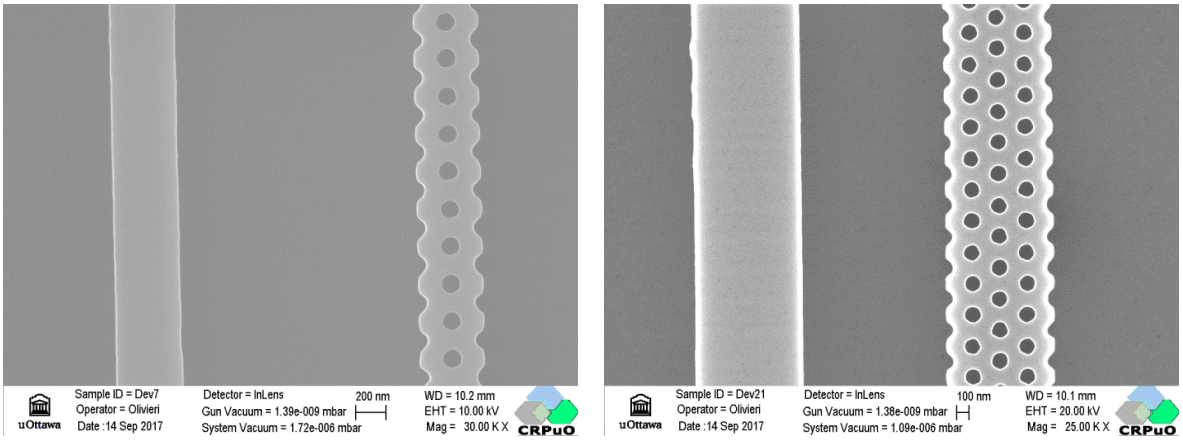

Figure 5.3 (Left) MZI device arms with 0.433 µm width and 50 µm length at the centre region with a constant hole diameter of 120 nm. (Right) MZI device arms with the width of 0.866 µm and length of 200 µm with a hole diameter of 120 nm in the constant hole diameter centre region.

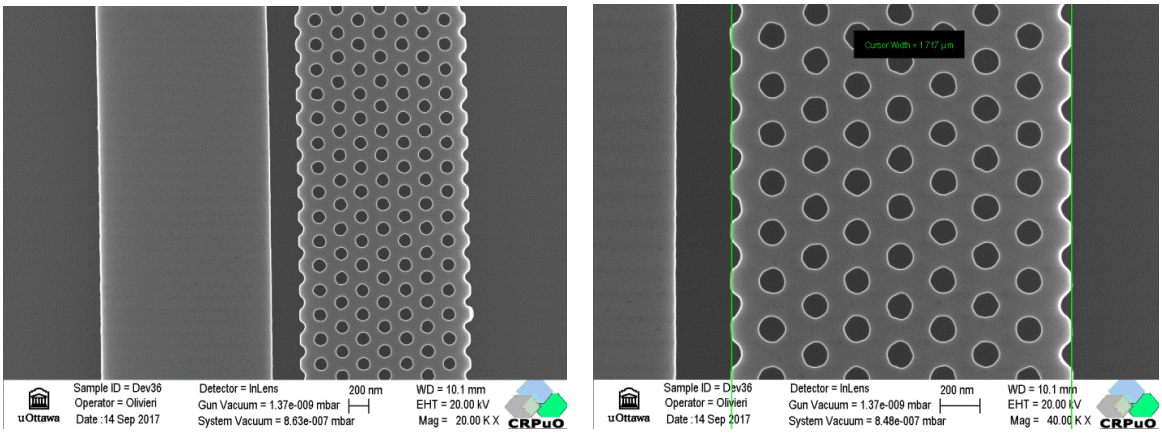

Figure 5.4 Arms of a MZI device with width of 1.732 µm and a length of 100 µm with a hole diameter of 120 nm in the constant centre region.

Table 5.2 The MMI dimensions on the mask and on the fabricated chip and fabrication errors.

MMI	On the mask (µm)	On the chip (µm)	Error (%)
Length	60.734	60.4	0.54
Width	4	4.01	0.25
Taper wide width	1.5	1.494	0.4
Waveguide width	0.45	0.446	0.88
Waveguide height	0.3	-	-

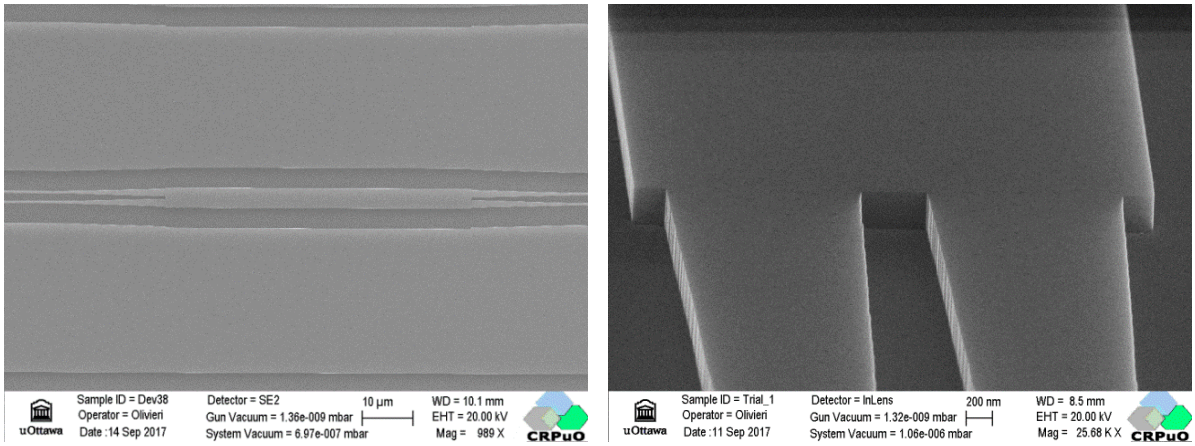

Figure 5.5 SEM of MMI structure on the chip, (left) top view MMI, (right) angled view of the taper section on MMI's ports.

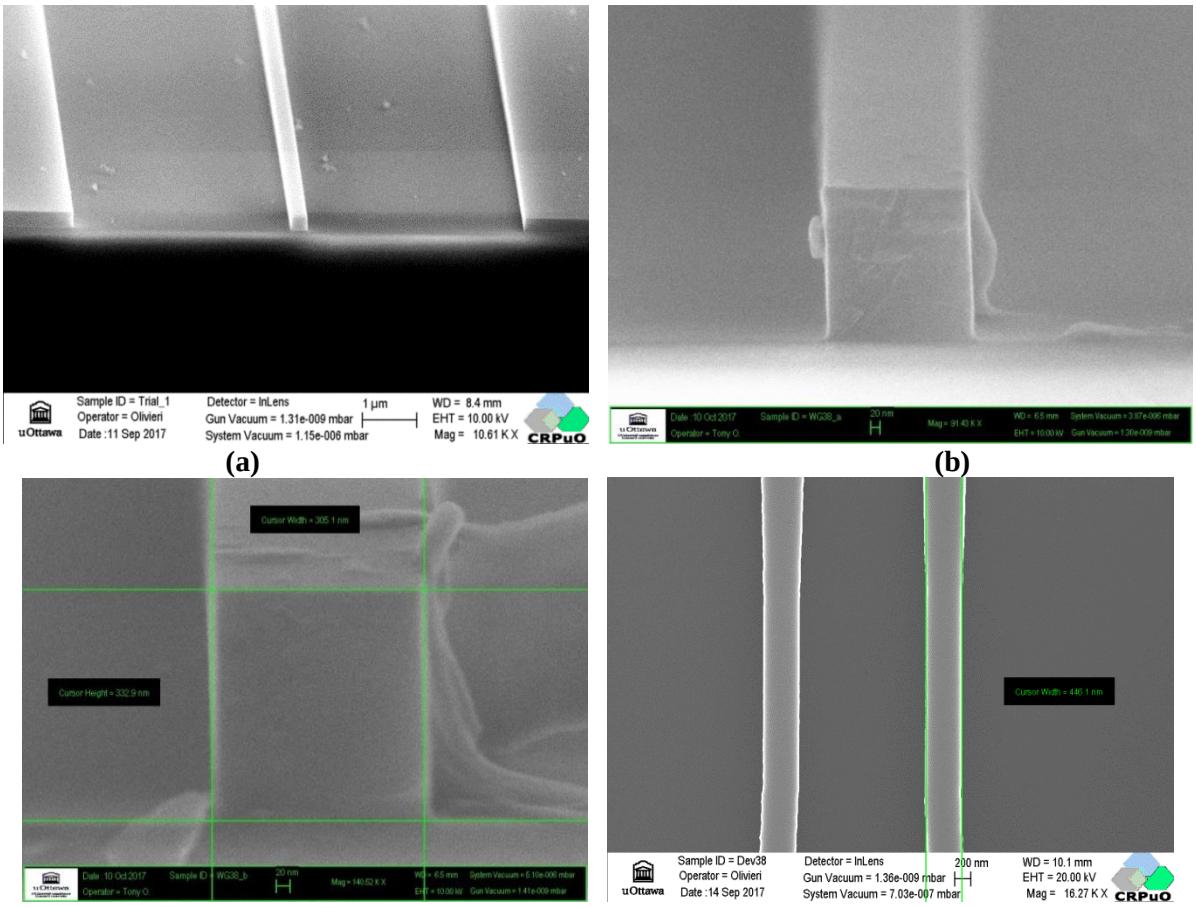

Figure 5.6 SEM of inversed taper waveguide at the edge of the chip. (a) wide view of the waveguide and the trench of 4 µm width on each side; (b) closer view of the waveguide at the edge and the observed roughness on the wall of the waveguide; (c) the measurement on the width and height of the taper waveguide at the edge; (d) the parallel waveguide connecting the back to back MMIs.

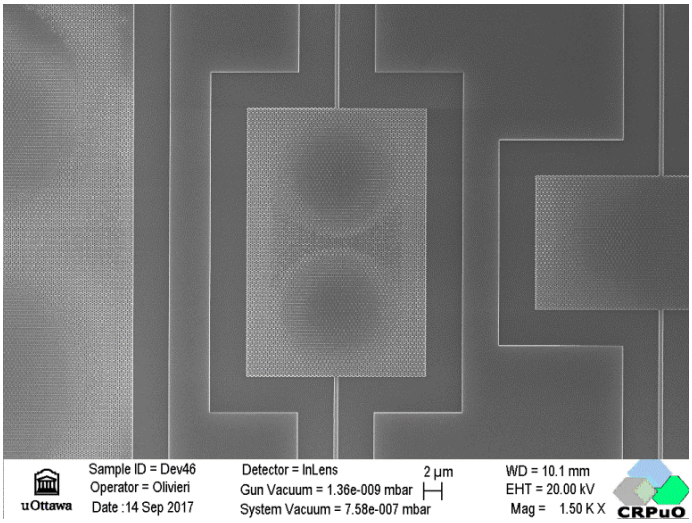

Figure 5.7 SEM micrograph of telescope composed of two lenses each with the diameter of 15 µm

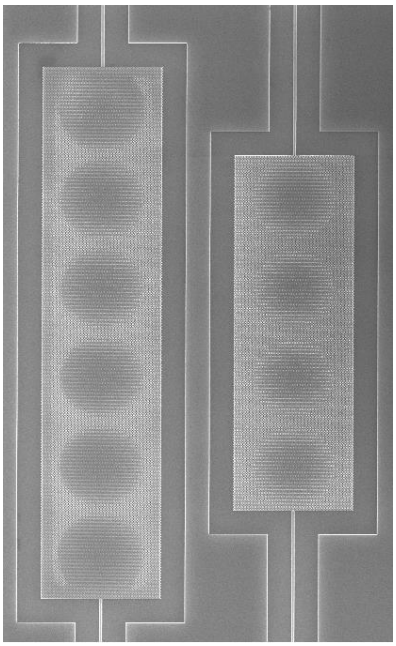

Figure 5.8 SEM micrograph of two telescope structures composed of four and six lenses, respectively, with each lens having a diameter of 15 µm.

The SEM of the MMI on the chip is shown in Figure 5.5. The measurements of the dimensions of the MMI and the calculated errors with respect to the mask layout dimensions are given in Table 5.2. The height of waveguide could not be measured confidently as the tip of AFM had an angle and caused uncertain measurement.

Figure 5.6 shows the waveguide at the edge of the chip where a reverse taper of 300 nm height and 300 nm width was used. The SEM measurement on the width of the waveguide at the edge was 305.1 nm with the error of 1.7% and the height of 332.9 nm with the error of 10.96%. It may be observed in Figure 5.6 that the waveguide and trench sidewalls are rough

and deviated markedly from the straight lines defined by the layout (Figure 5.6 (d)), which may cause the phase bias offset as mentioned in section 4.5

Figure 5.7 shows a SEM micrograph of telescope composed of two metamaterial lenses each with a diameter of 15 µm surrounded by trench of 4 µm width and connected to single mode access waveguides of 0.45 µm width. The air holes are changing in diameter from the rim towards the centre of the lens.

Figure 5.8 shows an SEM of two telescope structures of composed of four and six lenses respectively, with each lens having a diameter of 15 µm surrounded by trench of 4 µm width and connected to single mode access waveguides of 0.45 µm width.

5.4 Experimental Setup

Two main instruments were used in the measurement setup; a tunable laser and an optical component analyzer. The tunable laser was an Agilent 81680A with the wavelength range of 1460 nm to 1580 nm, maximum output power of 6 dBm, and wavelength accuracy of ±0.01 nm. The optical component analyzer was an Agilent N7788B with a polarimeter receiver which enables measurement of the transmission of the Ex and Ey polarisation of the device under test. A sweep rate of 0.5 nm/s was used for these measurements. The setup is shown in Figure 5.9. The devices are connected via optical fibres and the operation of the tunable laser and optical component analyzer are automated using polarization navigator software on the PC to facilitate the adjustment of the measurement options and collect the measured data. Lensed optical fibres were used to edge couple the optical field to the input/output of the sample chip.

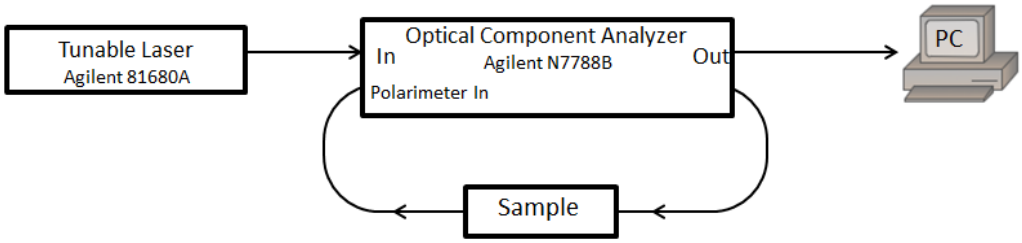

Figure 5.9 Measurement setup, consisting of a tunable laser and optical component analyzer that are connected through optical fibres, and are controlled by polarization navigator software on a PC.

The lensed fibres and waveguides of the sample were aligned using six axes positioning stage shown in Figure 5.10.

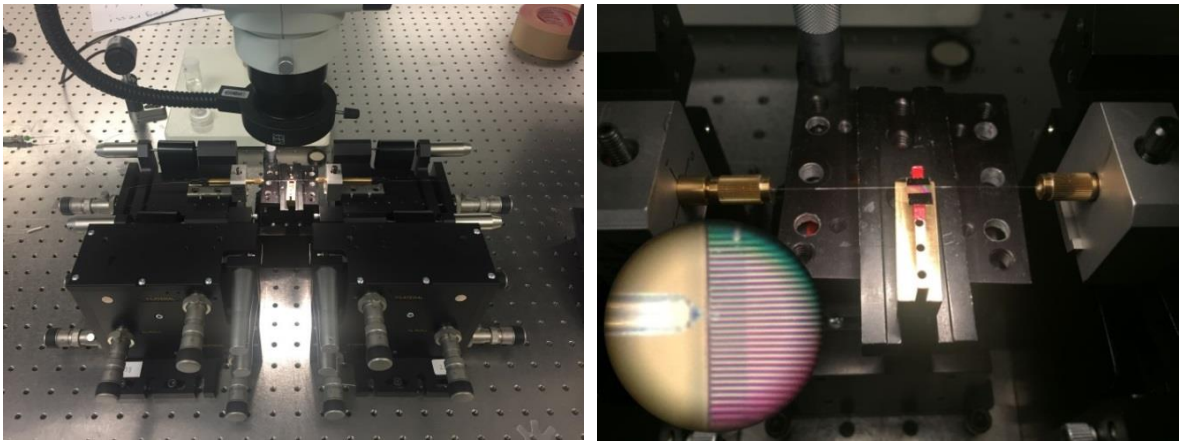

Figure 5.10 The sample was held and aligned with lensed fibres using a six axes positioning stage (left). (Right) Lensed fibres were used for input and output edge coupling to the chip. The insert shows a magnification of the lensed waveguide and the waveguides of the chip as observed by a microscope.

5.5 Experimental Analysis

The analysis of the data obtained in the measurement is performed using Matlab scripts and Excel spreadsheets. The experimental spectral data displays Fabry-Perot fringes with small period that modulate the envelope of desired data. This effect arises from the long cavity that is formed by the two edge facets of the SOI waveguide at the ends of the chip. The analysis of these Fabry-Perot fringes permits one to obtain the loss of the waveguides.

The expected spectral period $\Delta\lambda_{\mathrm{FP}}$ of the Fabry-Perot fringes is found to be $\Delta\lambda_{\mathrm{FP}} = 0.053$ nm using the free spectral range (FSR) relation:

$$\Delta\lambda_{FP} = \frac{\lambda^2}{2n_g L} \tag{5.1}$$

where λ is the operating vacuum wavelength, n_g is the average group index of the structure, which is taken to be dominated by the long straight waveguides, and L is the end-to-end length of the chip.

Using the method in Qi [31], the attenuation coefficient along the waveguide with the width of 0.45 µm was obtained as 6.94 dB/5mm and along the waveguide with the width of 0.433 µm as 7.94 dB/5mm with the edge coupling loss of 4 dB/coupling. More details on the calculations are provided in Appendix I.

Using the linear relation obtained from the total loss on the two, four and six lens structures (Figure 5.11), the intercept predicts the loss of the waveguide with no lens present to be 25.9 dB.

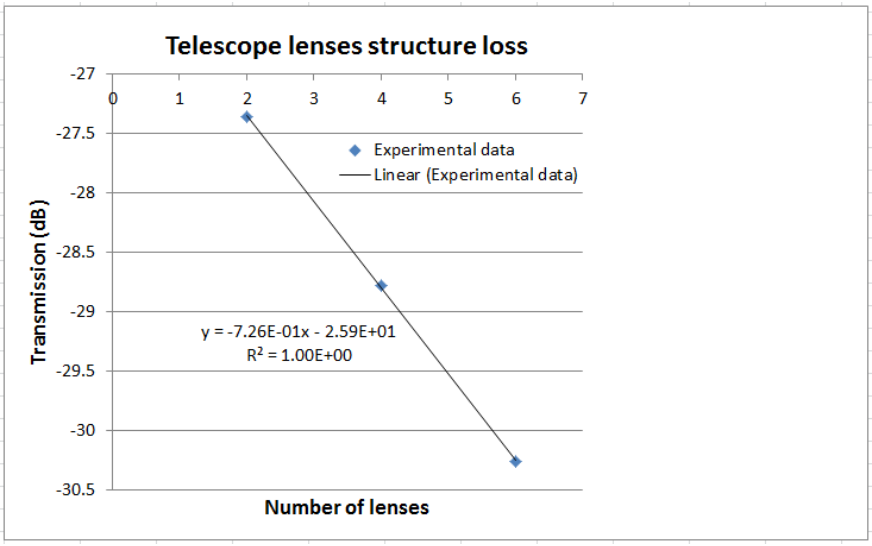

Figure 5.11 Linear relation of the loss of the telescope system of two, four and six lenses.

From the preceding analysis of the Fabry-Perot fringes given by a straight test waveguide, the loss of the waveguide is 6.94 dB/5mm, and the total loss measured on this device was17.97 dB, so the butt-coupling loss between fibre and the waveguide on each end is found to be 5.517 dB, which is close to the value found for the straight test waveguide. The slight difference could be due to a defect at the facet. The total loss due to the interface between lens and access waveguide then is calculated as $(25.9 - 17.97)/2 = 3.965\text{dB}$. This loss may be reduced by using an adiabatic lateral taper and/or adiabatic effective index transition between the conventional waveguide and the metamaterial slab waveguide of the lens. The slope of the plot gives the loss per lens without any other considerations of other losses and is found to be 0.726 dB/ lens which is close to the prediction of the simulation presented in Chapter 4.

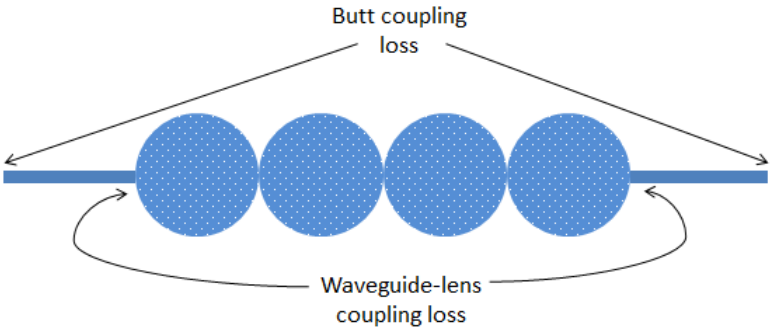

Figure 5.12 A four lens telescope system illustrating the definition of the butt-coupling loss and the waveguide to lens coupling loss.

As was discussed in the previous chapter, the OPD created by the change in effective index of the upper arm of a MZI due to the presence of the metamaterial structure, results in MZI fringes with a different spectral period from structure to structure. The period depends upon the hole diameters in the constant central region and the length of this region, which

parameterise the difference between the group index of the two arms. The analysis of the measured data provided by the structure with an arm width of 1.732 µm and the hole diameter of 180 nm with the length of 200 µm in the constant hole diameter region, is given in detail herein to illustrate the methodology but to avoid repetition the detailed analysis of all the other structures is relegated to Appendix I.

A segment of the measured transmission spectrum of a MZI test structure is plotted as black points in Figure 5.13. Very fine Fabry-Perot fringes due to facet reflections can be seen superimposed on broader MZI fringes due to the OPL imbalance of the arms of the MZI. A simulation of the experiment without the end-facet reflections is shown as the solid red curve. Good agreement between the simulation and experimental data set can be observed.

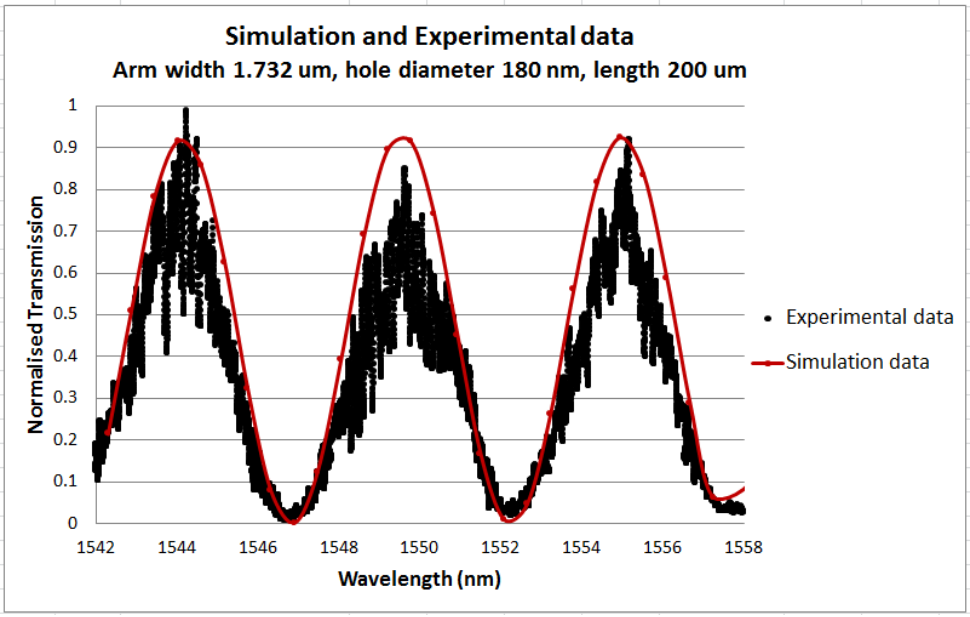

Figure 5.13 Comparison of simulation of experiment data and the measured experimental data of the device with the arm width of 1.732 µm with the central region length of 200 µm and constant hole diameter of 180 nm. The fit shows the good agreement between the two data sets.

Since the long period spectral fringes of the MZI within the measured experimental data are contaminated by the short period Fabry-Perot fringes, the Matlab Fourier curve fitting tool is used to extract the period or FSR of the MZI fringes. This tool finds the best fit to the data by a Fourier series truncated at a specified highest order in the form of a linear combination of sin and cos functions:

$$f(x) = a_0 + a_1\cos(xw) + b_1\sin(xw) + a_2\cos(2xw) + b_2\sin(2xw) + \cdots \qquad (5.2)$$

where x is normalized by a specific mean that regularly is the centre wavelength and a standard deviation. The Fourier curve fit of the corresponding fringes are shown by the solid blue line in figure 5.14.

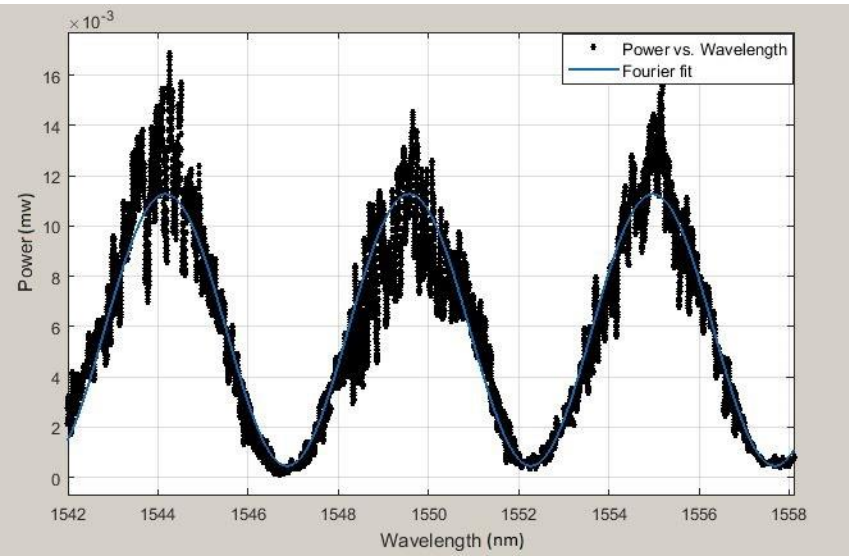

Figure 5.14 The fit by the Fourier curve function (blue) to the measured experimental data (black) of the MZI device with the arm width of 1.732 μm with the central region length of 200 μm and constant hole diameter of 180 nm.

The inverse spectral period 1/T is found from the parameter w provided by the Fourier curve fitting tool given the order of the dominant Fourier coefficient O and the standard deviation σ used by the tool to normalise the data:

$$\frac{1}{T} = \frac{O \times w}{\sigma \times 2\pi} \tag{5.3}$$

A plot of the extracted inverse period versus the length of the constant hole section on the arm should be a straight line with a slope equal to the difference in group index between the two arms in a set of MZI structures with the same hole diameters and waveguide widths according to the FSR relation (discussed in more detail in Appendix II).

$$\Delta\lambda = \frac{\lambda^2}{\Delta n_g L} \tag{5.4}$$

A plot of the inverse period extracted from simulation data versus the length of a set of MZI devices with an arm width of 1.732 μm and the hole diameter of 180 nm in the constant hole diameter centre region is shown in Figure 5.15. It is observed that the fit by a straight line to the extracted data is excellent.

The linear trend line of an Excel plot may be used to obtain the slope of the plot of the inverse spectral period versus central region length plot. The equation for the FSR can be rewritten as:

$$\frac{1}{\Delta\lambda} = \frac{\Delta n_g L}{\lambda^2} \tag{5.5}$$

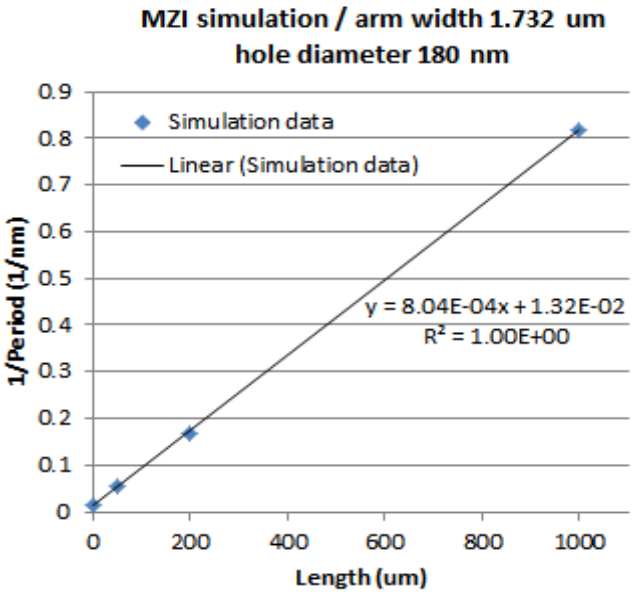

Figure 5.15 The linear relation between the inverse period extracted from simulation data and the central region length of a set of MZI devices with an arm width of 1.732 μm and constant hole diameter of 180 nm with the different central region lengths of 0 μm, 50 μm, 200 μm and 1000 μm.

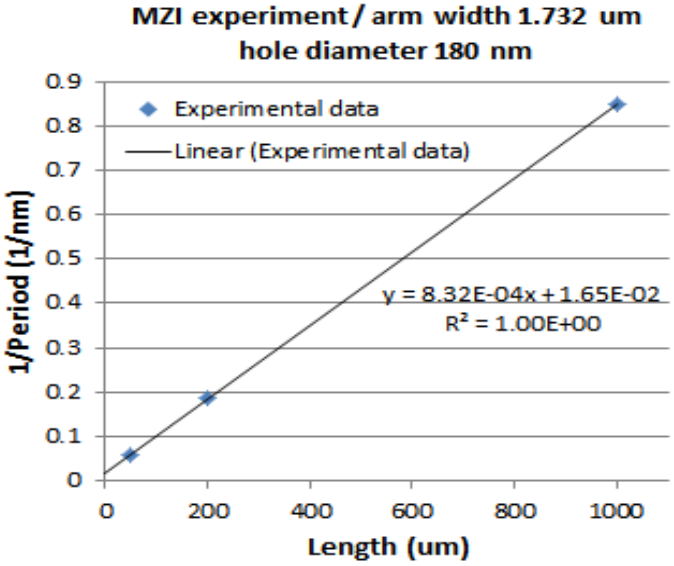

Figure 5.16. The linear relation between the inverse period extracted from measured experimental data and the central region length of a set of MZI devices with an arm width of 1.732 μm and a hole diameter of 180 nm in the constant hole diameter central region with central region lengths of 0 μm, 50 μm, 200 μm and 1000 μm.

The units used in the plots are 1/period (1/nm) versus length (μm). Hence, the slope of the plot is $\Delta n_g/\lambda^2 = 1/L\Delta\lambda$ and $\Delta n_g = \lambda^2 \times \text{slope}$. The unit of slope is obtained from $1/L\Delta\lambda$ which is $1/(\mu m \times nm)$ and for $\Delta n_g = \lambda^2 \times \text{slope}$ the unit is $\mu m^2 \times 1/(\mu m \times nm) = 10^3$.

The slope of the simulation data was obtained as 8.04×10^{-4} which converts to $8.04 \times 10^{-4} \times 10^{3} = 0.804$ which implies $\Delta n_g = (1.55)^2 \times 0.804 = 1.931$.

Following the same process but using parameters extracted from the measured experimental data as shown in Fig. 5.16, a slope of 0.832 is found which corresponds to $\Delta n_g = (1.55)^2 \times 0.832 = 1.998$ in good agreement with the simulated experiment. It is observed that the fit by a straight line for measured experimental data is again excellent.

To obtain a theoretical prediction of Δn_g, first CrystalWave was used to find the homogenised index for the core and then the mode solver of the Fimmwave was used to calculate the mode group index of the resulting continuous medium waveguide for the middle part of the upper arm with the constant hole diameter and the lower waveguide of pure silicon core.

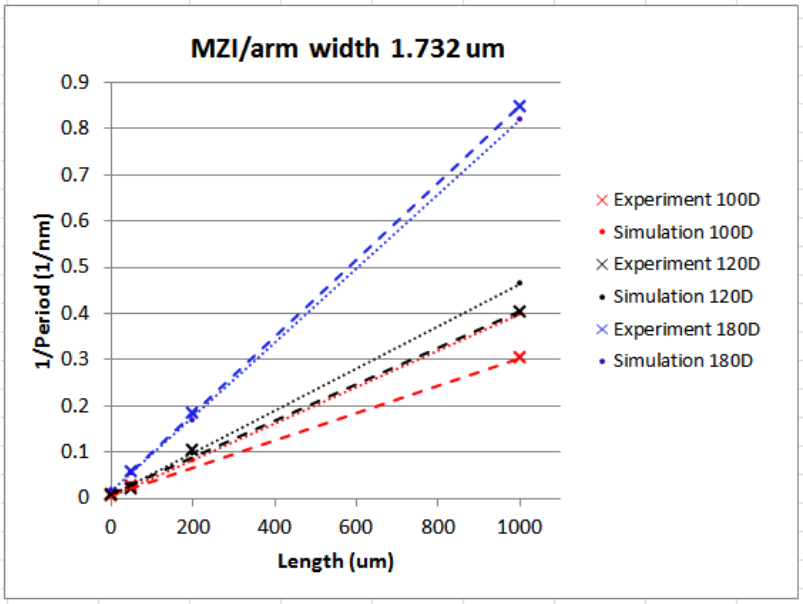

Figure 5.17 A comparison in the linear relation of the simulation and experimental data obtained from the plot of inverse period versus the length of the devices with the arm width of 1.732 µm and constant hole diameter of 100 nm, 120 nm and 180 nm with the different central region lengths of 0 µm, 50 µm, 200 µm and 1000 µm.

Following this method the group index of a 1.732 µm wide arm with 180 nm diameter holes is found to be 2.494, and the group index of the 0.45 µm wide silicon waveguide is found to be 4.330. This predicts a group index difference $\Delta n_g = 4.330 - 2.494 = 1.835$ which is within 3.72% the prediction of the simulation of the experiment. The difference between the prediction of theory and the value obtained from measured experimental data is larger at 5.47%. The difference between the theory and the simulation of the experiment may be due to the error in the curve fitting analysis which is very tricky when a limited number of data points must be considered due to the high memory demands of simulation tools and the

limitations of computer resources. The difference between the simulation of experiment and the measured experiment is most like due to the fabrication error and the curve fit error.

Figure 5.17 shows a good agreement between the experimental and simulation plots for the structure with a 1.732 µm wide arm with different lengths and constant hole diameters of 100 nm, 120 nm and 180 nm. The detailed calculation on the devices are given in Appendix I. In case of the structure with the hole diameter of 100 nm, the error between the experiment and simulation is higher as was expected, due to the minimum feature size limitation of the fabrication.

Table 5.3 provides a summary of the results obtained for the different structures (the detailed calculations are given in Appendix I).

Table 5.3 The theoretical, simulation and experimental results on Δn_gobtained on the structures with three different arm width and different hole diameters.

Device specifications		**Δn_g**		
Arm width (µm)	**Hole diameter (nm)**	**Theory**	**Simulation**	**Experiment**
1.732	180	1.835	1.931	1.998
	120	1.104	1.088	0.951
	100	0.953	0.946	0.713
0.866	180	1.704	1.729	1.864
	120	0.961	0.855	0.816
	100	0.816	0.812	0.744
0.433	120	0.419	0.430	0.840
	100	0.251	0.254	0.413
	80	0.152	0.151	0.209

Figure 5.18 shows a comparison of the Δn_g obtained from experiment, simulation and theory with respect to the hole diameters. It shows that the prediction by simulation and the approximation of the theory work well. These plots show a good agreement between the theory and simulation and experiments in the devices with the arm width of 1.732 µm and 0.866 µm. The error increases in the devices with the arm width of 0.433 µm as was expected due to the minimum feature size limit in fabrication, the error in curve fitting due to the large period of the fringes and more loss on the thinner waveguide of 0.43 µm which made the data hardly readable.

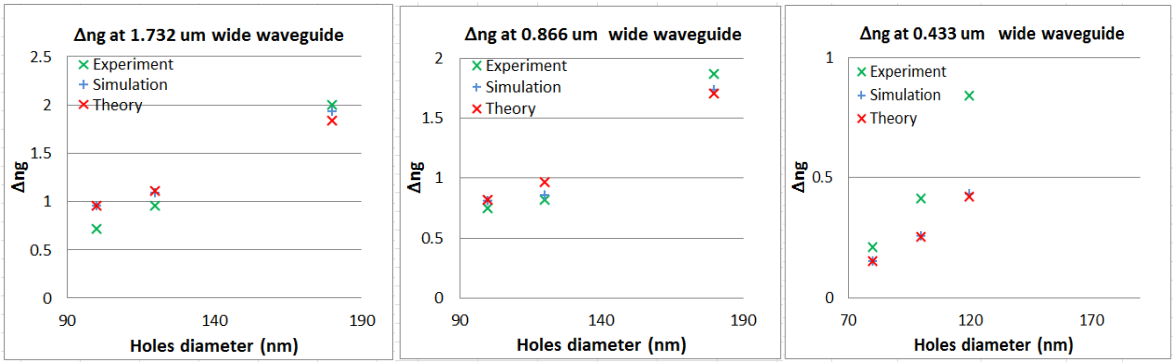

Figure 5.18 A comparison between the Δn_g obtained from experiment, simulation and theory with respect to the hole diameters in the three structures with the arm width of 1.732 µm, 0.866 µm and 0.433 µm.

5.6 Summary

This chapter has described the experimental and data analysis methods used to characterise the fabricated test structures. The topography of the fabricated devices on the chip was verified using SEM micrographs and the fabrication errors were quantified. The deviation of the diameter of the holes from the value defined on the layout varied from 0.66 % to 5.25 % in addition to the distorted circular holes. The waveguide and trench sidewalls was rough and deviated markedly from the straight lines defined by the layout, which might cause the phase change in MZI structure as was mentioned. In some sections the access waveguides were damaged preventing measurements to be performed on a number of devices.

The experimental set up, its components, the measurement procedure and method of experimental analysis have been described. Using the Fabry-Perot effect, the attenuation coefficient along the waveguide with the width of 0.45 µm was found to be -6.94 dB/5 mm and along the waveguide with the width of 0.433 µm obtained as -7.94 dB/5 mm and the edge coupling loss of 4 dB/coupling to a waveguide with the width of 0.3 um. The loss of each interface between lens and access waveguide was 3.965 dB. This loss may be reduced by adiabatic lateral taper and/or adiabatic effective index transition between the conventional waveguide and the metamaterial slab waveguide of the lens. The loss per lens was found to be 0.726 dB which close to the value predicted by FDTD simulation.

In the case of the differential group index of the MZI devices, good agreement was obtained between the predictions by theory, simulation of experiment and experimental measurement on the structures with three different arm widths and different hole diameters in the central region. The observed errors were expected due to the limit in minimum feature size of the fabrication, fabrication errors, curve fitting errors and defects on the fabricated devices. The homogenisation of these structures turns out to be accurate despite operation in the only just subwavelength regime. The results obtained show the accuracy of theoretical methods explained in Chapter 4.

Chapter 6. Conclusions

6.1 Summary & Conclusions

The optical communication sector have embraced silicon as the material platform of choice to decrease component footprint, energy consumption, and to reduce cost by leveraging the vast investment of the electronics industry in silicon microfabrication and the consequent maturity of the fabrication processes. The major challenge confronting a designer of a photonic integrated circuit is the low density of integration currently possible and a device library that is far from complete. These challenges stem from the difficulty of confining light below the scale of its wavelength. It has been argued in this thesis that the precise control of light in photonic integrated circuits is on the verge of a breakthrough driven by two recent developments in the field: transformation optics, which enables the material parameters needed to support a target desired optical field to be found, and homogenisation, which enables the constituent elements of a metamaterial to be specified such that its continuous medium equivalent possesses any desired optical property. The replacement for the purpose of analysis of a metamaterial meeting current constraints of volume fabrication process with a continuous medium with a refractive index given locally by the homogenised index of a perfectly periodic structure with local values of the structural parameters has been found to be a good design rule, despite the use of continuous media boundary conditions. Continuing advances in nanolithography that offer prospects of volume manufacture such as nanoimprinting and mask-less optical lithography [32] augur well that the impact of metamaterials on photonic integrated circuit technology will be as profound as the impact of quantum wells has been to semiconductor optoelectronic technology.

This thesis concentrates on structure-property relations of key PLC components and the metamaterial engineering of these properties which has important application to the next generation of coherent photonic systems. New design procedures of practical utility founded on the fundamental physics of metamaterials have been presented in addition to the identification of opportunities for break-through integrated photonic devices that metamaterial engineering has to offer. The fundamentals and the importance of first homogenisation was introduced to set a context of continuous media as a useful approximation to materials composed of atomic particles as a prelude to the more complex homogenisation of metamaterials in the following chapters. In Chapter 2, metamaterials are introduced as a means to refine the optical properties of devices. The homogenisation methods for 1D and 2D lattice metamaterial structures were described and found to provide a usefully accurate description of the properties of metamaterial waveguide components. To address an artifact observed as the consequence of a bandgap at operating wavelength for on-axis propagation in a metamaterial, a self-consistent waveguide confinement correction of the dispersion relation was introduced. In Chapter 3, the 1D lattice metamaterials structures were discussed along with their local anisotropic behaviour in the deep subwavelength regime. To reduce the modal phase error which is essential for perfect imaging in key

component devices such as MMI, the modification of the dispersion relation was addressed using subwavelength engineering of a longitudinal metamaterial structure. In such these structures, spatial and temporal dispersion must be taken into account when meeting current fabrication constraints. Subwavelength dispersion engineering can help by modifying the dispersion relation to extend the accuracy of the paraxial approximation to the metaxial regime. On the basis of the simulations and findings on modal phase error correction, a novel MMI based silicon integrated polarisation beam splitter using a longitudinal metamaterial structure was proposed for the first time, and the importance of the adiabatic structures to adapt geometry and homogenised index of metamaterial structure to the conventional structures to avoid abrupt junctions was explained.

The 2D lattice metamaterial was introduced in Chapter 4 and the implementation of the devices such as planar metamaterial Lüneburg lens, MZI test structures with metamaterial structure on one arm and metamaterial adiabatic structures were proposed and validated by simulation. A confocal telescope consisting a combination of an even number of planar metamaterial Lüneburg lens was proposed as a useful test-structure and verified by simulation. The simulations using Photon Design tools; mask layout procedure using Mentor Graphic tools; and the automation using the interface scripts were described. In Chapter 5, the fabricated structures were verified under SEM images, and the experimental set up was explained. The data analysis methods used to process the raw measurement data in order to characterise the fabricated test structures was described. Using the Fabry-Perot effect, the attenuation coefficient along the waveguides was calculated. Good agreement was obtained between the predictions by theory, simulation of experiment and experimental measurement on the differential group index of the MZI devices in the structures with three different arm widths and different hole diameters in the central region. The obtained results confirm the accuracy of theoretical methods explained in the Chapter 4.

6.2 Discussion & Suggestions for Further Work

Advancements in nanofabrication processes and metamaterial design methodology are converging to create a new component capability that may herald a paradigm-shifting breakthrough in photonic integrated circuit technology. Significant contributions have been made in this thesis to the advancement of the modelling and design of metamaterial based components but there remain many open questions that merit further research. Some suggestions for future work are offered below.

1. The most popular Si-photonics material platform is silicon-on-insulator. The silicon layer thickness is typically chosen to be 220 nm; a *de facto* microelectronics industry standard. However, it is not clear that this thickness is the best choice for photonics. An initial design of the longitudinal MMI structure targeting a 220 nm SOI wafer and a fabrication process with a 100 nm minimum feature size was found to be overly constrained. It was challenging to design a multi-waveguide array with 100 nm slots with sufficiently narrow width waveguides to ensure the strong coupling required for a short device length.

Ensuring that the fundamental mode remained bound as it traversed the adiabatic transition taper between the access waveguide and the multimode region of the MMI was found to be an even more delicate design issue. It was very clear that higher aspect ratio structures significantly ease the design problem by increasing the confinement in the direction normal to the wafer while still permitting longer range lateral interaction across the SWG. There is strong evidence that a thicker silicon layer is beneficial to Si-photonics components in general and is not specific to the longitudinal MMI structure [33]. SOI wafers with a silicon layer thickness from 100 nm to 500 nm are available commercially. A thickness of 350 nm was selected for the longitudinal MMI structure designed and simulated in this thesis as a compromise. The silicon layer thickness 'sweet spot' for photonic components merits further investigation.

2. It was found in this thesis that a 1D transverse metamaterial is effective in controlling temporal dispersion which increases the bandwidth of an MMI. The anisotropy introduced by the 1D transverse structure is effective at reducing the device length but the orientation of the index ellipsoid is not helpful in respect of modal phase error. The 1D longitudinal metamaterial is effective in controlling spatial dispersion which reduces modal phase error. However, the anisotropy introduced by the 1D longitudinal structure increases the device length. These findings suggest that a combination of transverse and longitudinal patterning (i.e. a 2D metamaterial MMI) may offer a route to a compact, broadband, low modal phase error MMI. It is a challenge to formulate a systematic procedure to design a 2D structure to specified optical properties. This has led to some researchers resorting to warehouse scale computers to run FDTD simulations of a pixelated 2D slab combined with a search algorithm to find a configuration of pixels that meets the desired component specification [34] sometimes with record breaking results [35]. The structures that emerge resemble computer generated holograms (CGH) (also known as a metasurface) but unlike a CGH, which diffract light incident normal to the plane of the hologram admitting a tractable theoretic description, the light propagates within the volume of the 2D metamaterial. The theoretical design problem and optimisation of 2D metamaterial slab waveguides is consequently a challenge that merits further investigation given the potential to reap rich rewards.

3. The SEM images of the fabricated chip revealed fabrication errors, including dimension errors, waveguide wall roughness, distorted hole shape, damage and debris. It is important to understand the extent to which these impairments are intrinsic to the process or simply reflect poor process control. Better care in the fabrication process may reduce the loss, scattering and phase bias errors especially in MZI structures. The experience of microelectronics leads one to expect the properties of an individual device to vary from wafer to wafer but nominally identical devices, especially when adjacent, to behave almost exactly the same. For example, it is well known that LiNbO3 Mach-Zehnder modulators offer larger extinction on the cross-path than the through-path as a consequence of the symmetry provided by a near identical pair of directional couplers.

The LiNbO3 material platform supports low-index contrast waveguide components with relatively large foot-print. In contrast, the SOI material platform used in this research supports high-index contrast waveguide components with relatively small foot-print. It was found that the sidewalls of the silicon ridge waveguides on the fabricated chip were subject to undulations which were uncorrelated between adjacent waveguides. The lack of correlation suggests that the error is caused by fluctuations in the position, width or intensity of the e-beam in the direct write process rather than spatial variations of the etching process. It was found that minute differential waveguide width errors of the order of 30 pm can completely unbalance a Mach-Zehnder interferometer. This is the most serious impairment found in terms of the component sensitivity to the fabrication error (MZI). If this particular impairment cannot be cured by improved process control then every MZI on the chip must feature monitors to sense the operating point and a controller to adjust phase-shift elements to set the MZI to the desired state [29]. It would be preferable to avoid such complexity whenever possible. This merits the collation and analysis of data on fabricated test-structure to assess the extent to which uncorrelated impairments are an intrinsic or a matter of poor process control as well as research into the actuators, sensors and control algorithms required to circumvent the effect of the most serious impairments with the goal of 'perfect optical systems using imperfect optics' [36].

4. While the optical losses between lensed fibres and silicon photonic waveguides do not prevent the characterisation of photonic integrated circuits for academic purposes, high insertion loss is an obstacle to commercialisation. Many researchers use vertical couplers that offer loss of the order of ~6 dB which is somewhat better than the high loss of ~12 dB of butt-coupling. Vertical couplers are certainly valuable for wafer-test probing but are unsuited to packaging. A variety of edge coupling schemes for low-loss coupling between optical fibres and silicon photonic wires have been proposed most of which rely on a subwavelength waveguide structure of some kind [37, 38]. Especially for the purpose of commercialisation, a comparative study of the merits and demerits of the many schemes is needed to identify a means of attaining <1dB coupling loss without concerns regarding fabrication feature size limitations or robust mounting of the fibre.

5. Further work is required to formulate practical models of metamaterial components. The ideal would be to have a means of homogenisation that permits one to substitute a continuous medium approximation in place of the metamaterial and then be able to analyze the component by classical means. As nanofabrication progresses such a simple process will become increasingly accurate. However, in the just subwavelength regime a homogenisation method that accurately reproduces the dispersion relation is strictly only valid for an unbounded medium. Whereas one might expect the theory to be valid in the interior of a bounded medium, one can expect boundary layers within which the electromagnetic field transitions across a material interface from the interior solution on either side of the interface. These layers will be many unit cells thick and hence may be comparable to the dimensions of the component. The problem is that the boundary

condition that should be applied to the smoothed field needed to correctly predict Fresnel transmission and reflection coefficients is not known. The problem is further compounded by the emergence of anisotropic properties and especially spatial dispersion which complicate the analysis of the continuous medium approximation of the component. While commercially simulation tools may admit the specification of an anisotropic material, none admit the specification of spatial dispersion. This thesis found that for some specific geometries of practical utility the agreement between very simple models and accurate numerical calculations is remarkably good, at least for Ex-like waveguide modes. Further work is needed to bring the predictions for Ey-modes up to a similar accuracy. The most likely deficiency is the neglect of anisotropy of the material on the waveguide dispersion relation for the Ey-like mode needed to correct the reciprocal space path to account for waveguide confinement. In this thesis the problem was largely side-stepped through the use of adiabatic transition tapers. An exception was the abrupt junction between the access waveguides and the rim of the Lüneburg lenses. The coupling to the planar metamaterial Lüneburg lenses could be improved by using metamaterial tapers between the conventional access waveguide and the metamaterial region at the rim of the lens.

Despite the issues associated with unknown boundary conditions and the complexity brought by anisotropy and spatial dispersion, one may be optimistic that theoretical models of practical utility can be formulated. For example, the effective mass approximation in which the crystal potential is effectively homogenised to yield a smoothed envelop of the effective wave-function and an associated effective potential, has a similar issue in respect of the boundary conditions that should apply at an abrupt junction between two different crystals. Yet the approximation is routinely used to predict the energy levels of quantum wells which not only present heterojunctions but also have a thickness that may be counted in numbers of atomic layers. This suggests that photonic heterojunctions merit further research. It would also be worthwhile to explore metamaterial constituents that are not restricted to dielectrics.

Appendix I:
The Details of Analysis on Different Test Structures

The details of analysis on different test structures in Chapter 5, section 5.4, are provided below:

In the structure with the arm width of 1.732 µm, and the hole diameter in the constant region of the arm of 120 nm, the slope of the simulation data was obtained as $4.53 \times 10^{-4}\ \mathrm{nm}^{-1}\ \mu\mathrm{m}^{-1}$ which becomes $4.53 \times 10^{-4} \times 10^{3} = 0.453\ \mu\mathrm{m}^{-2}$ and hence, $\Delta n_g = (1.55)^2 \times 0.453 = 1.088$.

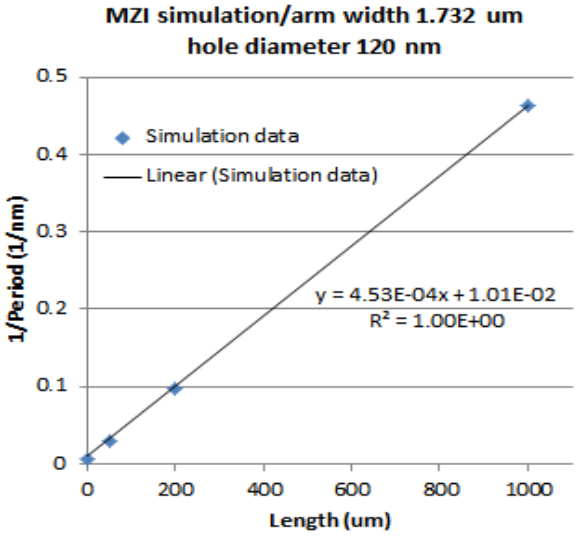

Figure I.1 The linear relation of the simulation data obtained from the plot of inverse period versus the length of the devices with the arm width of 1.732 µm and constant hole diameter of 120 nm with the different central region lengths of 0 µm, 50 µm, 200 µm and 1000 µm.

In experiment, the slope was obtained as $3.96 \times 10^{-4}\ \mathrm{nm}^{-1}\ \mu\mathrm{m}^{-1}$ or $3.96 \times 10^{-4} \times 10^{3} = 0.396\ \mu\mathrm{m}^{-2}$, hence $\Delta n_g = (1.55)^2 \times 0.396 = 0.951$.

The theory calculations showed the group index of wide arm with holes is 3.226, and the group index of waveguide with the width of 0.45 µm of silicon was obtained as 4.330 which gives $\Delta n_g = 3.225 - 4.330 = -1.104$. With regards to the three results obtained, the simulation and theory were closer but the error of the experimental result was also low.

In the next device of this set the hole diameter in the constant region of the arm was changed to 100 nm while the width of the arm remained the same. The slope was obtained in simulation $3.94 \times 10^{-4}\mathrm{nm}^{-1}\ \mu\mathrm{m}^{-1}$ which results $3.94 \times 10^{-4} \times 10^{3} = 0.394\ \mu\mathrm{m}^{-2}$ and consequently $\Delta n_g = (1.55)^2 \times 0.394 = 0.946$.

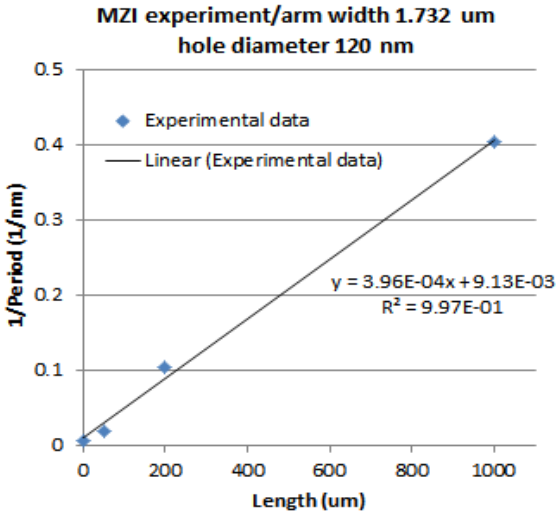

Figure I.2 The linear relation of the experimental data obtained from the plot of inverse period versus the length of the devices with the arm width of 1.732 µm and constant hole diameter of 120 nm with the different central region lengths of 0 µm, 50 µm, 200 µm and 1000 µm.

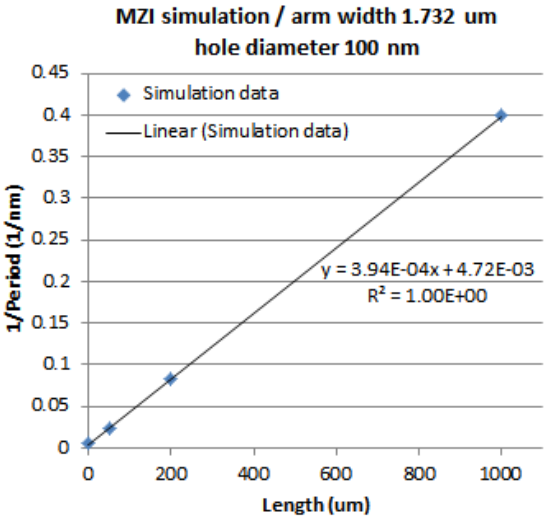

Figure I.3 The linear relation of the simulation data obtained from the plot of inverse period versus the length of the devices with the arm width of 1.732 µm and constant hole diameter of 100 nm with the different central region lengths of 0 µm, 50 µm, 200 µm and 1000 µm.

In the experiment, the device with 200 µm length was not readable due to a defect on the access waveguide, but the three remaining data points matched well with the linear fit. The slope was obtained as $2.97 \times 10^{-4} \mathrm{nm}^{-1}\,\mu\mathrm{m}^{-1}$ which becomes $2.97 \times 10^{-4} \times 10^{3} = 0.297\ \mu\mathrm{m}^{-2}$, hence $\Delta n_g = (1.55)^2 \times 0.297 = 0.713$

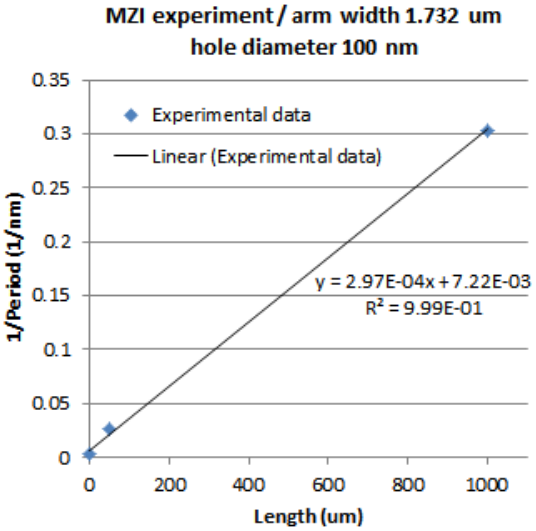

Figure I.4 The linear relation of the experimental data obtained from the plot of inverse period versus the length of the devices with the arm width of 1.732 µm and constant hole diameter of 100 nm with the different central region lengths of 0 µm, 50 µm, 200 µm and 1000 µm

In the theory calculation, the group index of wide arm with holes in this case was obtained as 3.376, and the group index of waveguide with the width of 0.45 µm of silicon was obtained as 4.330. So $\Delta n_g = 4.330 - 3.376 = 0.953$, which showed the theory and simulation matched closely but there was a significant error in the experimental result which was expected due to the possible curve fitting error and mainly fabrication error as the diameter of holes decreased to 100nm which was the limitation of the fabrication process.

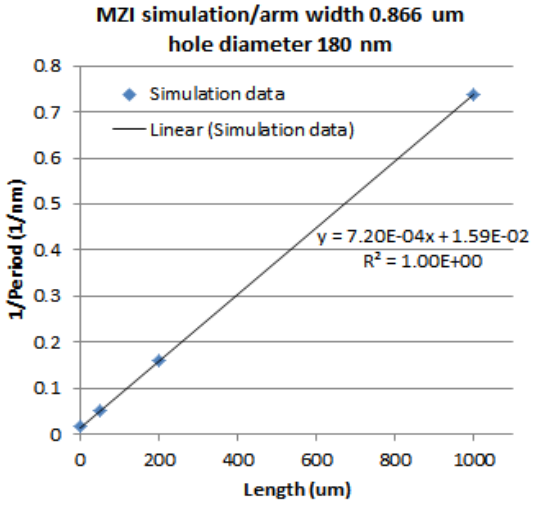

Figure I.5 The linear relation of the simulation data obtained from the plot of inverse period versus the length of the devices with the arm width of 0.866 µm and constant hole diameter of 180 nm with the different central region lengths of 0 µm, 50 µm, 200 µm and 1000 µm.

In the next step, the arm width was decreased to 0.866 µm but keeping the hole diameters the same set as previous structure. In this device, when the hole diameters in the constant region

was 180 nm, the slope of the simulation for different length of the constant region was obtained as $7.20 \times 10^{-4}\,\mathrm{nm}^{-1}\,\mu\mathrm{m}^{-1}$ which became $7.20 \times 10^{-4} \times 10^{3} = 0.720\,\mu\mathrm{m}^{-2}$, hence $\Delta n_g = (1.55)^2 \times 0.720 = 1.729$.

In experiment, the slope was obtained as $7.76 \times 10^{-4}\,\mathrm{nm}^{-1}\,\mu\mathrm{m}^{-1}$ consequently $7.76 \times 10^{-4} \times 10^{3} = 0.776\ \mu\mathrm{m}^{-2}$, hence $\Delta n_g = (1.55)^2 \times 0.776 = 1.864$

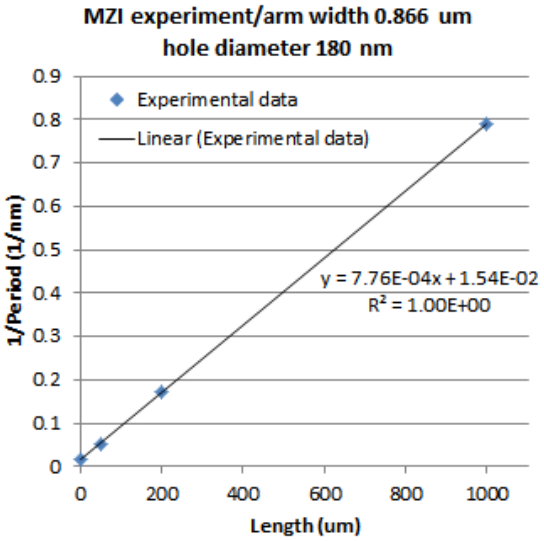

Figure I.6 The linear relation of the experimental data obtained from the plot of inverse period versus the length of the devices with the arm width of 0.866 µm and constant hole diameter of 180 nm with the different central region lengths of 0 µm, 50 µm, 200 µm and 1000 µm.

In the theory calculations, the group index of wide arm with holes in this case was obtained as 2.626, and the group index of waveguide with the width of 0.45um of silicon was obtained as 4.330. Hence, $\Delta n_g = 4.330 - 2.626 = 1.704$. This showed the error between the experimental results and simulation increased in this case which could be the result of the breakdown of assumptions due to the narrow width of the arm.

When the hole diameters in the constant region decreased to 120 nm, keeping the width of the arm 0.866 µm, the slope was obtained in simulation as $3.56 \times 10^{-4}\,\mathrm{nm}^{-1}\,\mu\mathrm{m}^{-1}$ which becomes$3.53 \times 10^{-4} \times 10^{3} = 0.356\,\mu\mathrm{m}^{-2}$, hence $\Delta n_g = (1.55)^2 \times 0.356 = 0.855$.

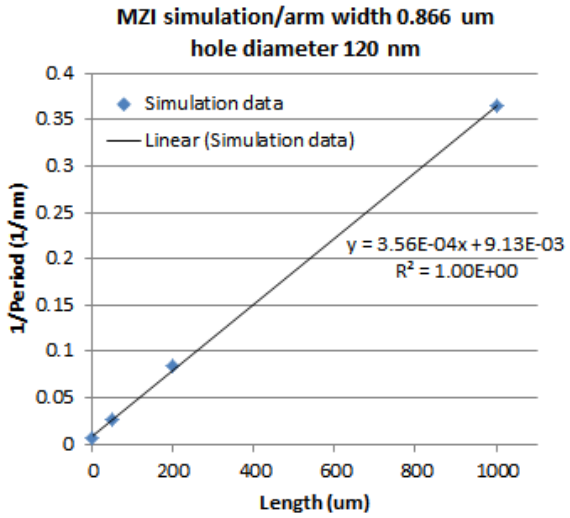

Figure I.7 The linear relation of the simulation data obtained from the plot of inverse period versus the length of the devices with the arm width of 0.866 µm and constant hole diameter of 120 nm with the different central region lengths of 0 µm, 50 µm, 200 µm and 1000 µm

The experimental slope was obtained as $3.40 \times 10^{-4}\ \mathrm{nm}^{-1}\ \mu\mathrm{m}^{-1}$ which becomes $3.40 \times 10^{-4} \times 10^{3} = 0.340\ \mu\mathrm{m}^{-2}$, hence $\Delta n_g = (1.55)^2 \times 0.340 = 0.816$.

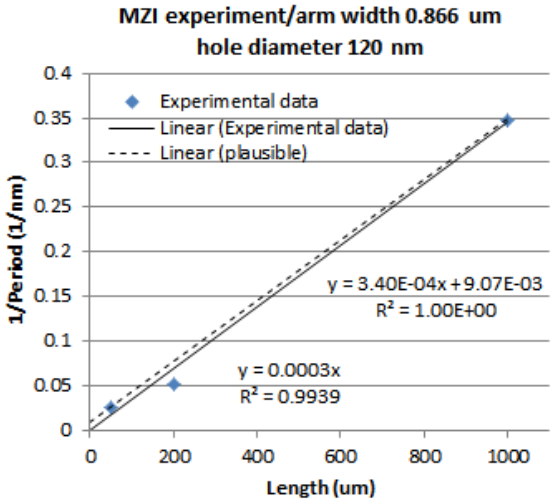

Figure I.8 The linear relation of the experimental data obtained from the plot of inverse period versus the length of the devices with the arm width of 0.866 µm and constant hole diameter of 120 nm with the different central region lengths of 0 µm, 50 µm, 200 µm and 1000 µm

The theory calculations result in the group index of wide arm with holes in this case as 3.368, and the group index of waveguide with the width of 0.45um of silicon is obtained as 4.330. So $\Delta n_g = 4.330 - 3.368 = 0.961$.

When the hole diameters decrease more to 100nm, the slope was obtained in simulation as $3.38 \times 10^{-4}\ \mathrm{nm}^{-1}\ \mu\mathrm{m}^{-1}$ which results $3.38 \times 10^{-4} \times 10^{3} = 0.338\ \mu\mathrm{m}^{-2}$, hence $\Delta n_g = (1.55)^2 \times 0.338 = 0.812$.

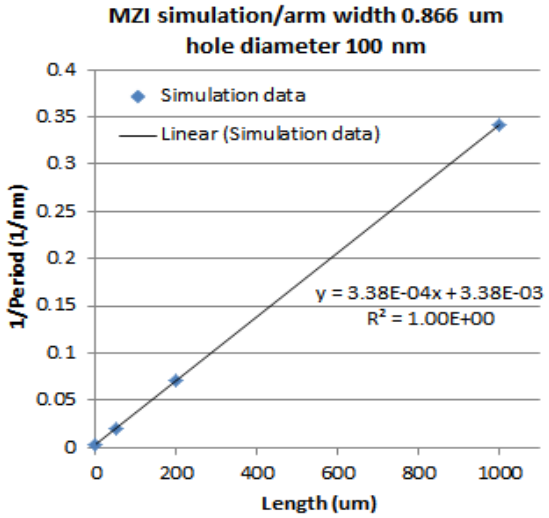

Figure I.9 The linear relation of the simulation data obtained from the plot of inverse period versus the length of the devices with the arm width of 0.866 μm and constant hole diameter of 100 nm with the different central region lengths of 0 μm, 50 μm, 200 μm and 1000 μm.

The data at the 0 length device was not readable in measurements. In experiment, the slope was obtained as $3.10 \times 10^{-4}\ \mathrm{nm}^{-1}\ \mu\mathrm{m}^{-1}$ which becomes $3.10 \times 10^{-4} * 10^{3} = 0.310\ \mu\mathrm{m}^{-2}$, hence $\Delta n_g = (1.55)^2 \times 0.310 = 0.744$

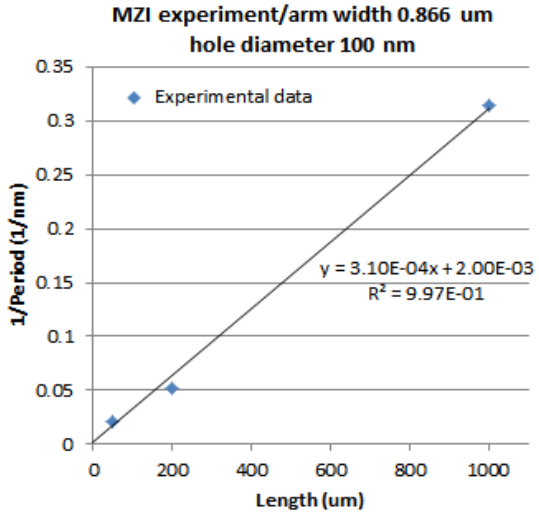

Figure I.10 The linear relation of the experimental data obtained from the plot of inverse period versus the length of the devices with the arm width of 0.866 μm and constant hole diameter of 100 nm with the different central region lengths of 0 μm, 50 μm, 200 μm and 1000 μm.

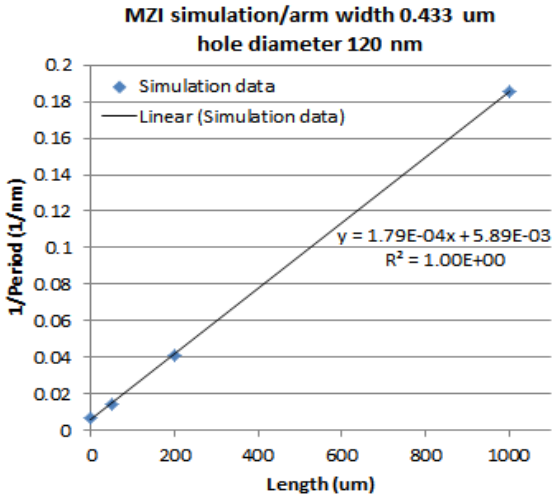

Figure I.11 The linear relation of the simulation data obtained from the plot of inverse period versus the length of the devices with the arm width of 0.433 μm and constant hole diameter of 120 nm with the different central region lengths of 0 μm, 50 μm, 200 μm and 1000 μm.

In the theory calculations, the group index of wide arm with holes in this case is obtained as 3.513, and the group index of waveguide with the width of 0.45 μm of silicon is obtained as 4.330. Hence, $\Delta n_g = 4.330 - 3.513 = 0.816$.

When the arm width was decreased to 0.433 μm the setting of the hole diameters changed to 120 nm, 100 nm and 80 nm. In the device with the hole diameters in the constant region of 120 nm, the slope of the simulation for different length of the constant region was obtained as $1.79 \times 10^{-4}\ \text{nm}^{-1}\ \mu\text{m}^{-1}$ which results $1.79 \times 10^{-4} \times 10^3 = 0.179\ \mu\text{m}^{-2}$, hence $\Delta n_g = (1.55)^2 \times 0.179 = 0.430$.

In experiment, the slope was obtained as $3.50 \times 10^{-4}\ \text{nm}^{-1}\ \mu\text{m}^{-1}$ which becomes $3.50 \times 10^{-4} \times 10^3 = 0.350\ \mu\text{m}^{-2}$, hence $\Delta n_g = (1.55)^2 \times 0.350 = 0.840$

In the theory calculations, the group index of wide arm with holes in this case is obtained as 3.978, and the group index of waveguide with the width of 0.433 μm of silicon is obtained as 4.397. So $\Delta n_g = 4.397 - 3.978 = 0.419$.

In the device with the hole diameters in the constant region of 100 nm, the slope of the simulation for different length of the constant region was obtained as $1.06 \times 10^{-4}\ \text{nm}^{-1}\ \mu\text{m}^{-1}$ which becomes $1.06 \times 10^{-4} \times 10^3 = 0.106\ \mu\text{m}^{-2}$, hence $\Delta n_g = (1.55)^2 \times 0.106 = 0.254$.

In the experiment, the slope was obtained as $1.72 \times 10^{-4}\ \text{nm}^{-1}\ \mu\text{m}^{-1}$ which becomes $1.72 \times 10^{-4} \times 10^3 = 0.172\ \mu\text{m}^{-2}$, hence $\Delta n_g = (1.55)^2 \times 0.172 = 0.413$.

In the theory calculations, the group index of wide arm with holes in this case is obtained as 4.146131, and the group index of waveguide with the width of 0.433 μm of silicon is obtained as 4.397. So $\Delta n_g = 4.397 - 4.146 = 0.251$.

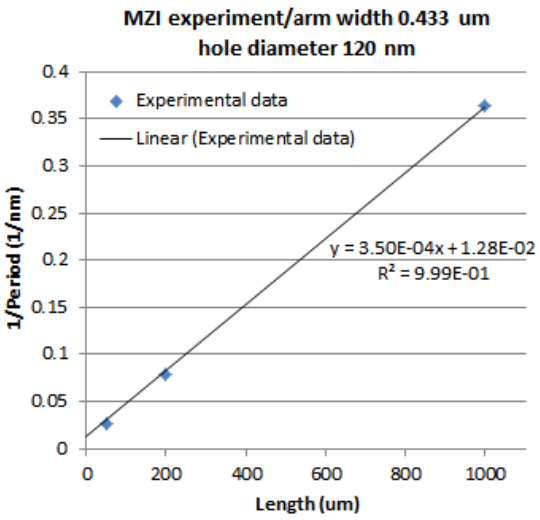

Figure I.12 The linear relation of the experimental data obtained from the plot of inverse period versus the length of the devices with the arm width of 0.433 µm and constant hole diameter of 120 nm with the different central region lengths of 0 µm, 50 µm, 200 µm and 1000 µm.

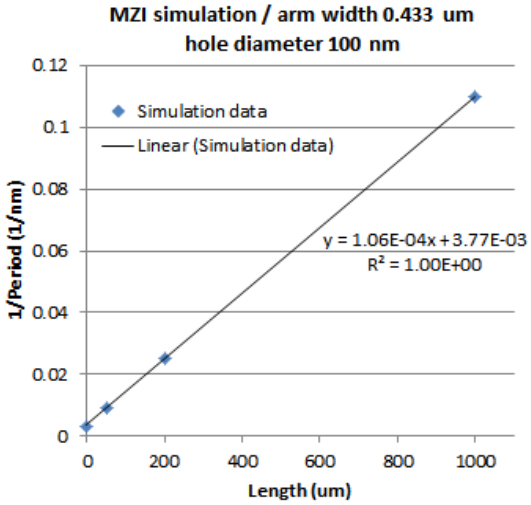

Figure I.13 The linear relation of the simulation data obtained from the plot of inverse period versus the length of the devices with the arm width of 0.433 µm and constant hole diameter of 100 nm with the different central region lengths of 0 µm, 50 µm, 200 µm and 1000 µm.

In the device with the hole diameters in the constant region of 80 nm, the slope of the simulation for different length of the constant region was obtained as $6.33 \times 10^{-5}\,\mathrm{nm}^{-1}\,\mu\mathrm{m}^{-1}$ which results $6.33 \times 10^{-5} \times 10^{3} = 0.063\ \mu\mathrm{m}^{-2}$, hence $\Delta n_g = (1.55)^2 \times 0.063 = 0.151$.

In the experiment, the slope was obtained as $8.77 \times 10^{-5}\,\mathrm{nm}^{-1}\,\mu\mathrm{m}^{-1}$ which becomes $8.77 \times 10^{-5} \times 10^{3} = 0.087\ \mu\mathrm{m}^{-2}$, hence $\Delta n_g = (1.55)^2 \times 0.087 = 0.209$.

In the theory calculations, the group index of wide arm with holes in this case is obtained as 4.245, and the group index of waveguide with the width of 0.433 μm of silicon is obtained as 4.397. So $\Delta n_g = 4.397 - 4.245 = 0.152$.

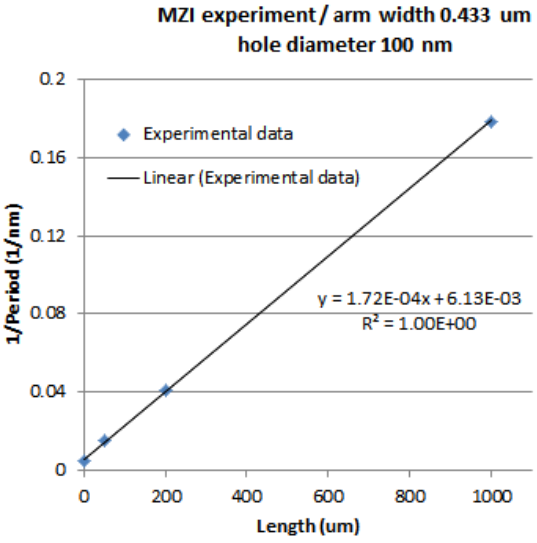

Figure I.14 The linear relation of the experimental data obtained from the plot of inverse period versus the length of the devices with the arm width of 0.433 μm and constant hole diameter of 100 nm with the different central region lengths of 0 μm, 50 μm, 200 μm and 1000 μm.

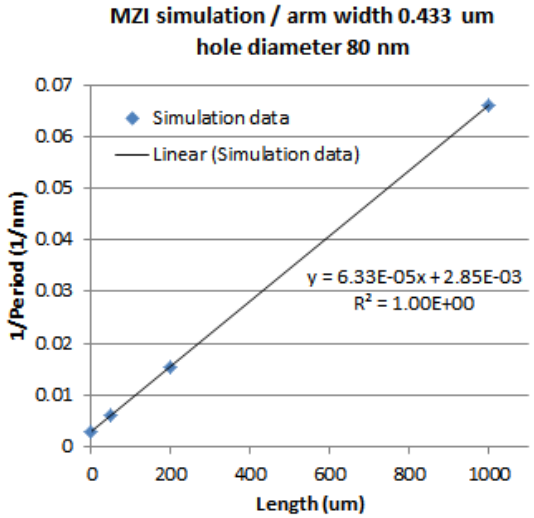

Figure I.15 The linear relation of the simulation data obtained from the plot of inverse period versus the length of the devices with the arm width of 0.433 μm and constant hole diameter of 80 nm with the different central region lengths of 0 μm, 50 μm, 200 μm and 1000 μm.

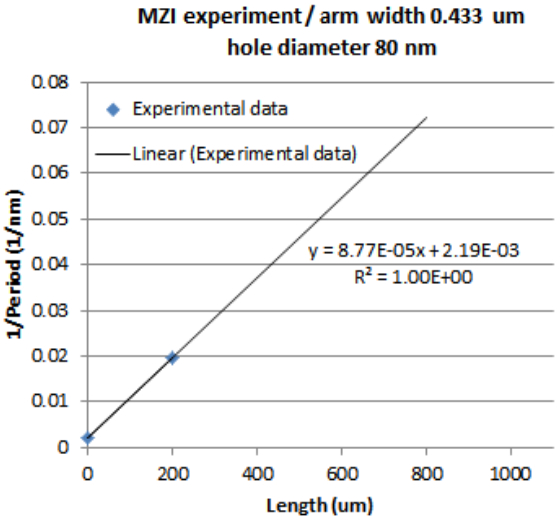

Figure I.16 The linear relation of the experimental data obtained from the plot of inverse period versus the length of the devices with the arm width of 0.433 µm and constant hole diameter of 80 nm with the different central region lengths of 0 µm, 50 µm, 200 µm and 1000 µm.

Appendix II:
FSR Relation

In Chapter 5, section 5.4, the FSR relation was obtained as follows:

$$\emptyset_1 - \emptyset_2 = \emptyset_c + \frac{2\pi}{\lambda_0} n_{effarm} L - \frac{2\pi}{\lambda_0} n_{gSi} L \quad \text{(II.1)}$$

$$\emptyset = \frac{\omega}{C}(n_{effarm} - n_{gSi})L \quad \text{(II.2)}$$

$$\emptyset = \frac{2\pi f}{C}(\Delta n_g)L \quad \text{(II.3)}$$

$$\Delta\emptyset = 2\pi \quad \text{(II.4)}$$

$$\Delta\emptyset = 2\pi = \frac{2\pi}{C}(\Delta n_g)L\Delta f \quad \text{(II.5)}$$

$$\Delta f = \frac{C}{\Delta n_g L} \quad \text{(II.6)}$$

Or as $\frac{2\pi f}{C} = \frac{2\pi}{\lambda}$ hence $f = \frac{C}{\lambda}$ and $\Delta f = \frac{C\Delta\lambda}{\lambda^2}$ hence:

$$\Delta f = \frac{C\Delta\lambda}{\lambda^2} = \frac{C}{\Delta n_g L} \quad \text{(II.7)}$$

Then

$$\Delta\lambda = \frac{\lambda^2}{\Delta n_g L} \quad \text{(II.8)}$$

Appendix III:
Python Script to Create Metamaterial Arm with Taper for MZI

A script written in Python automated the creation of the metamaterial arm of the MZI test structures. Here as an example, an arm will be created automatically on Crystalwave through its script interface with the width of 0.866 μm, the constant hole diameter in the centre region of 180 nm, with the length of the region as 50 μm, with two metamaterial taper at the both sides with the length of 35 μm, when the hole diameters are changing from 12.6 nm to 180 nm. As the position of the holes along the taper determine the desired refractive indices, a raster scan across the lattice using the Bravais vectors over an area that contains the device is performed. The script checks whether or not the lattice site visited falls within the device or not. If it falls within the device, the default atom is updated with an atom from an indexed palette. The local effective index corresponding to a unit cell composed of the indexed atom may found by the calibration process described in the preceding. The desired local effective index at the atom co-ordinate normally determines the hole diameter and hence the index by a look up process. In the case of the test structure tapers, it was found simpler and more direct to vary the hole diameters linearly between the two ends of the taper. This results in an effective index that varies approximately linearly with fill-factor and hence quadratically with respect to diameter which is close to the optimum profile of a taper and was found to work well.

```
#### Python code to create metamaterial arm with the width of 0.866 um
#### The hole diameters in the centre region of 180 nm for 50 um length of the centre region
####Metamaterial taper of 35 um at the both side of the constant centre region
from pdPythonLib import*
from numpy import*

f = pdApp() # make the connection with Crystalwave
f.ConnectToApp()

######## initial values
lc = 250.0          # lattice constant (nm)
lc = lc/1000.0      # lattice constant (um)

######################################## Parameters

dc = 180 #200.0              # atom diameter in centre region (nm)
L = 80.0 #82.0              # length of the whole structure, dark blue except taper width change
L22 = 10 #12                # length of centre constant atom region
TB = 0.866028 #1.73205080#0.866025# 0.433012701 # Width of the device 0.866028

########################################

dc = dc/1000.0      # atom diameter in centre region (um)

na = 256            # number of atoms added to palette


L1 = L/2            # length of the half the structure, dark blue except taper width change
z4 = L1/0.25        # right side of right-transition taper region converted to atom number(um)
z4 = z4+0.75
z1 = -L1/0.25       # left side of left-transition taper region converted to atom numbers(um)
z1 = z1-0.75


L2 = L22/2          # length of half constant region from zero (centre)
```

```
36
37    z2 = -L2/0.25       # right side of left-transition taper
      region converted to atom number (um)
38    z3 = L2/0.25        # left side of right-transition taper
      region converted to atom number(um)
39
40
41    LT = 20.0            # length of the width change taper
42    W = 0.45            # width of the single mode access waveguide
43
44    ######## create the atom with specified name & diameter
45    for k in range (1,na):
46        d = k*dc/na
47
48        f.Exec(
      "app.subnodes[1].subnodes[1].pcdevice.addellippaletteatom(3)")
49        f.Exec(
      "app.subnodes[1].subnodes[1].pcdevice.paletteatoms2d[{k+1}].star
      tchange()")
50        f.Exec(
      "app.subnodes[1].subnodes[1].pcdevice.paletteatoms2d[{k+1}].name
      ={k}")
51        f.Exec(
      "app.subnodes[1].subnodes[1].pcdevice.paletteatoms2d[{k+1}].shap
      e.width={d}")
52        f.Exec(
      "app.subnodes[1].subnodes[1].pcdevice.paletteatoms2d[{k+1}].shap
      e.height={d}")
53        f.Exec(
      "app.subnodes[1].subnodes[1].pcdevice.paletteatoms2d[{k+1}].fini
      shchange()")
54
55    ######### visit each lattice site & update atom in transition
      region
56    bz=array([1.0,0.0])       # Bravais vector bz with z component
57    bx=array([0.5,0.866])     # Bravais vector bx with both z and x
      components
58    bz_p=array([0.0,1.0])     # perpendicular vector, complementary
59    bx_p=array([-0.866,0.5]) # perpendicular vector
60
61
62
63
64    # scan limits
65
66    TB1 = TB/2
```

```
67   bot = -TB1/0.216
68   bot = int(bot)
69
70   top = TB1/0.216
71   top = int(top)
72
73   left = -600 #-204
74   right = 600 #204
75
76   for j in range (bot,top+1,1):          # scanning the area,
     checking the position of the atom
77       for i in range (left,right,1):
78
79           pos = i*bz+j*bx
80           z=pos[0]
81
82
83           if (z>=z1) and (z<z2):# atom inside the left
     transition region?
84               t = (z-z1)/(z2-z1)
85               t = sqrt(t)
86               k = int(t*(na-1))  # find the atom number to
     substiute with the previous atom
87               f.Exec(
     "app.subnodes[1].subnodes[1].pcdevice.objects[1].lattice2d.clear
     latticepoint({i},{j})")      # deleting the old atom
88               f.Exec(
     "app.subnodes[1].subnodes[1].pcdevice.objects[1].lattice2d.addla
     tticeatom({k+1},{i},{j})")   # susbtituting the new atom
89
90           if (z>=z2) and (z<=z3): # atom inside uniform region?
91               k = na-1  # find the atom number to substitute
     with the previous atom
92               f.Exec(
     "app.subnodes[1].subnodes[1].pcdevice.objects[1].lattice2d.clear
     latticepoint({i},{j})")      # deleting the old atom
93               f.Exec(
     "app.subnodes[1].subnodes[1].pcdevice.objects[1].lattice2d.addla
     tticeatom({k+1},{i},{j})")   # susbtituting the new atom
94
95           if (z>z3) and (z<=z4): # atom inside the right
     transition region?
96               t = (z4-z)/(z4-z3)
97               t = sqrt(t)  # linear fill-factor in taper
98               k = int(t*(na-1))  # find the atom number to
     substiute with the previous atom
```

```
 99              f.Exec(
    "app.subnodes[1].subnodes[1].pcdevice.objects[1].lattice2d.clear
    latticepoint({i},{j})")     # deleting the old atom
100             f.Exec(
    "app.subnodes[1].subnodes[1].pcdevice.objects[1].lattice2d.addla
    tticeatom({k+1},{i},{j})")  # susbtituting the new atom
101
102 f.Exec(
    "app.subnodes[1].subnodes[1].pcdevice.objects[1].startchange()"
    )
103 f.Exec(
    "app.subnodes[1].subnodes[1].pcdevice.objects[1].sizex={TB+0.000
    003}") # Resize the blue region x
104 f.Exec(
    "app.subnodes[1].subnodes[1].pcdevice.objects[1].sizez={L}")
    # Resize the blue region z
105 f.Exec(
    "app.subnodes[1].subnodes[1].pcdevice.objects[1].finishchange()"
    )
106
107 #f.Exec("app.subnodes[1].subnodes[1].pcdevice.addrectangle(1,-{L
    1+1+LT},0.0,0.000000,2.2,{W})") # left access waveguide
108 #f.Exec("app.subnodes[1].subnodes[1].pcdevice.addrectangle(1,{L1
    +1+LT},0.0,0.000000,2.2,{W})")# right access waveguide
109
110 f.Exec("app.subnodes[1].subnodes[1].pcdevice.startchange()")
111 f.Exec(
    "app.subnodes[1].subnodes[1].pcdevice.setdimensions(-{L1+1.8+LT}
    ,{L1+1.8+LT},-{2*TB+8.0},{2*TB+8.0})")  # resize the device
    (light blue)
112 f.Exec("app.subnodes[1].subnodes[1].pcdevice.finishchange()")
113
114 #f.Exec("app.subnodes[1].subnodes[1].pcdevice.addmodesensorzx(-{
    L1+1+LT},0.0,0.000000,{3*TB})")  # Sensor 1
115 #f.Exec("app.subnodes[1].subnodes[1].pcdevice.addmodesensorzx({L
    1+1+LT},0.0,0.000000,{3*TB})")  # Sensor 2
116
117
118 f.Exec(
    "app.subnodes[1].subnodes[1].pcdevice.addlinearpath(1,-{L1+LT},0
    .0,0.000000,{LT},0.0,{W},{TB+0.000003},0.000000,0.000000)")
    #taper left
119 # (1,Zleft,Xleft, angle of the waveguide, L, Xright, dleft,
    dright, normal angle on left, normal angle on the right)
120 W=0.45
121 f.Exec(
```

```
    "app.subnodes[1].subnodes[1].pcdevice.addlinearpath(1,{L1},0.0,0
    .000000,{LT},0.0,{TB+0.000003},0.45,0.000000,0.000000)")
    #taper right
122
123 #####Trench
124 ##f.Exec("app.subnodes[1].subnodes[1].pcdevice.addrectangle(2,-1
    4.348512,-6.224931,0.000000,5.765813,2.442992)")
125 ##f.Exec("app.subnodes[1].subnodes[1].pcdevice.objects[2].startc
    hange()")
126 ##f.Exec("app.subnodes[1].subnodes[1].pcdevice.objects[2].sizex=
    {TB+0.000003+8.0}") # Resize the pink region x
127 ##f.Exec("app.subnodes[1].subnodes[1].pcdevice.objects[2].sizez=
    {L}")   # Resize the pink region z
128 ##f.Exec("app.subnodes[1].subnodes[1].pcdevice.objects[2].finish
    change()")
129 ##
130 ##f.Exec("app.subnodes[1].subnodes[1].pcdevice.addlinearpath(2,-
    {L1+LT},0.0,0.000000,{LT},0.0,{TB+0.000003+8.0},{TB+0.000003+8.0
    },0.000000,0.000000)") #taper left
131 ### (1,Zleft,Xleft, angle of the waveguide, L, Xright, dleft,
    dright, normal angle on left, normal angle on the right)
132 ##W=0.45
133 ##f.Exec("app.subnodes[1].subnodes[1].pcdevice.addlinearpath(2,{
    L1},0.0,0.000000,{LT},0.0,{TB+0.000003+8.0},{TB+0.000003+8.0},0.
    000000,0.000000)")  #taper right
134 ##
135
136 ##
137 raw_input(">>>>")  #OMNISIM waits for the user to press return
    on the keyboard before continuing.
138 del f    #delete the connection and close the script
139
```

Bibliography:

[1] Rytov, S. M., *"Electromagnetic properties of a finely stratified medium",* Soviet Physics JETP-USSR, **2**(3), (1956):466-475.

[2] Schmid, J. H., Cheben, P., *et al*., *"Refractive index engineering with subwavelength gratings in silicon microphotonic waveguides",* IEEE Photonics Journal, **3**(3), (2011):597-607.

[3] Nikkhah, H., Hall, T., *"Metamaterial Lüneburg lens for Fourier optics on-a-chip*", Proc. SPIE 8988, Integrated Optics: Devices, Materials, and Technologies XVIII, (2014):89880J-89880J

[4] Bock, P. J., *"Addressing the challenges of silicon waveguides with subwavelength nanostructures",* PhD Thesis, Université d'Ottawa/University of Ottawa, 2011.

[5] Chen, H., Poon, A. W., *"Low-loss multimode-interference-based crossings for silicon wire waveguides",* IEEE Photonics Technology Letters, **18**(21), (2006):2260-2262.

[6] Fukazawa, T., *et al*., *"Low loss intersection of Si photonic wire waveguides",* Japanese Journal of Applied Physics, **43**(2R), (2004):646.

[7] Bogaerts, W., *et al*., *"Low-loss, low-cross-talk crossings for silicon-on-insulator nanophotonic waveguides",* Optics Letters, **32**(19), (2007):2801-2803.

[8] Gallagher, D. F.G., Felici, T. P., *"Eigenmode Expansion Methods for Simulation of Optical Propagation in Photonics - Pros and Cons",* Photonics West, San Jose, 2003, Proc. SPIE, **4987**-10, (2003):69-82.

[9] Molina-Fernández, I., *et al*., *"Improving multimode interference couplers performance through index profile engineering",* Journal of Lightwave Technology, **27**(10), (2009):1307-1314.

[10] Halir, R., *et al*., *"High-performance 90 hybrid based on a silicon-on-insulator multimode interference coupler",* Optics Letters, **36**(2), (2011):178-180.

[11] Ortega-Monux, A., et al., *"High-performance multimode interference coupler in silicon waveguides with subwavelength structures",* IEEE Photonics Technology Letters, **23**(19), (2011):1406-1408.

[12] Pérez-Galacho, D., *et al*., *"Integrated polarization beam splitter with relaxed fabrication tolerances",* Optics Express, **21**(12), (2013):14146-14151.

[13] Halir, R., *et al*., *"Ultra broadband waveveguide coupler using an anisotropic sub-wavelength metamaterial",* arXiv preprint arXiv:1606.03750, (2016).

[14] Maese-Novo, A., *et al*. *"Wavelength independent multimode interference coupler",* Optics Express, **21**(6), (2013):7033-7040.

[15] Xiong, Y., *et al*., *"Polarization splitter and rotator with subwavelength grating for enhanced fabrication tolerance",* Optics Letters, **39**(24), (2014):6931-6934.

[16] Dai, D., et al., *"Compact polarization beam splitter using an asymmetrical Mach–Zehnder interferometer based on silicon-on-insulator waveguides",* IEEE Photonics Technology Letters, **24**(8), (2012):673-675.

[17] Oughstun, K. E., *"Electromagnetic and Optical Pulse Propagation 1: Spectral Representations in Temporally Dispersive Media",* Springer Series in Optical Sciences, Ch. 4, (2006).

[18] Lorentz, H. A., *"The Theory of Electrons"*, Leipzig: Teubner, Ch. IV, (1906).

[19] Landau, L. D., Liftshitz, E. M., *"Electrodynamics of Continuous Media",* Pergamon Press LTD, Ch. II, second edition, (1963).

[20] Tsukerman, I., *"Computational Methods for Nanoscale Applications: Particles, Plasmons and Waves"*, Springer, (2008).
[21] Nikkhah, H., Hall, T., *"Subwavelength Grating Waveguide Design Rules for Integrated Photonics",* IEEE Proceedings of 9th International Congress on Advanced Electromagnetic Materials in Microwave and Optics (Metamaterials 2015), Oxford, UK, 7-12 September 2015, (2015):460-462.
[22] Nikkhah, H., *"Optical Switch on a Chip: The Talbot Effect, Lüneburg Lenses & Metamaterials",* MSc. Thesis, Université d'Ottawa/University of Ottawa, Canada, August (2013).
[23] Choy, T. C., *"Effective Medium Theory: Principles and Applications",* Oxford University Press, (1999).
[24] Kronig, R. D. L., Penney, W. G., *"Quantum mechanics of electrons in crystal lattice",* Proc. R. Soc. London, Ser. A, **130**, (1930):499-513
[25] Nikkhah, H., Hall, T., *"Subwavelength grating waveguides for Integrated Photonics",* Applied Physics A, **122**:368, (2016):1-6.
[26] Walther, A, *"Ray & Wave Theory of Lenses,"* Cambridge University Press, (2006).
[27] Bieren, K. von, *"Lens Design for Optical Fourier Transform Systems",* Applied Optics **10**(12), (1971):2739-2742.
[28] Luneburg, R. K., *"Mathematical Theory of Optics,"* Providence Rhode Island: Brown University, (1944): 189–21.
[29] Wilkes, C. M., Qiang, X., *et. al*., *"60 dB high-extinction auto-configured Mach–Zehnder interferometer",* Optics Letters, **41**(22), (2016):5318-5321.
[30] Zine-El-Abidine, I., *et al*. *"NanoSOI Design Manual",* Document ICI-233, V1.1, , CMC Microsystems, November 2012.
[31] Zheng, Q., *"Performance Characterization of Silicon-On-Insulator (SOI) Corner Turning and Multimode Interference Devices",* MSc. Thesis, Université d'Ottawa/University of Ottawa, Canada, 2012.
[32] LumArray, Inc. http://www.lumarray.com/ (*last visited* 1 Nov. 2017).
[33] Xu, D.-X., *et al*., *"Silicon Photonic Integration Platform— Have We Found the Sweet Spot?",* IEEE Journal of Selected Topics in Quantum Electronics, **20**(4), art. 8100217 (2014), (17 pages).
[34] Lu, J., Vŭckovíc, J., *"Nanophotonic computational design",* Optics Express, **21**(11), (2013):13351-13367.
[35] Shen, B., *et al*., *"An integrated-nanophotonics polarization beamsplitter with 2.4 × 2.4 μm2 footprint",* Nature Photonics, **9**, (2015): 378-382.
[36] Miller, D. A. B., *"Perfect optics with imperfect components",* Optica, **2**, (2015):747–750.
[37] Cheben, P., *et al*., *"Broadband polarization independent nanophotonic coupler for silicon waveguides with ultra-high efficiency",* Optics Express, **23**(17), (2015):22553-22563.
[38] Picard, M.-J., *et al*., *"Novel Spot-Size Converter for Optical Fiber to sub- μm Silicon Waveguide Coupling with Low Loss, Low Wavelength Dependence and High Tolerance to Alignment",* Optical Communication (ECOC), European Conference, IEEE, ISBN**:** 978-8-4608-1741-3 (2015).
[39] Nikkhah, H., Hasan, M., Hall, T.J., *"The Talbot effect in a metamaterial",* Applied Physics A, **124**:106, January (2018), (9 pages). https://doi.org/10.1007/s00339-017-1521-1